

PATHWAYS TO SPATIAL INSTABILITY IN MODELS OF FIRE PROPAGATION

Olivia Sarita Chandrasekhar

A dissertation submitted to the faculty at the University of North Carolina at Chapel Hill in partial fulfillment of the requirements for the degree of Doctor of Philosophy in the Department of Mathematics in the College of Arts and Sciences.

Chapel Hill & Los Alamos
2025

Approved by:
Christopher K.R.T. Jones
Rodman Linn
Blake Barker
Katherine Newhall
Jeremy Marzuola

© 2025
Olivia Sarita Chandrasekhar
ALL RIGHTS RESERVED

ABSTRACT

Olivia Sarita Chandrasekhar: Pathways to spatial instability in models of fire propagation

(Under the direction of Christopher K.R.T. Jones)

An equilibrium solution to a time-dependent system is considered stable if small disturbances decay in time and the solution eventually returns to its original form, perhaps up to a translation. Instability, on the other hand, is characterized by disturbances that grow exponentially and cause the solution to transition to a new, qualitatively different form. Often, the onset of instability leads to the formation of spatially patterned states. This type of spatial patterning is characteristic of a number of emergent phenomena in the field of wildland fire science. In order to understand the onset of instability in models of fire propagation and characterize the resulting spatially structured solutions, we study pathways to instability in two systems: a reaction-diffusion model of temperature and fuel concentration with a spatially dependent wind and a model of fluid flow over a heat source with a constant wind.

Using tools from geometric dynamical systems, we extend existing theory concerning the existence and stability of traveling wave solutions to reaction-diffusion systems to include systems with spatial dependence in the advection coefficient. An interesting result is that, in a system with spatial dependence constructed to model the fire-induced wind, traveling wave solutions exist for a continuum of wave speeds instead of a single, unique speed. We identify this range of speeds and explain how both the speed and shape of the traveling waves is influenced by the magnitude and sign of the imposed wind. We develop a selection mechanism to identify the one-dimensional fronts that are most likely to persist in nature and identify regions of transverse instability. Taken together, these results allow us to classify parameter regimes for which unstable two-dimensional fronts exist and visualize the resulting patterned states. Lastly, we examine an analogue of the classic model for Rayleigh-Bénard convection, adapted to the fire application by the addition of a crosswind term, and identify the conditions necessary for spatial patterning in a system that lacks the mechanisms of combustion and fuel consumption.

The pattern-forming mechanism in the first system is the interplay between the diffusing heat and the

combustion reaction; in the second system, it is thermally-driven buoyancy and the resulting fluid dynamics. We find regions of two-dimensional instability in both systems, suggesting that neither mechanism alone is responsible for the generation of spatial structure. However, our findings demonstrate that the existence of a spatially dependent, first-order forcing term capturing the dynamics of the local wind velocity leads to the emergence of patterned front solutions. The fact that the spatial patterning that develops in the fluids model resembles this forcing term strongly suggests that the spatially dependent wind is a key component contributing to the onset of pattern formation.

This dissertation is dedicated to the memory of my grandmother, Dr. Saroj
Chandrasekhar, and to all the other strong women in my life.

ACKNOWLEDGEMENTS

I would like to thank my advisor, Chris Jones, for continually challenging me while being unfailingly patient and supportive. I am incredibly lucky to have stumbled in to being a student of a mathematician and teacher as singular as Chris. I also owe thanks to Rod Linn, my mentor at Los Alamos, for introducing me to the world of fire modeling and for his infectious enthusiasm for science in all its forms; to Blake Barker, for teaching me about numerics and collaboration and being the kindest mathematician I have ever met; to Katherine Newhall and Jeremy Marzuola, for supporting me in this venture; to Michael Penn, for freshman year linear algebra; and to Mark Vondracek and Kamasi Hill, for showing me and so many other high school students what we were capable of.

I am grateful to my family, Melodie, Venkat and Max, for their unshakable belief in me from the very beginning and their continued support ever since. I am particularly thankful to my father, for teaching me to hate math (they say that love and hate are two sides of the same coin).

I would like to thank my friends, for whom my specific bits of gratitude would fill many pages, particularly: Charlie Tappan, JC Fillion-Robin, Holly Roper, Allison Dawn, Nina Friedman, Michelle Gee, the Barber Shop, and the members of the 2019 UNC math graduate cohort, who will always feel like family to me—especially Anna Coletti, without whom I would have been completely lost.

I am grateful for Patrick O'Hare, who is both the most solid foundation and the best source of distraction I could ever ask for.

Lastly, I would like to extend my sincere thanks to Ms. Black, for giving me a 40% on a seventh grade math test and kickstarting this whole stubborn venture.

TABLE OF CONTENTS

LIST OF FIGURES	x
CHAPTER 1: INTRODUCTION	1
1.1 A brief overview of wildland fire modeling	1
1.2 The mechanisms of pattern formation	2
1.3 Phenomena of interest	3
1.4 Questions addressed in this thesis	4
CHAPTER 2: BACKGROUND AND METHODS	8
2.1 A dynamical systems view of traveling waves	8
2.2 Computational methods for finding traveling waves	12
2.2.1 In phase space	12
2.2.2 As a boundary value problem	14
2.3 Stability	15
2.4 Finding the essential spectrum	17
2.5 Finding the point spectrum: Sturm-Liouville theory	18
2.5.1 A brief recap of Sturm-Liouville theory	18
2.5.2 Oscillation theory	19
2.5.3 An example	20
2.6 Finding the point spectrum: the Evans function	21
2.6.1 Constructing the Evans function	22
2.7 Mechanisms of instability	23
CHAPTER 3: A MODEL OF FIRE FRONT PROPAGATION	24
3.1 The model	26
3.2 Derivation of the model from conservation laws	27

3.3	The nondimensional model and separation of time scales	30
3.4	Assumptions on the wind term	31
3.5	Traveling wave solutions to the full system	31
3.6	The singular problem	33
3.7	Formulating the eigenvalue problem for the reduced system	35
3.8	Stability of one-dimensional front solutions in the constant wind case	38
3.8.1	The essential spectrum	38
3.8.2	The point spectrum	39
3.9	A note on parameter values	40
3.10	The rest of the problem	40
CHAPTER 4: STREAMWISE WIND VARIATION IN THE REDUCED SYSTEM		42
4.1	Introduction and motivation	42
4.2	The reduced system in one dimension	44
4.3	Constant wind	44
4.3.1	Solutions in phase space	45
4.3.2	Solutions to the boundary value problem	45
4.3.3	Stability	46
4.4	Constructing the spatially dependent wind	47
4.5	Solutions in phase space with a spatially dependent wind	48
4.5.1	Finding the invariant manifolds and their intersections	49
4.5.2	Stability properties of different intersection types	54
4.6	Profile solutions to the boundary value problem with a spatially dependent wind	56
4.7	Stability as a selection mechanism for the preferred wave	58
4.8	Conclusion	61
CHAPTER 5: TRANSVERSE WIND VARIATION IN THE REDUCED SYSTEM		64
5.1	Introduction	64
5.2	Motivating and constructing the spatially dependent wind	65
5.3	The transverse eigenvalue problem	66
5.4	The accumulated angle	69

5.5	Finding positive transverse eigenvalues and corresponding eigenfunctions	71
5.6	Comparing streamwise and transverse eigenvalues	74
5.7	Two-dimensional eigenfunctions	74
5.8	Discussion and conclusions	76
CHAPTER 6: EMERGENT INSTABILITIES IN WIND-DRIVEN BUOYANT FLOW		79
6.1	Motivation	79
6.2	Set up and formulation	81
6.3	The equations of state	83
6.3.1	Reduction to a system in w and θ	85
6.4	Normal mode analysis	85
6.5	Spatial eigenfunctions	87
6.6	Analyzing the spectrum	89
6.7	Conclusion	92
CHAPTER 7: CONCLUSIONS		93
Code appendix		95
References		96

LIST OF FIGURES

1.1 Examples of pattern formation in reaction-diffusion and hydrodynamic systems.	
(a) The chemical elements Turing studied, called morphogens, are responsible for tissue pigmentation and form. The outcome of the pathways to instability he identified are particularly visible in nature, as in on the skin of this Giant Puffer fish.	
(b) A Kelvin-Helmholtz atmospheric instability visible in clouds. The KH instability occurs when there is shear between two layers of the same fluid or at the interface between two fluids moving with different velocities.	
(c) An aerial view of banded vegetation patterns in Niger. Such patterns arise in reaction-diffusion systems for vegetation growth in which rainfall is inhibited, such as the Klausmeier model (see [18]). Image courtesy of the US Geological Survey.	
(d) A vortex street visible in clouds off the coast of Chile, the result of vortex shedding as fluid flows around blunt objects.	
<i>Images (a), (b), and (d) from the Wikimedia Commons. Image (c) courtesy of the US Geological Survey.</i>	6
1.2 The towers and troughs phenomenon seen in (a) an experimental grassland fire [16] and (b) a top-down view of the vertical velocity output of a FIRETEC simulation, where dark red regions indicate strong updraft and dark blue regions indicate strong downdrafts [15].	7
1.3 In [17], particle image velocimetry data is used to capture the velocity field in the vicinity of a fire spreading radially from a point ignition. This image shows the magnitude of the horizontal velocity as time progresses. The actual fireline is the inner edge of the bright yellow region, as fire creates a warm low pressure front that pushes hot air up and entrains cool air. The “fire pockets” observed by the authors are seen in the second row of images: the black and white dots indicate fixed points of the underlying flow.	7
2.1 An example quasi-cubic reaction term with roots $u_0 = 0, u_1 = 0.5, u_2 = 1$, and its derivative.	9
2.2 Sketch of the stable and unstable subspaces and manifolds of a hyperbolic fixed point.	11
2.3 Phase portraits for the system (2.6) with (a) $c = 0$ and (b) $c = -1$. When $c = 0$, the system is Hamiltonian.	12
2.4 Phase space trajectories for the system (2.6) for (a) $c = -0.2$, (b) $c = -0.4$, (c) $c = 0$ and (d) $c = -0.305$. The unstable manifold initiated near $(0, 0)$ is indicated in pink and the stable manifold initiated near $(1, 0)$ is indicated in green. The trajectory in (d) shows the result of a successful implementation of the shooting method: a value of c has been found such that the stable and unstable manifolds coincide in a heteroclinic orbit connecting the two fixed points.	13
2.5 A graphical depiction of the elements of the resolvent set and the spectrum and a linear operator.	17
3.1 The nullclines of the first order system, excluding the s axis. The line $v = 0.25$ is indicated in red and the resulting (u, v) fixed points are indicated by black dots. All fixed points live in the $s = 0$ plane.	32
3.2 The singular orbit. In this depiction, the jump occurs at the knee of the nullcline. For other values of v_f , the jump occurs before the knee.	34

3.3	The reaction term for various values of v^* for (a) small v^* regimes and (b) large v^* regimes. The zeros of the reaction term are u_0, u_1 and u_2 . Note that, for $v^* \gg 0$, u_0 and u_1 are very close together relative to u_2 . Also note, in figure (a), that $v = 0.07$ is below the threshold for bistability.	35
3.4	Wave speed c as a function of fuel load	36
3.5	A schematic of the temperature pulse as a function of the spatial variable. Note the sharp, leading edge gradient in red followed by the gradual cooling on the tailing end, indicated in blue. In chapters 4 and 5, we focus on the traveling front consisting of the red “reaction” zone.	37
3.6	The essential spectrum of $\mathcal{L}^{-\infty}$ depicted as a plot of the real vs. the imaginary parts of λ_- as defined in (3.38).	40
3.7	(a) The contour of radius 1 on which the Evans function is evaluated, constructed to exclude the origin and (b) the Evans function output, illustrating the location of the zeros of the Evans function when evaluated on the contour shown in (a).	41
4.1	The fireline depicted as the boundary between regions of burning and unburned fuel in (a), then zoomed in to illustrate the transition zone between burning and unburned fuel in (b), then viewed again as a two-dimensional object in (c). The profile solutions we consider in this work correspond to the dotted black line in figure (c), asymptotically connecting regions of maximum and ambient temperature (corresponding to regions of burning and unburned fuel). The direction of motion of the fireline and the traveling wave is indicated by the red arrow(s) across all three figures.	43
4.2	Two possibilities for the spatially dependent wind configuration. The first illustrates a convergent wind field and the second a divergent wind field. The fireline is indicated in red.	47
4.3	The three-dimensional phase space described in §5. The blue plane is the stable manifold of the fixed point $(u_2, 0)$ for the system at $+\infty$ and the red plane is the unstable manifold of the fixed point $(0, 0)$ for the system at $-\infty$. The solid blue and red curves indicate the intersections of these manifolds with the plane $z = 0$. The point of intersection of the solid curves can be traced back across the unstable manifold and forward across the stable manifold to find the heteroclinic connection between $(0, 0)$ and $(u_2, 0)$	50
4.4	Invariant manifolds color-coded by wave speed value $c \in (-0.045, -0.125)$. (a) depicts type 1 intersections, while (b) depicts type 2 intersections for $c \in ()$. The fixed points $(0, 0)$, $(u_1, 0)$ and $(u_2, 0)$ are indicated in purple. Note the different qualitative nature of the intersections in (a) versus those in (b).	52
4.5	Phase portraits for the angular systems at $-\infty$ and $+\infty$ with a sample solution trajectory moving from θ_u^- to θ_s^+ . Unstable manifolds for each system are indicated in red and stable manifolds in blue.	56
4.6	Profile solutions found using the method described in §4.6, for $v^* = 0.1$, $l = 0.027$, $\alpha = 0.05$, $\beta = -\alpha$, color-coded by wave speed c . In this case, $u_2 \approx 2.5$	58
4.7	(a) shows the accumulated angle for a range of c values as a function of ω . Vertical jumps indicate the ω value that is an eigenvalue for that value of c and corresponding solution. (b) shows an alternate view of the same idea. The solution trajectories are color-coded by ω values. If the solution jumps by a factor of π as $z \rightarrow \infty$, the corresponding value of ω is an eigenvalue. It is worth noting that at the exact value of ω that is an eigenvalue, the solution in θ will not have a jump. The depicted solutions occur just after the eigenvalue.	58
4.8	The largest eigenvalue ω as a function of the phase γ in figure (a) and the wave speed c in figure (b). Both views demonstrate a clear minimum and an inverted parabolic structure.	59

4.9	Intersecting invariant manifolds for two wave speeds on either end of the allowed range as well as the preferred wave speed. The fireline occurs at the maximum value of s along the portion of the trajectory corresponding to the solution and is indicated by the black star. The wind switch occurs at the point of intersection of the manifolds and is indicated by the black dot. All intersections are type 1. (a) shows the intersection when c is very close to $\hat{c} + \beta$. The signed distance between the fireline and the wind switch is $\mathbf{d} = -0.82683$. (b) shows the intersection when c is very close to $\hat{c} + \alpha$, with $\mathbf{d} = 1.41559$. (c) shows the intersection for the preferred wave speed, $c = -0.08995$, with $\mathbf{d} = 0.58459$.	63
5.1	For an unperturbed system the front solutions studied in this chapter, indicated in purple, may be thought of as the result of taking the intersection of constant x planes with the two-dimensional front depicted in red and blue. As a function $u(y)$, the resulting solutions are constant. Recall that the profile solutions studied in Chapter 3 correspond to the dashed black line. For perturbations to which the system is unstable, we expect emergent transverse structure.	65
5.2	A schematic of the counter-rotational vortices along the fireline in the streamwise direction. The pattern of updrafts and downdrafts in the z direction is indicated by the blue and red arrows. The projection of the two-dimensional field on to the y axis is indicated by the purple arrows, illustrating the switching behavior in the transverse direction.	66
5.3	The accumulated angle for fixed $\beta_y = 1$ and a range of α_y values, zoomed in near $\alpha_y = 0$ to focus on the region of the jump. The dashed black line indicates the α_y value of the initial jump, at about 0.1. The dashed red lines are at $y = 0, \pi$ and the dotted red curve indicates the eigenvalue condition (5.20), which varies as a function of α_y . Note that the accumulated angle tracks this condition before jumping.	71
5.4	A contour plot of the accumulated angle $\Delta\theta$ as a function of α_y and β_y . Solid red indicates an accumulated angle of π and, therefore, parameter regions for which a positive eigenvalue exists. (b) is a contour plot of θ_f and demonstrates the gradient of changes in the angle as a function of the parameter values. Note the symmetry with respect to the line $\alpha_y = -\beta_y$, which is to be expected because of the parity of the tanh function used to define the wind.	72
5.5	Eigenvalues found using the method described in §4.6 for $\alpha_y \in [-2, 2]$ and $\beta_y \in [-2, 2]$. The largest positive eigenvalue for this range of parameters, rounded to four decimal places, is $\mu_{max} = 1.9965$ and occurs for $\alpha_y = -2.0$, $\beta_y = 1.5556$.	73
5.6	Transverse eigenfunctions $\eta(y)$ for $\alpha_y = 1$ and $\beta_y = -0.5$ with a range of guesses for the eigenvalue parameter μ . The eigenvalue corresponding to each eigenfunction is listed in the legend. The eigenfunction with no zeros corresponds to the largest eigenvalue, as expected.	73
5.7	Regions of positive and negative values of the eigenvalue λ of the two dimensional problem, found as the sum of the transverse and streamwise eigenvalues $\lambda = \mu + \omega$ for $\alpha_y \in [-2, 2]$ and (a) $\beta_y = 0.5$ and $\alpha_x = \alpha_y \in [.03, .7]$ and (b) $\beta_y = -0.5$ and $\alpha_x \in [.03, .7]$.	75
5.8	Contour plots of the two-dimensional eigenfunctions when (a) both the transverse and streamwise winds are constant in space, resulting in $\lambda = \mu + \omega = -0.0002 + 0 < 0$ and (b) both the transverse and streamwise winds switch in space, resulting in $\lambda = \mu + \omega = 0.9989 - 0.0012 > 0$.	77
5.9	The two-dimensional spatial eigenfunction $p(z, y)$, found as the product of the streamwise and transverse eigenfunctions $q(z)$ and $\eta(z)$, for the parameters $\alpha_x = 0.05$, $\alpha_y = 1$, $\beta_y = -0.5$. (a) and (b) depict the eigenfunction for the largest transverse eigenvalue, $\mu = 0.99898$, whereas (c) and (d) depict the higher-order harmonics associated with $\mu = 0.99080$, the second largest eigenvalue.	78

6.1	Computational fluid dynamics simulations of the vertical velocity w generated by fluid flowing over a constant heat source outputting 775 KW of heat energy in an x/y domain. The imposed wind velocity is (a) 03m/s and (b) 06m/s. The characteristic pattern of updrafts and downdrafts is visible. The vertical velocity ranges from 1.8m/s (in yellow) to -1.8m/s (in blue). Simulations conducted by the author using FIRETEC [9].	80
6.2	The system investigated in this chapter, in which fluid moving with velocity c_w flows over a hot plate moving with velocity c_f . We aim to characterize the conditions under which counter-rotational vortices, indicated in blue and purple, emerge in the velocity field along the length of the hot plate.	81
6.3	The real part of the spatial eigenfunction $w(x,y,z)$ for fixed $z = 0.5$ and $j = k = n = 1$. Note the growth of the eigenfunctions in the x direction and the periodicity in the y direction. (b) shows the same eigenfunction but for an x domain that cuts off halfway across the hot plate, illustrating the sinusoidal pattern of updrafts and downdrafts.	88
6.4	Contour plots of the eigenfunctions $w(x,y,z)$ for $j = k = 1$ and $n = 2$ and (a) $\sigma = 0$, (b) $\sigma = 0.5$, (c) $\sigma = 1$ and (d) $\sigma = 2$ for fixed $z = 0.5$, halfway up the vertical domain.	89
6.5	The spectrum for $\sigma = -1$ and $R = 0$: in other words, $\text{Re}(s)$ vs. $\text{Im}(s)$ parameterized as a function of j . In this case, at least one of the terms on the left hand side of (6.40) must be zero: it cannot be the first, due to a disagreement of signs. The second term yields s entirely real and gives us the spectrum along the imaginary axis in blue. The third term gives us both real and imaginary parts of s , where the imaginary parts correspond to $\pm k$ and are indicated in red.	90
6.6	The spectrum for $\sigma = 0$ is entirely real. In (a), $R = 1.25$ and, in (b), $R = 5$. Note that the steady-state bifurcation occurs for R_c between these values: the exact value may be found using a root-finding method. The spectrum for $\sigma = -1$ with (c) $R = 1.25$ and (d) $R = 6$ exhibits a Hopf bifurcation for some R_c between these values, as does the spectrum for $\sigma = -3$ with (d) $R = 6$ and (e) $R = 30$. Note that the bifurcation occurs for a much larger R_c compared to the R_c found when $\sigma = -1$	91

CHAPTER 1

Introduction

Wildfires are an issue of increasing societal, economic and environmental importance, particularly to the inhabitants of the American West. According to the National Interagency Fire Center [1], wildfires in the United States burned a total of 7.6 million acres in 2022, an area approximately equivalent to the land mass of the state of Rhode Island. In 2023, this number was down significantly, to 2.7 million acres—but 2023 was an anomalous year, and the trend has been one of steady increase for the last 40 years. An undeniably urgent need exists to better understand the dynamics of wildfires. Current research spans the often intersecting fields of observational methods, data collection and analysis, numerical simulation, and analytic investigation of the underlying physical systems. The physics, chemistry and fluid dynamics of wildfires are complex: as such, they present a challenging modeling task and a rich testbed for exploring emergent phenomena and novel mathematics.

1.1 A brief overview of wildland fire modeling

To contextualize this work, we begin by discussing historical and present-day modeling efforts. Fire propagation is a multi-scale, multi-physics problem: models attempting to resolve the processes involved must begin with the transport equations and capture a number of additional interacting effects, including wind, topography and slope, fuel moisture and heterogeneity, and atmospheric coupling. According to a series of encyclopedic review articles by Andrew Sullivan, an Australian physicist and the leader of CSIRO’s Bushfire Behavior and Risks team, modeling approaches may be broadly classified as one of three types: empirical, physical, and mathematical analogues [2]–[4].

Empirical models use statistical approaches and data from experimental fires, whereas physical models represent both the physics and chemistry of fire. Most empirical models are in fact quasi-empirical, with some basis in a physical framework. The famous Rothermel model, developed at the Northern Forest Fire Laboratory (now the Missoula Fire Lab) in the 1970s is an example [5]. Many relatively modern simulation tools, including FARSITE, FlamMap, and BehavePlus, are based on Rothermel’s fire spread calculations [6]–[8]. Though they have some basis in the principles of conservation of energy, these quasi-empirical

models generally do not differentiate between modes of heat transfer, nor do they account for atmospheric coupling.

Most physical models, on the other hand, are in fact quasi-physical and contain parameterizations that make them at least somewhat empirical. Today's state-of-the-art fire modeling tools¹ are largely physics-based, use massive computational resources to solve the equations of computational fluid dynamics on three-dimensional domains, and are capable of incorporating complex topography, fuel beds and atmospheric interactions. HIGRAD/FIRETEC, a coupled fire-atmosphere model that solves the three-dimensional transport equations and captures the effects of combustion, drag, turbulence and atmospheric interactions, is the foremost example [9]. Models such as FIRETEC are capable of recreating fire phenomena in impressive detail. However, the high level of complexity of a largely physics-based model can serve to obscure the physical and mathematical mechanisms underlying phenomena of interest. When used in an exploratory, scientific manner rather than as a prognostic tool, such models are generally subject to a number of simplifying assumptions to allow researchers to study idealized situations.

On the other end of the spectrum are Sullivan's so-called "mathematical analogue" models, in which equations for fire spread are based largely on mathematical principles as opposed to purely physical principles. Examples include Hyugen's principle of elliptical spread [10], level-set methods for front tracking [11], cellular automata (dating back to [12]), and reaction-diffusion type models, which we discuss further in the introduction to Chapter 3. Of course, as with the other two categories of classification, these models typically include physical and empirical elements. In order to be analytically tractable, many of these approaches reduce the complexity of the fire system by a dramatic degree. The benefit of these simplified models is that they allow researchers to focus on the interactions of a limited set of physical processes and study the resulting (often decidedly un-simple) behavior in a rigorous manner.

1.2 The mechanisms of pattern formation

Pattern formation refers to the tendency towards self-organization in complex systems. The mathematical study of pattern formation is concerned with both the properties of these (generally spatial) patterns and the mechanisms behind their formation. The field has its roots in Alan Turing's seminal 1952 paper, "The chemical basis of morphogenesis," in which Turing demonstrates that the interaction between reacting and

¹It is worth noting that, with the increasing dominance of data-driven methods and accelerating demand for fast-running models, this standard is rapidly changing.

diffusing chemical elements in biological tissue leads to destabilization of the homogeneous equilibrium and transition of the system to a new, ordered equilibrium state [13]. In particular, Turing found that a homogeneous equilibrium can be simultaneously stable to homogeneous perturbations and unstable to specific spatially dependent perturbations. This results in a supercritical bifurcation leading to a spatially dependent steady state—in other words, a spatial pattern [14].

Pattern formation is also frequently observed in hydrodynamical systems, though the language used is somewhat different. A large number of hydrodynamic instabilities have been studied and classified, including the Rayleigh-Taylor instability, the Kelvin-Helmholtz instability, Görtler vortices, Kármán vortex streets, Rayleigh-Bénard convection, and others. While some hydrodynamic instabilities yield patterns of standing waves, such as Faraday waves, many of the resulting phenomena are transient. As in a system of reaction-diffusion equations, the onset of instability corresponds to the transition of the system from an equilibrium state, through a marginally stable state and in to another steady, patterned state. These transitions occur in response to a changing parameter (often a non-dimensional quantity such as the Reynolds number or the Prandtl number) that causes a bifurcation. Examples of pattern formation seen in nature in both reaction-diffusion and hydrodynamic systems can be found in figure 1.4.

Common to both fields is the identification of a threshold state—when the system is on the cusp of transitioning from one equilibrium to the next—and the study of the conditions that precipitate such a state. In the next section, we introduce a handful of phenomena from the field of fire science that may be understood through the lens of pattern formation. Then, for the remainder of this thesis, we explore pathways to instability in two mathematical systems that capture salient features of these pattern-forming physical systems.

1.3 Phenomena of interest

The formation of coherent structures in the velocity field in the vicinity of a propagating fire has long been of interest to the fire science community. These structures are characterized by alternating patterns of updrafts and downdrafts, referred to as “coherent streaks” by some authors and “towers and troughs” by others (see [15], [16]). The towers and troughs moniker comes from observations of the phenomenon in landscape-scale fires, in which the updrafts and downdrafts in the local velocity field lead to visible “towers” of flame and “troughs” devoid of flame. The formation of these structures is due to counter-rotational vortices that emerge along the length of a fireline, the effect of which is to push hot air up and pull cool air down in an alternating pattern. The resulting gaps in the fireline allow for convective heat transfer from air heated by the burning fuel on to unburned fuel, creating the conditions necessary for its ignition. This phenomenon has

been observed across a wide range of scales in simulated fires, experimental fires and landscape-scale burns.

Similar pattern-forming mechanisms have been observed in radial spot fires [17]. In an experiment conducted at the Southern Research Station in Athens, Georgia, particle velocimetry data was used to track the evolution of a fire spreading radially outward from a point ignition under calm ambient wind. Both velocity and temperature data captured the disintegration of the fireline and the formation of discrete “fire pockets,” apparently in response to instabilities in the underlying flow field. In particular, the pockets appear to be spatially confined to fixed points of the flow. The mechanisms by which these structures emerge in the underlying flow field are not immediately evident and the authors call for further investigation of the nonlinear system’s dynamical behavior.

1.4 Questions addressed in this thesis

The emergence of such coherent structures in models of fire spread is generally attributed, at least in part, to buoyant flow instabilities. The spatial structures these instabilities beget may be observed in the resulting velocity and temperature fields. In this thesis, we explore two mathematical models chosen because of their potential to capture key elements of the pattern-forming systems highlighted in the preceding section.

In Chapter 3, we introduce a two-dimensional model for the temperature and fuel concentration of a region through which a fire is moving. This model is intended to capture a (spatially, not dynamically) linear view of the radial spot fires just discussed, though some of the resulting behavior resembles the flow instabilities that typify the towers and troughs phenomenon. A key aspect of the model is the inclusion of a spatially dependent wind term describing a “switch” in the velocity field near the fireline. The local behavior of equilibria may be understood by linearizing the equations about solutions of interest: this linearization allows us to study the spatial dynamics in isolation.

In Chapter 4, we investigate the dynamics parallel to the fire’s direction of motion in the presence of a wind switch. Using geometric dynamical systems methods, we find that the spatially dependent forcing term has an important impact on the existence and stability of solutions, representing a departure from classical theory. We find conditions for the existence of traveling fronts, classify the fronts based on their stability characteristics, and develop a mechanism by which to identify the fronts that are “preferred” in a physical and spectral sense.

In Chapter 5 we turn to the transverse dynamics, again motivating the use of a spatially dependent wind term (slightly different from that considered in Chapter 4) by interpretation of a physical system. Using tools developed in the previous chapter, we identify parameter regimes for which positive eigenvalues are expected

to exist. After finding these positive eigenvalues, we incorporate our analysis in to the full, two-dimensional problem to identify regions of spatial instability for the original system. Finally, we visualize the resulting spatial pattern formation by way of the eigenfunctions of the two-dimensional system.

Lastly, in Chapter 6, we introduce a version of the classical model of Rayleigh-Bénard convection modified to include an advection term representing the environmental wind. By reducing the effect of combustion to only the heat energy added to the system, thought of as a “hot plate” underneath the channel of fluid, this model allows us to test the hypothesis that coherent structures such as towers and troughs emerge as the result of thermally driven buoyancy. By way of a normal mode analysis, we obtain the spectrum of the corresponding operator and note that the nature of the bifurcation—the point at which the spectral curves move through the imaginary axis in to the right half-plane—is qualitatively different from the bifurcation seen in classical Rayleigh-Bénard convection. Lastly, we visualize the resulting eigenfunctions and note that they emulate the pattern of updrafts and downdrafts observed in the towers and troughs phenomenon.

Throughout this thesis, we aim to understand how physically motivated external forcings, either in the form of a wind term or a heat energy input, give rise to spatial pattern formation in models of fire propagation. In doing so, we apply the tools of geometric dynamical systems theory to two simple but highly physically motivated models of fire propagation in a way not seen in existing literature: in particular, the model we consider in Chapters 3-5 does not assume a system insulated from heat loss and does allow for spatial variation of the wind. The study of pattern-forming physical systems consists of a number of components, such as: identifying relevant physical systems, analyzing the onset of instability, characterizing the resulting bifurcations, and describing the structure of emergent patterns. Our work focuses on the role of mechanisms of instability in this chain of inquiry. Our goal is not to reproduce the patterns in question, but to use mathematical methods to shed light on the physical underpinnings of pathways to instability.

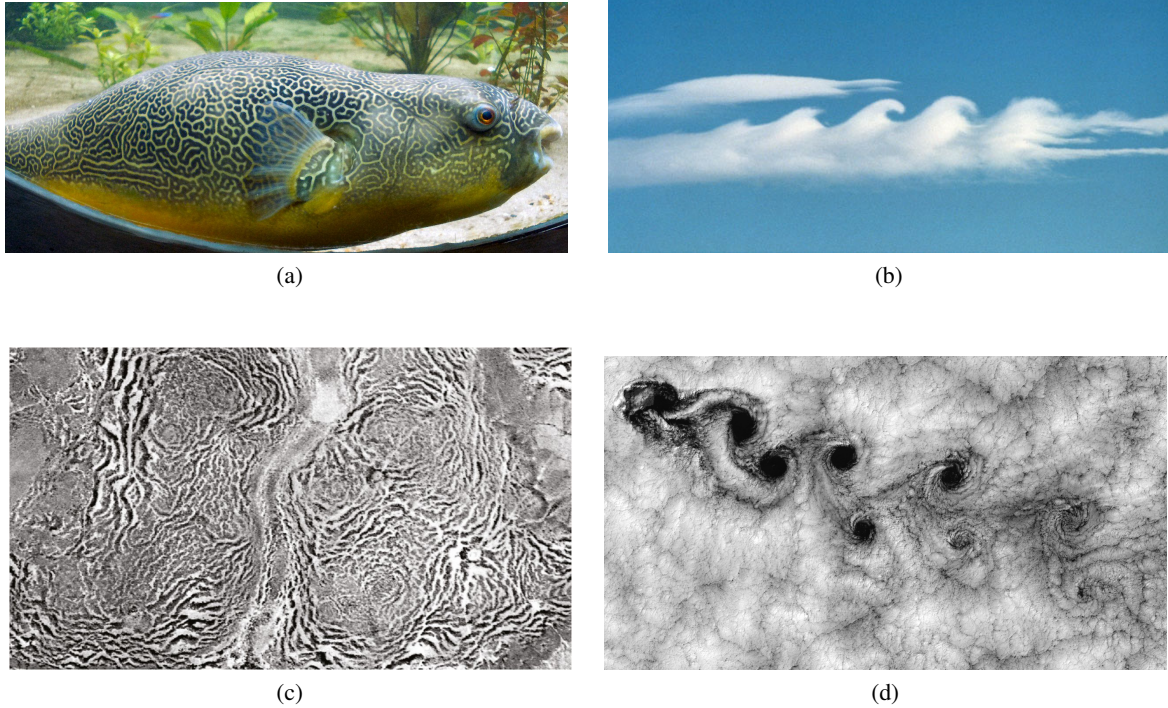


Figure 1.1: Examples of pattern formation in reaction-diffusion and hydrodynamic systems.

- (a) The chemical elements Turing studied, called morphogens, are responsible for tissue pigmentation and form. The outcome of the pathways to instability he identified are particularly visible in nature, as in on the skin of this Giant Puffer fish.
- (b) A Kelvin-Helmholtz atmospheric instability visible in clouds. The KH instability occurs when there is shear between two layers of the same fluid or at the interface between two fluids moving with different velocities.
- (c) An aerial view of banded vegetation patterns in Niger. Such patterns arise in reaction-diffusion systems for vegetation growth in which rainfall is inhibited, such as the Klausmeier model (see [18]). Image courtesy of the US Geological Survey.
- (d) A vortex street visible in clouds off the coast of Chilé, the result of vortex shedding as fluid flows around blunt objects.

Images (a), (b), and (d) from the Wikimedia Commons. Image (c) courtesy of the US Geological Survey.

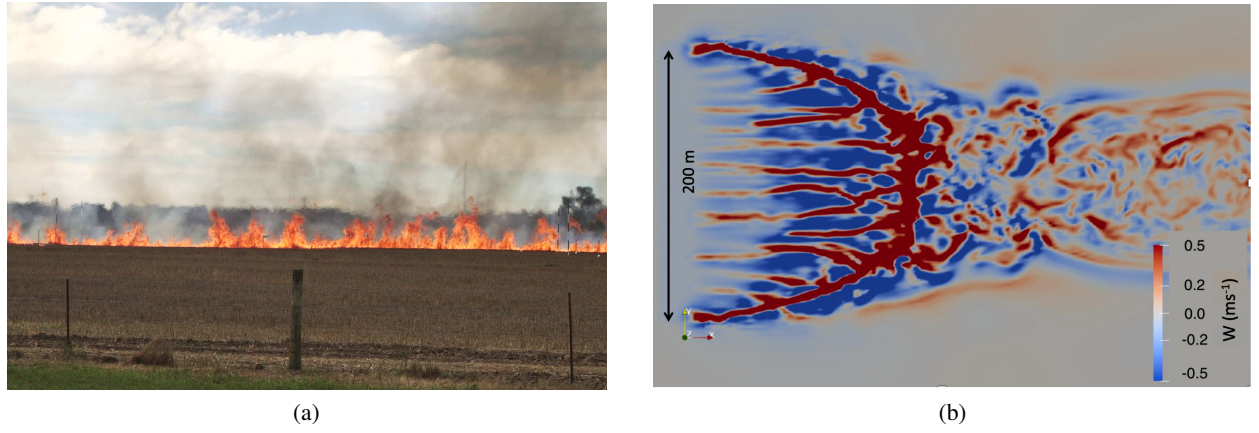


Figure 1.2: The towers and troughs phenomenon seen in (a) an experimental grassland fire [16] and (b) a top-down view of the vertical velocity output of a FIRETEC simulation, where dark red regions indicate strong updraft and dark blue regions indicate strong downdrafts [15].

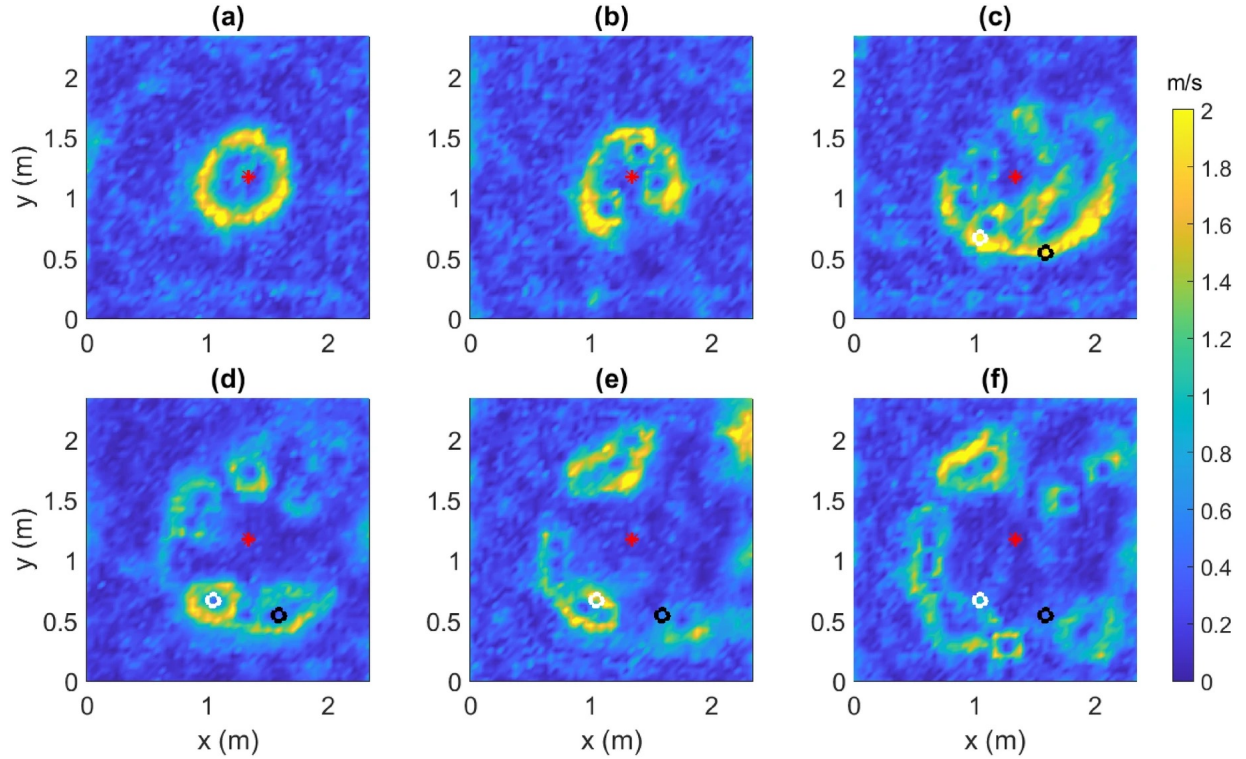


Figure 1.3: In [17], particle image velocimetry data is used to capture the velocity field in the vicinity of a fire spreading radially from a point ignition. This image shows the magnitude of the horizontal velocity as time progresses. The actual fireline is the inner edge of the bright yellow region, as fire creates a warm low pressure front that pushes hot air up and entrains cool air. The “fire pockets” observed by the authors are seen in the second row of images: the black and white dots indicate fixed points of the underlying flow.

CHAPTER 2

Background and methods

The model we introduce in Chapter 3 and analyze for the remainder of this dissertation contains an example of a bistable reaction-diffusion equation (RDE). We will study both scalar and non-constant coefficient variants. In the scalar case the existence of traveling wave solutions is well known and, in the next section, we discuss the existence of such solutions for a general equation. We seek to understand traveling wave solutions as heteroclinic connections in the phase space of the system of ODEs corresponding to the traveling wave equation, which may be derived from the reaction-diffusion PDE in question. The framework we establish for the scalar problem will be used to guide our analysis when we consider RDEs with spatially dependent coefficients.

2.1 A dynamical systems view of traveling waves

Consider the reaction diffusion equation with constant coefficients defined on the real line

$$u_t = u_{xx} + f(u) \quad (2.1)$$

where the reaction term $f : \mathbb{R} \rightarrow \mathbb{R}$ has a “quasi-cubic” shape. In particular, we require $f \in C^0$ and

- (a) $f(u_0) = f(u_1) = f(u_2) = 0$, $u_0 < u_1 < u_2$
 - (b) $f < 0$ on (u_0, u_1) , $f > 0$ on (u_1, u_2)
 - (c) $f'(u_0) < 0$, $f'(u_2) < 0$
 - (d) $\int_0^{u_2} f(z) dz > 0$
- (2.2)

For illustrative purposes, we might consider the function

$$f(x) = -(2x - 1)^3 + (2x - 1) \quad (2.3)$$

with $u_0 = 0$, $u_1 = 0.5$, and $u_2 = 1$. Existence and uniqueness of solutions to systems of the form (2.1) in

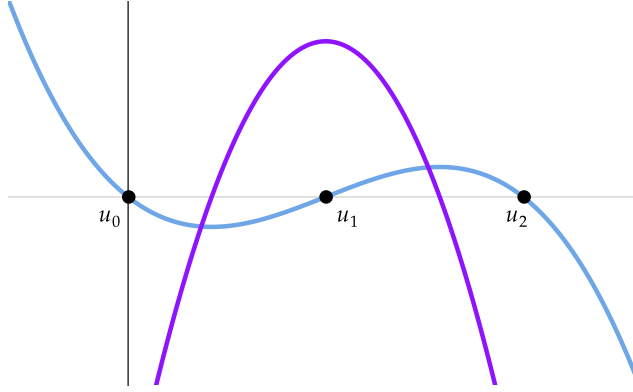


Figure 2.1: An example quasi-cubic reaction term with roots $u_0 = 0, u_1 = 0.5, u_2 = 1$, and its derivative.

general follows from the fact that, assuming a sufficiently smooth reaction term $f(u)$, the associated vector field is Lipschitz. Our goal is to demonstrate the existence of traveling wave solutions of the form

$$u(x, t) = v(x - ct) = v(z) \quad (2.4)$$

where v is the wave profile and c is the wave speed. We will focus specifically on traveling fronts, so that v satisfies boundary conditions

$$\lim_{z \rightarrow -\infty} v = 0 \quad \text{and} \quad \lim_{z \rightarrow +\infty} v = 1 \quad (2.5)$$

Substituting the traveling wave ansatz (2.4) into (2.1) and noting that front solutions must be independent of time yields a nonlinear ODE which, in first order form, is

$$\begin{aligned} v' &= w \\ w' &= -cw - f(v) \end{aligned} \quad (2.6)$$

with boundary conditions

$$\lim_{z \rightarrow -\infty} (v, w) = (0, 0) \quad \text{and} \quad \lim_{z \rightarrow +\infty} (v, w) = (1, 0) \quad (2.7)$$

The system (2.6) has fixed points at $(u_0, 0), (u_1, 0)$ and $(u_2, 0)$. In our example, these are $(0, 0), (0.5, 0)$ and $(1, 0)$. The fixed points at $(0, 0)$ and $(1, 0)$ are hyperbolic. To see this, consider the linearization of (2.6),

where $F(v, w) = w$ and $G(v, w) = -cw - f(v)$:

$$Df(v, w) = \begin{pmatrix} \frac{\partial F}{\partial v} & \frac{\partial F}{\partial w} \\ \frac{\partial G}{\partial v} & \frac{\partial G}{\partial w} \end{pmatrix} = \begin{pmatrix} 0 & 1 \\ -f'(v) & -c \end{pmatrix} \quad (2.8)$$

The eigenvalues of the linearization evaluated at $(0, 0)$ or $(1, 0)$ are

$$\lambda_0^\pm = \frac{-c \pm \sqrt{c^2 + 16}}{2} \quad \text{and} \quad \lambda_1^\pm = \frac{-c \pm \sqrt{c^2 + 8}}{2} \quad (2.9)$$

for f as in (2.6). We note that, for all values of c , $\operatorname{Re}(\lambda) \neq 0$ and the corresponding fixed points are therefore hyperbolic. This result holds for any function $f(v)$ satisfying the conditions (2.2). Hyperbolic fixed points of linear systems of ODEs have stable and unstable subspaces, denoted E^s and E^u , which are given by the eigenvectors of the matrix associated with the system evaluated at the fixed point, which define the lines

$$\{w_0 = \lambda_0^+ v_0\} \equiv E^u \quad \text{and} \quad \{w_1 = \lambda_1^- v_1\} \equiv E^s \quad (2.10)$$

E^u and E^s are invariant under the dynamics of the linear system. The following theorem allows us to infer information about the local dynamics of the nonlinear system from the dynamics of the corresponding linear system.

Theorem 2.1.1 (Hartman-Grobman). *Let x^* be a hyperbolic fixed point of a C^1 vector field $f(x)$ with flow $\varphi_t(x)$. Then, there is a neighborhood N of x^* such that φ is topologically conjugate to its linearization on N .*

Theorem 2.1.1 allows us to conclude that E^u and E^s are invariant under the dynamics of the nonlinear system in some neighborhood N of each of the hyperbolic fixed points $(0, 0)$ and $(1, 0)$. Moreover, for the nonlinear system, there exist invariant sets in the form of smooth manifolds tangent to the unstable and stable subspaces of the corresponding linear system as illustrated in figure 2.2. There are many statements of the primary result on the existence of invariant manifolds for nonlinear hyperbolic systems: we borrow the following statement from [19].

Theorem 2.1.2 (Local Stable Manifold Theorem). *Given $f(x)$ a smooth vector field on \mathbb{R}^n and x^* a hyperbolic fixed point, there exists a k -dimensional manifold $W^s(x^*)$ and an $n - k$ -dimensional manifold $W^u(x^*)$ such that the following hold:*

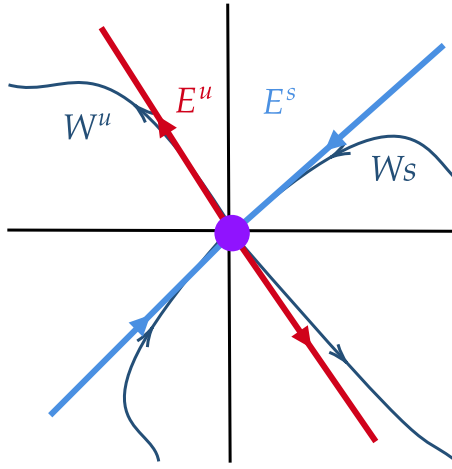


Figure 2.2: Sketch of the stable and unstable subspaces and manifolds of a hyperbolic fixed point.

1. *$W^s(x^*)$ and $W^u(x^*)$ are both locally invariant under the dynamics of $f(x)$ and contain the point x^* .*
2. *The tangent space to $W^s(x^*)$ at x^* is E^s and the tangent space to $W^u(x^*)$ at (x^*) is E^u .*
3. *If $x \in W^s(x^*)$ then the solution trajectory with initial condition x tends to x^* as $t \rightarrow \infty$ and if $x \in W^u(x^*)$ then the solution trajectory with initial condition x tends to x^* as $x \rightarrow -\infty$.*
4. *The manifolds $W^s(x^*)$ and $W^u(x^*)$ are locally unique and determined by the above conditions.*

Theorems 2.1.2 and 2.1.1, together with the fact that systems of type (2.1) with reaction terms satisfying (2.2) admit two hyperbolic fixed points, implies the existence of a stable and unstable manifold, as described in Theorem 2.1.2, for the fixed points at $(0,0)$ and $(1,0)$. These theorems hold for finite-dimensional systems: in other words, systems of ODEs. The proofs of the infinite-dimensional analogues for systems of PDEs may be found in [20] and [21].

For parameter ranges in which $W^u(x_0^* = (0,0))$ and $W^s(x_1^* = (1,0))$ intersect—or even coincide—a **heteroclinic orbit** exists asymptotically connecting the two fixed points. Coincidence of trajectories occurs for autonomous systems: if the phase space is two-dimensional, then invariant manifolds are one-dimensional. The intersection of one-dimensional manifolds is again a one-dimensional manifold. It follows that, if the manifolds intersect, they must coincide (unless this intersection occurs at a fixed point, in which case the dimension of the invariant subspace is again decreased).

A standard phase plane analysis (see [22]) demonstrates the existence of this heteroclinic orbit for a

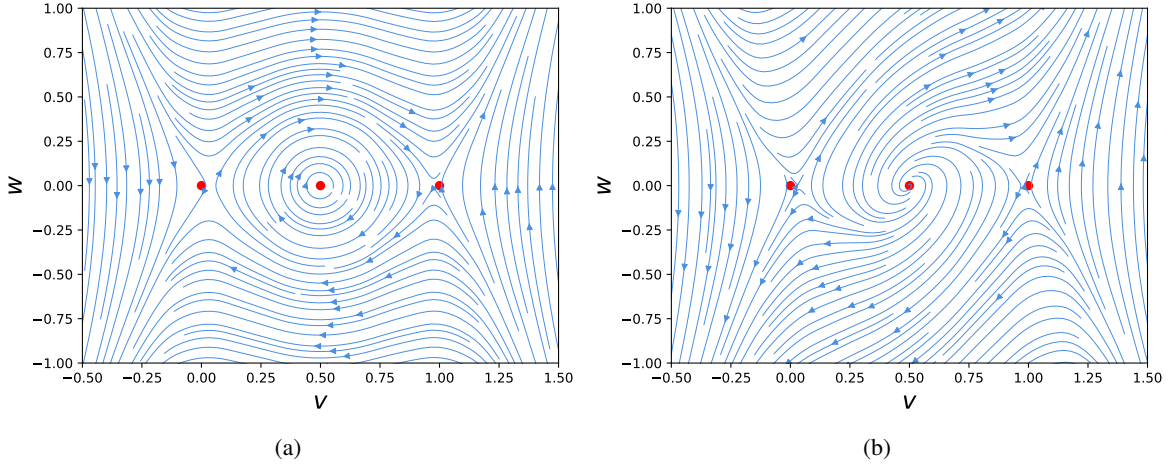


Figure 2.3: Phase portraits for the system (2.6) with (a) $c = 0$ and (b) $c = -1$. When $c = 0$, the system is Hamiltonian.

unique wave speed $c^* < 0$ in bistable systems. In particular, for (2.6), we have:

$$W^u(x_0^*, c^*) = W^S(x_1^*, c^*) \quad \text{for} \quad \{v > 0, w > 0\} \quad (2.11)$$

So that, for this c^* , a solution exists to the ODE (2.6) and a traveling wave solution of the form (2.4) exists to the PDE (2.1).

2.2 Computational methods for finding traveling waves

Oftentimes, the most straightforward way to understand the conditions for existence and qualitative properties of a traveling wave solution is to numerically compute the solution. In the next section, we discuss two methods for doing so.

2.2.1 In phase space

Recall that a traveling wave solution of the form (2.4) must satisfy boundary conditions (2.7) as the independent variable $z \rightarrow \pm\infty$. In phase space, where $v' = w$, this condition translates to $(v, w) \rightarrow (0, 0)$ as $z \rightarrow -\infty$ and $(v, w) \rightarrow (1, 0)$ as $z \rightarrow +\infty$. One way to conceptualize this boundary value problem is as two initial value problems. This is known as a **shooting method**: we solve the initial value problem with different values of the wave speed parameter c until we find a value of c for which the solution to either initial value problem also satisfies the omitted boundary condition. As an initial condition, we use the value of the fixed point at either boundary perturbed in the direction of the unstable or stable subspace, as appropriate.

Example 2.2.1. Consider system (2.6) and the eigenvalues of the corresponding linearization about the fixed

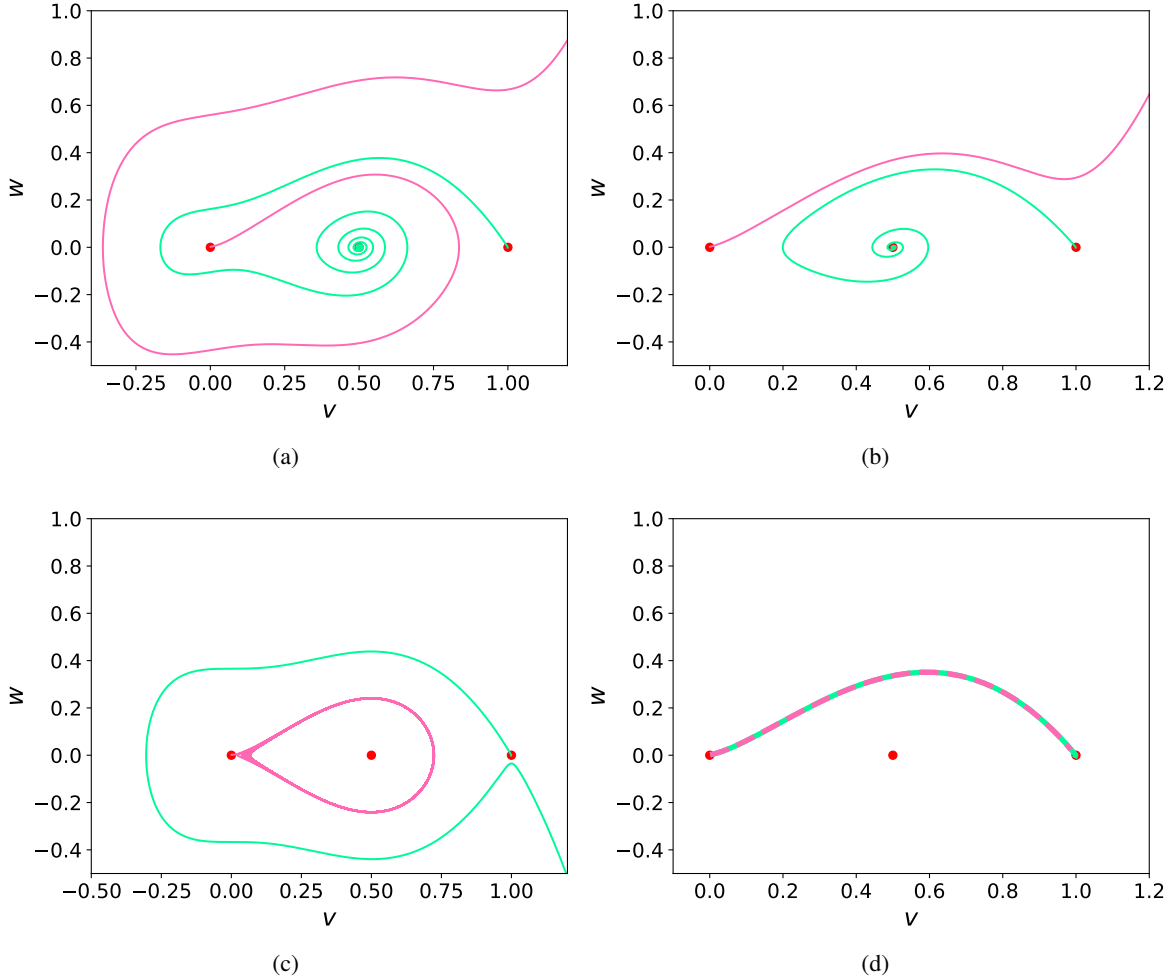


Figure 2.4: Phase space trajectories for the system (2.6) for (a) $c = -0.2$, (b) $c = -0.4$, (c) $c = 0$ and (d) $c = -0.305$. The unstable manifold initiated near $(0,0)$ is indicated in pink and the stable manifold initiated near $(1,0)$ is indicated in green. The trajectory in (d) shows the result of a successful implementation of the shooting method: a value of c has been found such that the stable and unstable manifolds coincide in a heteroclinic orbit connecting the two fixed points.

points $(0,0)$ and $(1,0)$, given in (2.9). We formulate the **forward problem** with the initial condition (v_0^f, w_0^f) and the **backward problem** with the initial condition (v_0^b, w_0^b) , defined as

$$(v_0^f, w_0^f) = (0,0) + \varepsilon v_0^+ \quad \text{and} \quad (v_0^b, w_0^b) = (1,0) + \varepsilon v_1^- \quad (2.12)$$

for $\varepsilon \ll 1$, where

$$v_0^+ = \begin{pmatrix} 1 \\ \lambda_0^+ \end{pmatrix} \quad \text{and} \quad v_1^- = \begin{pmatrix} -1 \\ \lambda_1^- \end{pmatrix} \quad (2.13)$$

are the eigenvectors corresponding to the unstable and stable subspaces E^u and E^s . Our aim is to numerically find the unstable and stable manifolds W^u and W^s tangent to these subspaces at the appropriate fixed points for a range of c , then find the value of c for which they coincide.

The forward problem is defined for $z \in [0, L]$ and the backward problem for $z \in [0, -L]$, where L must be chosen large enough to capture the long-term dynamics. Using a numerical integrator (in this case, SciPy's `SOLVE_IVP`), we integrate forward in the dependent variable z from (v_0^f, w_0^f) and backward in z from (v_0^b, w_0^b) . The results are summarized in figure 2.4. Of interest is the case when $c = 0$ and the system is Hamiltonian, as seen in figure 2.4(c).

2.2.2 As a boundary value problem

Alternatively, we can solve the original boundary value problem. What follows is the method outlined in [23], which we use for most boundary value problem calculations in this work. Consider the problem

$$\frac{dU}{dz} = f(U(z)), \quad U \in \mathbb{R}^n, \quad \lim_{z \rightarrow \pm\infty} U = U_{\pm} \quad (2.14)$$

In the context of the example problem studied in the preceding sections, we have $U = (v, w)$ and $n = 2$. We solve the two-point boundary value problem on the infinite domain $z \in (-\infty, \infty)$. Our aim is still to connect the unstable manifold from $-\infty$ to the stable manifold from $+\infty$. To that end we employ **projective boundary conditions** at $\pm L$:

$$P_{\pm}(U(\pm L) - U_{\pm}) = 0 \quad (2.15)$$

where $\pm L$ is our numerical approximation to $\pm\infty$ (meaning it is necessary to take L sufficiently large to capture the behavior near the ends of the domain). There exists a family of solutions parameterized by the wave speed c due to translational invariance. To select for the unique solution corresponding to one parameter value, we employ a centering condition in the form of an initial boundary condition at $z = 0$. Generally, we will choose to center the wave here, specifying that

$$U(z = 0) = (U_- + U_+)/2 \quad (2.16)$$

The addition of (2.16) turns our two-point BVP into a three-point BVP. A number of pre-packaged solvers exist for two-point BVPs, so it is convenient to transform our new three-point BVP back into a two-point BVP by doubling the size of the system and halving the domain. Lastly, to account for the unknown wave

speed parameter, we augment the system with the additional relation $c' = 0$. This results in the system

$$\begin{pmatrix} U \\ V \\ c \end{pmatrix}' = \begin{pmatrix} f(U) \\ -f(V) \\ 0 \end{pmatrix}, \quad z \in [0, L], \quad U, V \in \mathbb{R}^n \quad (2.17)$$

with (2.16) and (2.15) giving us the requisite $2N + 1$ boundary conditions. Lastly, we require a reasonable initial guess: for a front solution, a hyperbolic tangent function generally works well. We then complete the calculation using, e.g., SciPy's `SOLVE_BVP` or Matlab's `BVP4C`, both of which employ a fourth-order collocation method. The latter has built-in functionality for dealing with a free parameter, so we do not need to include the additional relationship $c' = 0$.

2.3 Stability

In the context of traveling waves, stability generally means that a wave maintains its shape in space as it propagates in time. In particular, perturbations to the wave decay to the wave or a translate thereof. In the infinite-dimensional function space associated with solutions of a PDE, a traveling wave solution and its translates exist as a curve of fixed “points,” where each fixed point is in fact an equilibrium solution of the evolution equation. Traveling wave stability is a stricter version of the concept of orbital stability; perturbations to a traveling wave converge to one of these fixed points representing translates of the wave, rather than to the entire curve of fixed points [20].

In the absence of stability, small (in the norm corresponding to the appropriate function space) environmental disturbances may be amplified, leading to markedly different behavior of the solution or a transition to a different system state entirely. Stability analysis is therefore a useful tool for determining when a traveling wave solution will persist in nature.

Consider the PDE

$$u_t = Au + F(u) \quad (2.18)$$

where $u(x, t) \in X$ is a Banach space, $A : D(A) \subset X \rightarrow X$ is a closed linear operator, and $F : X \rightarrow X$ is a nonlinear operator. To understand the stability of stationary solutions $\tilde{u}(x)$ to (2.18), we would like to understand the behavior of perturbations to that stationary solution, which requires locating the spectrum of A . Such a task might emerge in the context of a nonlinear problem, such as the primary problem considered in this thesis, as the result of linearizing a nonlinear operator about a stationary solution.

Determining the spectrum of the operator A associated with a PDE is more difficult than the analogous problem in ODEs because, even when evaluated at a stationary solution, the operator A likely still has spatial dependence. This means that A acts on an infinite dimensional space, as opposed to a finite dimensional space. The problem of finding the spectrum of A is therefore akin to the problem of finding solutions to non-autonomous ODEs, which is notoriously difficult.

Definition 2.3.1. The **spectrum** of the operator A is the complement of its **resolvent set** in the complex numbers, $\sigma(A) = \mathbb{C} \setminus \rho(A)$, where the resolvent set is defined as

$$\rho(A) = \{\lambda \in \mathbb{C} \mid (A - \lambda I) : D(A) \rightarrow X \text{ is bijective}\} \quad (2.19)$$

Bijectivity requires that A have a bounded inverse, by way of the closed graph theorem. There are a number of ways for $(A - \lambda I)$ to fail to have a bounded inverse and for λ to therefore be in the spectrum:

1. $A - \lambda I$ could have a non-trivial null space, but still have an (unbounded) inverse
2. $A - \lambda I$ could have a range that is not closed in X
3. $A - \lambda I$ could have a range that is not dense in X

Items (2) and (3) are unique to the infinite-dimensional case and therefore are only relevant for PDEs. The way in which $A - \lambda I$ fails to have a bounded inverse determines what subset of the spectrum it falls into.

Definition 2.3.2. A number $\lambda \in \mathbb{C}$ is an **eigenvalue** of A if there exists $v \in X$ nonzero such that $Av = \lambda v$, where v is the associated **eigenfunction**. The **point spectrum** $\sigma_{pt}(A)$ is the set of all isolated eigenvalues of finite algebraic multiplicity. The **essential spectrum** is the complement of the point spectrum in the spectrum: $\sigma_{ess}(A) = \sigma(A) \setminus \sigma_{pt}(A)$.

If some value λ results in a **resolvent operator** $A - \lambda I$ with a non-trivial null space, as in (1), λ is an eigenvalue and is in the point spectrum. This is analogous to the condition for λ to be an eigenvalue in the finite-dimensional sense. If λ causes the resolvent operator to fail to have a bounded inverse by way of (2) or (3), then λ is in the essential spectrum. As a general rule, the essential spectrum corresponds to the constant end states to which the traveling wave is asymptotic, whereas the point spectrum corresponds to the component of the wave with spatial structure. There are a number of ways to identify essential and point spectra for various operators. We address several in the following sections.

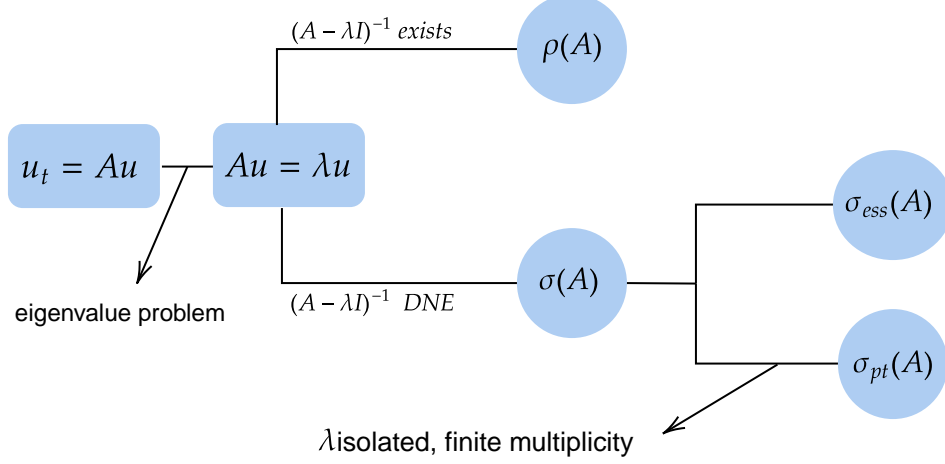


Figure 2.5: A graphical depiction of the elements of the resolvent set and the spectrum and a linear operator.

2.4 Finding the essential spectrum

The primary tool we will use to identify the location of the essential spectrum for second order systems is a classical result, not originally due to D. Henry but recorded as Theorem A.2 in the appendix to Chapter 5 in his lecture notes [21]. We paraphrase the result as follows, inspired by [24]:

Theorem 2.4.1. Suppose that $m(x), n(x)$ are bounded real functions and define $\lim_{x \rightarrow \pm\infty} m(x), n(x) = m^\pm, n^\pm$.

In any of the spaces $L^p(\mathbb{R}), 1 \leq p < \infty$, consider the closed, densely defined linear operator

$$Au = \partial_x^2 + m(x)\partial_x u + n(x)u \quad (2.20)$$

Define $S^\pm = \{\lambda | \lambda = -k^2 + ikm^\pm + n^\pm\}$, which are parabolas in the complex plane. Further define $P \subset \mathbb{C}$ such that $\mathbb{C} \setminus P$ is the component of $\mathbb{C} \setminus (S^+ \cup S^-)$ contained in the right half plane. Then, the essential spectrum of A is contained in P and includes $S^+ \cup S^-$.

Proof. For the proof and other supporting materials, see [21]. □

This gives us the following technique for finding the essential spectrum of A , a closed, densely defined, linear operator:

1. Find $A^{\pm\infty}$, which amounts to linearizing the relevant PDE about the wave solution we're interested in and evaluating as $x \rightarrow \pm\infty$.

2. Construct $S^{\pm\infty}$ by calculating the spectrum of $A^{\pm\infty}$, which should be in the algebraic form indicated in Theorem 2.4.1.
3. Conclude that the essential spectrum of A is bounded by the curves S^+ and S^- .

2.5 Finding the point spectrum: Sturm-Liouville theory

Determining the stability of a coherent structure such as a traveling wave does not necessarily require finding exact eigenvalues—instead, it suffices to determine the sign of the real part of the eigenvalue. In the case of a self-adjoint linear operator, we have $\lambda \in \mathbb{R}$ and are therefore concerned with whether there exist $\lambda > 0$, implying instability, or if all $\lambda \leq 0$, implying stability. In the case of an operator A resulting from linearizing a PDE about a solution such as a traveling wave, these λ are in $\sigma_{pt}(A)$. Note that the process of linearizing a PDE in two variables about a stationary solution reduces it to an ODE in a single variable. In the case that the PDE is in three or more variables, the resulting linear problem may or may not be separable. If it is separable, we can use Sturm-Liouville theory to analyze the properties of solution sets of the resulting boundary value problems.

2.5.1 A brief recap of Sturm-Liouville theory

The following linear, second-order ODE defined on the interval $[a, b]$ constitutes the **Sturm-Liouville problem**:

$$\frac{d}{dx} \left[p(x) \frac{du}{dx} \right] + q(x)u = -\lambda w(x)u \quad (2.21)$$

A Sturm-Liouville problem is said to be **regular** if:

- 1) $q, w \in C^0$ and $p \in C^1$ on $[a, b]$
- 2) $p, w > 0 \forall x \in [a, b]$
- 3) There are separated boundary conditions of Dirichlet, Neumann or Robin type at

$$x = a \text{ and } x = b$$

In first-order form, the problem is:

$$\begin{aligned} u' &= \frac{1}{p(x)} v \\ v' &= -(\lambda w(x) + q(x)) u \end{aligned} \quad (2.23)$$

The primary result of Sturm-Liouville theory are the **Sturm-Liouville theorems**, summarized as:

Theorem 2.5.1. *The eigenvalues λ_n of a regular Sturm-Liouville problem are real, bounded from below and can be ordered such that $\lambda_0 < \lambda_1 < \dots < \lambda_n < \dots \rightarrow \infty$. The eigenfunction u_n corresponding to λ_n has exactly n zeros on the interval $[a, b]$. Moreover, the (normalized) eigenfunctions are orthogonal and form an orthonormal basis under the inner product with weight w in the appropriate Hilbert space, meaning*

$$\langle u_n, u_m \rangle = \int_a^b u_n(x) u_m(x) w(x) dx = \delta_{nm}.$$

Proof. See [25] or any number of other resources. □

To identify the eigenvalues λ_n , we turn to oscillation theory.

2.5.2 Oscillation theory

We convert (2.21) to **Prüfer variables** by making the change of variables

$$u(x) = r(x) \sin \theta(x), \quad v(x) = r(x) \cos \theta(x) \quad (2.24)$$

Some authors refer to Prüfer variables as “polar coordinates in phase space,” an apt description as they allow us to translate the coordinate axes of our phase space from (u, u') to (r, θ) . Our Sturm-Liouville problem is now:

$$\begin{aligned} \theta' &= \left(-\lambda w(x) + q(x) \right) \sin^2 \theta(x) + \frac{1}{p(x)} \cos^2 \theta(x) \\ r' &= r \left(\frac{1}{p(x)} + \lambda w(x) + q(x) \right) \cos \theta(x) \sin \theta(x) \end{aligned} \quad (2.25)$$

It is evident from (2.25) that, since the equation for θ does not depend on r , we have reduced our system of two equations to a system of one equation (albeit a nonlinear equation). This change of coordinates requires $p(x) \neq 0$, but this is the same as only considering non-trivial solutions. The angle associated to (2.24) is clearly $\theta(x) = \arctan \left(\frac{u(x)}{v(x)} \right)$ but, to reflect that fact that it is an argument of two functions, the **Prüfer angle** is often defined as:

$$\theta(x) = \text{atan2}(u(x), v(x)) \mod 2\pi \quad (2.26)$$

where **atan2** is the two-argument arctangent:

$$\text{atan2}(x, y) = \begin{cases} \arccos \frac{x}{\sqrt{x^2+y^2}}, & y \geq 0 \\ -\arccos \frac{x}{\sqrt{x^2+y^2}}, & y < 0 \end{cases} \quad (2.27)$$

It is useful to “unwrap” the arctangent so that the angle (2.26) is not discontinuous and instead takes on all real values.

The Prüfer angle has a number of useful properties, chiefly that we can use the value of $\theta(x) \bmod \pi$ to count the number of zeros of the eigenfunction u , which Theorem 2.5.1 tell us is directly related to the indexing of the corresponding eigenvalue. To see why, note that $u(x_0) = 0 \iff \theta(x_0) = 0 \bmod \pi$, lest we have $r = 0$ and trivial solutions. But $\theta(x_0) = 0 \implies \theta'(x_0) = \frac{1}{p(x)} > 0$, so the angle is always increasing at a zero of u . The conclusion is that the Prüfer angle jumps by a multiple of π whenever u has a zero, and it does so in an increasing fashion. Therefore, the value of $\theta \bmod \pi$ is directly related to the number of zeros of u and we can identify whether there is an eigenvalue of the operator associated to (2.21) in an interval (λ_0, λ_1) by identifying if $\theta(x, \lambda)$ jumps by a factor of π as we vary λ .

2.5.3 An example

Consider the following reaction-diffusion equation:

$$u_t = u_{xx} + f(u) \quad (2.28)$$

for $x \in [0, L] \subset \mathbb{R}$ with Dirichlet boundary conditions and initial condition $u_0(x)$. We are interested in the stability of stationary solutions $\tilde{u}(x)$, defined by the condition $u_t = 0$. The stability question asks whether or not solutions that result from initial conditions close to $u_0(x)$ will decay to the stationary solution $\tilde{u}(x)$ or a translate.

To answer this question, we linearize (2.28) about $\tilde{u}(x)$ to obtain

$$\mathcal{L} = \frac{d^2}{dx^2} + f'(\tilde{u}(x)) \quad (2.29)$$

where $f'(\tilde{u}(x))$ is the derivative of f acting on the stationary solution. When seen as part of the operator \mathcal{L} , it is interpreted as a multiplication operator. We define $\sigma(\mathcal{L})$, the spectrum of \mathcal{L} , using the same definition as in

§2.3.2. Therefore, an element $\lambda \in \sigma(\mathcal{L})$ is an eigenvalue if there exists a non-trivial solution q to

$$(\mathcal{L} - \lambda I)q = 0 \quad (2.30)$$

We can rewrite the eigenvalue problem in terms of first order ODEs, obtaining

$$\begin{aligned} \dot{q} &= p \\ \dot{p} &= (\lambda - f'(\tilde{u}(x)) q) \end{aligned} \quad (2.31)$$

where $\cdot = \frac{d}{dx}$. The spectral parameter λ is an eigenvalue if it corresponds to a non-trivial solution of (2.31) while also satisfying the boundary conditions $q(0) = q(L) = 0$. To apply the theory described above to this example, we first convert (2.31) to polar coordinates, obtaining

$$\begin{aligned} \dot{r} &= r \cos \theta \sin \theta (1 + \lambda - f'(\tilde{u}(x))) \\ \dot{\theta} &= (\lambda - f'(\tilde{u}(x)) \cos^2 \theta - \sin^2 \theta) \end{aligned} \quad (2.32)$$

Noting that the equation for θ is independent of that for r , we may consider only the equation for θ , as any non-trivial value of $r(x)$ will solve (2.32). The eigenvalue problem then amounts to finding solutions $\theta(\lambda, x)$ such that the boundary conditions are satisfied, meaning $\theta(\lambda, 0) = \theta(\lambda, L) = 0 \pm n\pi$ for some λ . We can define the **accumulated angle** as $\Delta(\theta) = \theta(\lambda, L)$. This quantity amounts to the rotational value “accumulated” over the course of solution trajectories to the second equation in (2.32), where we are using the fact that we may assume that some solution $\theta(\lambda, x)$ satisfies the left-hand boundary condition (at $x = 0$) without assuming that λ is an eigenvalue, which would require it to also satisfy the right-hand eigenvalue (at $x = L$).

The upshot is that, for (2.31), we have the following eigenvalue condition:

$$\Delta(\theta(\lambda)) = 0 \pm n\pi \text{ for } n \in \mathbb{Z} \quad (2.33)$$

If λ satisfies (2.33), then it is an eigenvalue of \mathcal{L} as defined in (2.29).

2.6 Finding the point spectrum: the Evans function

The approach outlined above is not always sufficient for locating the spectrum, such as when the nonlinearity is particularly complex or the dimension of the system is high enough. The vague nature of this statement reflects the fact that PDE stability is a complicated problem without a one-size-fits-all solution.

Discussing all possible approaches is beyond the scope of this thesis but, for a comprehensive treatment, see some combination of [22], [24], [26] and others.

One tool useful for determining the stability of nonlinear waves is the **Evans function**. In brief, the Evans function is the Wronskian of decaying solutions to the eigenvalue problem $\lambda v = \mathcal{L}v$ arising from an evolution equation. The usefulness of the Evans function lies in the fact that its roots are precisely the eigenvalues of \mathcal{L} .

2.6.1 Constructing the Evans function

In what follows we give a very brief overview of the construction of the Evans function. For a more detailed treatment see [23] and, for the original work on the Evans function, see [27].

Consider the evolution equation $u_t = F(u)$. Traveling wave solutions \hat{u} moving with speed c are stationary solutions in the moving frame $x \rightarrow x - ct$, meaning that they are stationary solutions of the translated equation

$$u_t = cu_x + F(u) \quad (2.34)$$

The eigenvalue problem resulting from linearizing the flow defined by (2.34) about solutions \hat{u} is

$$\lambda v = (c \frac{d}{dx} + DF(\hat{u}))v \equiv \mathcal{L}v, \quad \mathcal{L} : X \rightarrow X \quad (2.35)$$

where \mathcal{L} is a densely defined linear operator on a Banach space X . Consider the corresponding first order system

$$\frac{dW}{dx} = A(x; \lambda)W \quad (2.36)$$

where

$$A = \frac{1}{c}(\lambda - \mathcal{L}) \quad (2.37)$$

for $W \in \mathbb{C}^n$. Finding an eigenvalue λ of \mathcal{L} amounts to finding a non-trivial solution of (2.36) that satisfies the decaying boundary conditions at infinity $W(x \rightarrow \pm\infty) = 0$. Because \hat{u} is a traveling wave it converges exponentially to constant end states $u_{\pm\infty}$ as $x \rightarrow \pm\infty$. Therefore, the matrices A must also converge exponentially to the constant matrices

$$A_{\pm\infty}(\lambda) = \lim_{x \rightarrow \pm\infty} A(x; \lambda) \quad (2.38)$$

If A satisfies a handful of assumptions (see [23] for details) we can say that a non-trivial bounded solution W of (2.36) exists if and only if the unstable manifold $\mathcal{W}_-^u(x; \lambda)$ at $x = -\infty$ intersects the stable manifold

$\mathcal{W}_+(x; \lambda)$ at $x = +\infty$ non-trivially. Given matrices W_- and W_+ whose columns are analytic bases of \mathcal{W}_- and \mathcal{W}_+ respectively, the Evans function is defined as

$$E(\lambda) = \det([W_-(x; \lambda), W_+(x; \lambda)]) \quad (2.39)$$

The roots of $E(\lambda)$ have exactly the same location and multiplicity as the eigenvalues of \mathcal{L} . The function $E(\lambda)$ is analytic on the closed, deleted right half of the complex plane, where the point at the origin is excluded because the translational invariance of traveling waves means there will always be an eigenvalue at $\lambda = 0$. We can evaluate $E(\lambda)$ on contours in this set and find the roots contained within these contours, which amounts to finding the eigenvalues of \mathcal{L} . If any of these roots are contained in the right half-plane, we may conclude spectral instability of the traveling wave \hat{u} .

2.7 Mechanisms of instability

Finally, we note two means by which a system such as (2.18) may exhibit instabilities. In some systems, instabilities emerge as a result of nonlinearities inherent in the problem. In this case, we might consider the algebraic representation of the spectrum, obtained by a Fourier transform or a separation of variables ansatz, and consider the effect on the location of the spectrum of varying the spatial wavenumbers. If varying a wave number k_i associated to the spatial direction x_i causes an element of the spectrum to cross from the left-half plane in to the right-half plane, we say that the corresponding solution is unstable with respect to perturbations in the x_i direction. On the other hand, an external forcing may upset the equilibrium of a steady-state solution: varying the parameter associated with this forcing then causes a bifurcation in the system's behavior. In Chapters 4 and 5 we discuss instabilities generated through this second mechanism and, in Chapter 6, we consider an example of the former mechanism.

CHAPTER 3

A model of fire front propagation

Reaction-diffusion models of fire propagation have been studied since at least the 1980s (see [28]–[34]) as a minimal model capable of capturing key components of the transport problem underlying fire spread. Such models rely on a number of simplifying assumptions to render them analytically tractable: exactly which concessions are made varies between studies. One of the draws of reaction-diffusion models is that they admit traveling wave solutions that may be understood as combustion fronts. Moreover, when a nonlinear reaction term is employed, they are capable of reproducing complex behavior and spatial and temporal pattern formation that is not captured by empirical models.

Early investigations of existence and stability of combustion front solutions in such systems generally focused on the effect of varying the Lewis number in systems insulated from heat loss, as in [32] and [35]. The Lewis number, denoted Le , is a non-dimensional quantity defined as the ratio of thermal diffusivity to mass diffusivity. In reaction-diffusion models of fire propagation, its inverse is generally the coefficient of the fuel diffusion term. $\text{Le} \rightarrow \infty$ regimes, in which the effect of fuel diffusion is neglected in the large parameter limit, are generally associated with solid fuels that do not diffuse. Gaseous fuels, on the other hand, are associated with $\text{Le} \rightarrow 1$ regimes. [30] calculates flame speeds (corresponding to traveling wave speeds) for pre-mixed gaseous and solid fuels in a one-dimensional system for both Le regimes using asymptotic and phase plane methods: they find their results to be in good agreement with numerics and identified a period-doubling route to chaos in the infinite Le regime.

The system in [30] is insulated from heat loss to the environment. The authors in [32] look at a similar system with heat loss in two dimensions, finding that increasing the effect of heat loss also results in chaotic behavior, and [33] presents numerical results for a similar system. In [35], the authors take a geometric approach to a one-dimensional system with high (but not infinite) Lewis number, using techniques from geometric singular perturbation theory to demonstrate the existence of combustion fronts and explore the nonlinear stability of fronts in the high Le system in comparison to the infinite Le system.

Common to all of these studies is the use of an Arrhenius-type, temperature-dependent reaction law, often

normalized so that there is no reaction at ambient temperature. [34] uses a smooth form of this reaction term in a system with solid fuel and the addition of an advection term. Their work discusses the stability implications of a quasi-cubic reaction term and computes traveling wave profiles, but stops short of an in-depth stability analysis of these profiles. More recent works have explored the effects of curvature and oxygen consumption [36] and pyrogenic flow [37] in slightly more complex versions of the prototypical reaction-diffusion (RD) or reaction-diffusion-advection (RDA) systems.

To our knowledge, no authors have taken a geometric approach to studying the stability of traveling fronts in an RDA system with a spatially dependent advection term. Recent work due to [38] and [39] has explored the effect of diffusion and advection regimes on planar interfaces in a singularly perturbed system similar to the one studied in the following chapters. The advection term they considered does not, however, have spatial dependence and their model is not adapted to reflect the physics of fire propagation.

In this chapter, we discuss the derivation of a model for temperature and fuel concentration from conservation laws. The model captures the effects of radiative heat transfer, loss of heat to the atmosphere, a combustion reaction coupled to the temperature, and a spatially dependent advection term describing the local wind velocity. We omit diffusion of the fuel and are therefore considering an infinite Le regime (in other words, a solid fuel source). We discuss the existence of traveling wave solutions, the geometric and multi-scale features of the system, and the stability problem. Finally, we examine the simple example of a one-dimensional front impacted by a constant wind using tools from Chapter 2. The groundwork laid in this chapter allows us to explore more complex cases in Chapters 4 and 5.

3.1 The model

We will derive the following model, modified from [33] and [34]¹ for the evolution of the temperature $T(x,t)$ and the mass fraction of fuel $S(x,t)$ of a fixed, two-dimensional region of homogeneous solid fuel,

$$\begin{aligned}\frac{\partial T}{\partial t} &= k\nabla^2 T - \vec{v} \cdot \nabla T + A(SR(T) - C(T - T_a)) \\ \frac{\partial S}{\partial t} &= -C_s SR(T)\end{aligned}\tag{3.1}$$

with initial conditions $T(\vec{x},t=0) = T_0$, $S(\vec{x},t=0) = S_0$. The mass fraction of fuel is defined as $S = \frac{F(\vec{x},t)}{F_0}$, where F is the quantity of fuel at (\vec{x},t) and F_0 is the initial quantity of fuel. The Arrhenius reaction term is a smooth function R based on the Arrhenius reaction rate:

$$R(T) = \begin{cases} \exp(-B/(T - T_0)) & T > T_0 \\ 0 & T \leq T_0 \end{cases}\tag{3.2}$$

Before the reaction process begins, there is a full fuel load and $S = 1$. As the reaction proceeds, the fuel rapidly depletes before settling to a constant value.

The dimensional parameters included in equations (3.1) and (3.2) and their units are:

$k(m^2/s)$ the thermal diffusivity

$A(K/s)$ the temperature increase per second at the maximum burning rate with $S_0 = 1$ and no cooling

$B(K)$ the proportionality coefficient in the Arrhenius reaction rate

$C(1/K)$ the scaled coefficient of heat transfer to the environment

$T_a(K)$ the ambient temperature

$\vec{v}(m/s)$ the wind speed

¹The model in [34] does not assume a constant diffusion coefficient and the model in [33] does not allow for a continuous reaction term, among other differences.

3.2 Derivation of the model from conservation laws

We develop two PDEs for energy balance and fuel reaction rate that govern the behavior of the state variables: fraction of the fuel supply remaining S and temperature of the fire layer T . These equations describe conditions in a two-dimensional “fire layer,” defined by [34] as the layer of fuel through which the fire moves and the thin layer of atmosphere directly above it.

We define the concentration of fuel remaining at a given time, $F(t)$, to be some positive quantity with units of $\frac{\text{kg}}{\text{m}^2}$. Clearly the fire depletes its fuel source as it burns, so we need to define an initial fuel concentration, F_0 . Then, the mass fraction of fuel is the fraction of the fuel remaining after time t :

$$S = \frac{F(t)}{F_0} \quad (3.3)$$

We define our combustion rate to be $C_s R(T)$, where $R(T)$ is a function of temperature only and C_s is a proportionality constant with units of $1/\text{s}$. Assuming that the rate of fuel disappearance is proportional to the rate of reaction multiplied by the amount of available fuel, we have:

$$\frac{\partial S}{\partial t} = \frac{1}{F_0} \frac{\partial F}{\partial t} = -\frac{F}{F_0} C_s R(T) = -SC_s R(T) \quad (3.4)$$

giving us the PDE for our first state variable.

For the temperature equation, we employ a conservation of energy approach. Given an arbitrary control area A (we can think of this as a fixed infinitesimal region of the fire layer), the rate of heat energy accumulation in A must be a sum of the rate of heat energy transferred to A by convection, conduction, heat generation within A , and work done by the system on its surroundings and/or by the surroundings on the system. In this case, no work is done on the system or by the system on the boundary. The remaining terms have obvious physical meanings: convection occurs due to the movement of air through the fire layer, conduction occurs as a result of the conductive heat flux, heat generation occurs due to combustion, and heat loss occurs due to the difference in temperature between the fire layer and the surrounding air.

The rate of heat energy accumulation in A is

$$\frac{\partial}{\partial t} \left(\iint_A \tau dA \right) \quad (3.5)$$

where τ is heat energy per unit area and has units of J/m^2 . We take $\tau = \rho c_p T$, where c_p is the specific heat

of the fire layer with units J/kgK and ρ is the surface density of the fire layer in kg/m^2 . The units of the quantity $\tau = \rho c_p T$ are then J/m^2 , as desired.

The heat generation and heat loss terms are straightforward: we take the volume integral of the as-of-yet undefined expressions q_g and q_c , where q_c is taken to be positive and so must be subtracted off. Then, we calculate the component of the conductive heat flux, \vec{q}_r , normal to the boundary B of our control volume V as $\mathbf{n} \cdot \vec{q}_r$. This gives us a quantity with units of J/ms . Multiplying through by a differential line element dB gives us the rate of heat flow over that small one-dimensional region, a quantity with units of J/s . Finally, we integrate over the boundary of the control area to obtain the total rate of heat flow through the boundary due to the conductive heat flux,

$$\int_B \mathbf{n} \cdot \vec{q}_r dB \quad (3.6)$$

Similarly, we calculate the component of the wind velocity \mathbf{v} normal to the boundary as $\mathbf{n} \cdot \mathbf{v}$. Then, $\mathbf{n} \cdot \mathbf{v} dB$ gives the rate at which wind blows through a portion of the boundary. To convert this to a measure of energy, we multiply by the heat energy per area, $\rho c_p T$, and then integrate over the entire region to arrive at

$$\int_B \rho c_p T (\mathbf{n} \cdot \mathbf{v}) dB \quad (3.7)$$

Combining all of the components of our conservation of energy law, we have

$$\frac{\partial}{\partial t} \left(\iint_A \rho c_p T dA \right) = \int_B \mathbf{n} \cdot \vec{q}_r dB + \int_B \rho c_p T (\mathbf{n} \cdot \mathbf{v}) dB + \iint_A q_g - q_c dA \quad (3.8)$$

The divergence theorem allows us to transform the line integral of a vector field into the surface integral of the divergence of that vector field, given that the boundary enclosing the surface is closed. Assuming a non-porous boundary for our control area, we have:

$$\iint_A \frac{\partial(\rho c_p T)}{\partial t} dA = \iint_A \nabla \cdot \vec{q}_r dA + \iint_A \nabla \cdot (\rho c_p T \mathbf{v}) dA + \iint_A q_g dA - \iint_A q_c dA \quad (3.9)$$

We are able to bring the derivative inside the integral on the left hand side of the equality because A is a fixed area that does not change in time. Combining terms,

$$\iint_A \left(\frac{\partial(\rho c_p T)}{\partial t} - \nabla \cdot \vec{q}_r - \nabla \cdot (\rho c_p T \mathbf{v}) - q_g + q_c \right) dA = 0 \quad (3.10)$$

Because A is an arbitrary area, the above integral must go to zero regardless of our region of integration. As a result, the only way for equation (3) to hold is if the integrand is identically zero.

$$\frac{\partial(\rho c_p T)}{\partial t} - \nabla \cdot \vec{q}_r - \nabla \cdot (\rho c_p T \mathbf{v}) - q_g + q_c = 0$$

Noting the product rules $\frac{\partial(\rho c_p T)}{\partial t} = \rho c_p \frac{\partial T}{\partial t} + T \frac{\partial \rho c_p}{\partial t}$ and $\nabla \cdot (\rho c_p T \mathbf{v}) = T \nabla \cdot \rho c_p \mathbf{v} + \rho c_p \mathbf{v} \cdot \nabla T$, we have:

$$T \left(\frac{\partial \rho c_p}{\partial t} + \nabla \cdot \rho c_p \mathbf{v} \right) + \rho c_p \left(\frac{\partial T}{\partial t} + \mathbf{v} \cdot \nabla T \right) - \nabla \cdot \vec{q}_r - q_g + q_c = 0 \quad (3.11)$$

The first term in equation (5) contains the continuity equation for a conserved quantity (mass) and therefore goes to zero. We are left with

$$\frac{\partial T}{\partial t} = -\mathbf{v} \cdot \nabla T + \frac{1}{\rho c_p} (\nabla \cdot \vec{q}_r + q_g - q_c) \quad (3.12)$$

This can be written in material derivative form as

$$\rho c_p \frac{DT}{Dt} = \nabla \cdot \vec{q}_r + q_g - q_c \quad (3.13)$$

which is analogous to equation (10) in [34], modified for consistency in the dimensions.

We approximate heat generation as a function of the fuel lost, represented as the remaining fuel fraction F , the reaction rate $C_{sr}(T)$, and a coefficient A_1 with units $\frac{J}{kg}$ representing the heat energy released per unit mass of fuel burned. The resulting expression for q_g has units of $\frac{W}{m^2}$.

$$q_g = A_1 F C_{sr}(T) \quad (3.14)$$

We approximate heat lost to the atmosphere through convection using Newton's law of cooling, where T_a is the ambient temperature of the atmosphere and C_a is the heat transfer coefficient, with units $\frac{W}{Km^2}$. The resulting expression for q_c has units of $\frac{W}{m^2}$.

$$q_c = C_a (T - T_a) \quad (3.15)$$

Finally, we use Fourier's law of heat conduction to write the heat flux through a two-dimensional unit segment

of the fire layer as

$$\vec{q}_r = -k_1 \nabla T \quad (3.16)$$

Where k_1 , the thermal conductivity of the fire layer, has units $\frac{W}{K}$ and the resulting expression for \vec{q}_r has units $\frac{W}{m}$.

Putting everything together, we arrive at our final temperature PDE

$$\frac{\partial T}{\partial t} = -\mathbf{v} \cdot \nabla T + \nabla \cdot (k \nabla T) + A(SR(T) - C(T - T_a)) \quad (3.17)$$

where $k = \frac{k_1}{\rho c_p}$, $A = \frac{A_1 C_s}{\rho c_p}$ and $C = \frac{C_a}{A_1}$. Equations (3.4) and (3.17), together with initial conditions

$$S(t_0) = 1 \text{ and } T(t_0) = T_0 \quad (3.18)$$

compose our model of fire propagation in the fire layer.

3.3 The nondimensional model and separation of time scales

We nondimensionalize and transform our dependent variables from (T, S) to (u, v) . Our system becomes

$$\begin{aligned} u_t &= \nabla^2 u - \vec{w} \nabla \cdot u + vr(u) - lu \\ v_t &= -\beta vr(u) \end{aligned} \quad (3.19)$$

with nondimensional parameters $l = BC$, $\beta = \frac{BC_s}{A}$, and $\vec{w} = \vec{v} \sqrt{\frac{B}{Ak}}$. The Arrhenius reaction term becomes

$$r(u) = \begin{cases} e^{-1/u} & u > 0 \\ 0 & u \leq 0 \end{cases} \quad (3.20)$$

The qualitative characteristics of solutions to (3.19) now depend solely on the nondimensional parameters l, β and \vec{w} . The convection term $-lu$ is a nondimensional form of Newton's law of cooling, with l serving as the heat transfer coefficient. We fix l at an appropriate value— see §3.9 for a discussion of our choice. β is inversely proportional to the heat of the combustion reaction. “Heat of reaction” is a term borrowed from physical chemistry for “change in enthalpy,” where enthalpy refers to the total heat content of the system.

The process of combustion causes a large, rapid change in the total heat content of the system, so we expect $\beta \ll 1$. The resulting existence of a small parameter influencing only the dynamics described by the

second equation in (3.19) indicates that the process of fuel consumption is occurring on a much slower time scale than the temperature increase.

3.4 Assumptions on the wind term

The nondimensional wind takes the form of a vector

$$\vec{w} = \begin{pmatrix} w_x \\ w_y \end{pmatrix} \quad (3.21)$$

We make several critical assumptions:

1. The x component of the wind depends only on the x coordinate and time, so that $w_x = w_x(x, t)$.
2. The x component of the wind term is chosen to model a fire-induced wind, described in detail in Chapter 4. As a result, the wind should be defined in the frame of reference of the moving fire front. In the moving frame $z \rightarrow x - ct$ described below, w_z is a function of z only. Therefore, w_x in the stationary frame must be a function of $x - ct$.
3. The y component of the wind depends only on the y coordinate, so that $w_y = w_y(y)$.

3.5 Traveling wave solutions to the full system

The system (3.19) admits traveling wave solutions corresponding to a heteroclinic orbit as described in Chapter 2. To center ourselves in the frame of reference of a wave traveling with speed c , we make the change of variables $x \rightarrow z = x - ct$. In this frame, our equations are

$$\begin{aligned} u_t &= (c - w_z)u_z - w_yu_y + u_{zz} + u_{yy} + f(u, v) \\ v_t &= cv_z - \beta vr(u) \end{aligned} \quad (3.22)$$

where we have split the wind term in to its spatial components, and written the full reaction term as

$$f(u, v) = vr(u) - lu = v \exp(-1/u) - lu \quad (3.23)$$

Going forward, when we refer to the “reaction term,” we will be referring to the function $f(u, v)$. Finding a traveling wave solution of (3.19) is equivalent to finding a stationary solution of (3.22) that is spatially

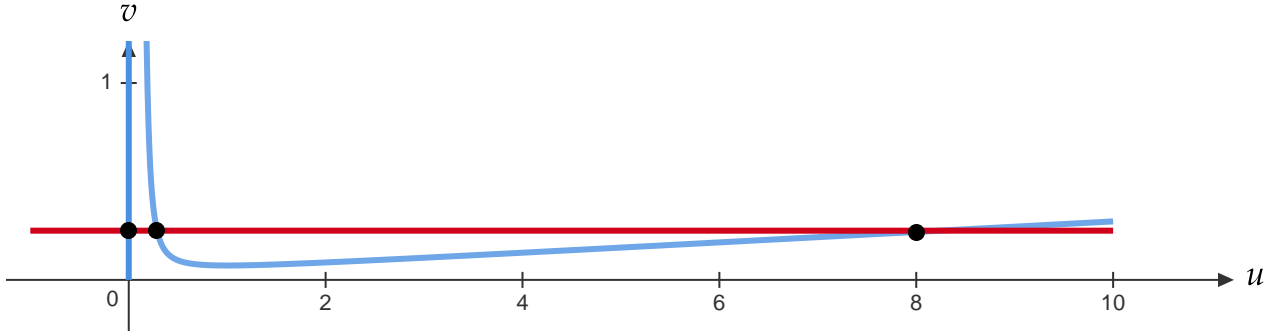


Figure 3.1: The nullclines of the first order system, excluding the s axis. The line $v = 0.25$ is indicated in red and the resulting (u,v) fixed points are indicated by black dots. All fixed points live in the $s = 0$ plane.

uniform in the y direction. In other words, we seek solutions (\hat{u}, \hat{v}) to

$$\begin{aligned} 0 &= (c - w_z)u_z + u_{zz} + f(u, v) \\ 0 &= cv_z - \beta vr(u) \end{aligned} \tag{3.24}$$

In first order form, this is

$$\begin{aligned} u' &= s \\ s' &= -(c - w_z)s - f(u, v) \\ v' &= \frac{\beta}{c}vr(u) \end{aligned} \tag{3.25}$$

where $' = \frac{d}{dz}$. Traveling wave solutions asymptotically connect fixed points of (3.25) as described in Chapter 2. These fixed points exist on the nullclines of (3.25), given by the curve

$$v(u) = \begin{cases} lu \exp\left(\frac{1}{u}\right) & u \neq 0 \\ 0 & u = 0 \end{cases} \tag{3.26}$$

Intersections of the line $v = v^*$ with (3.26) give $(u(v^*), v^*)$ pairs of fixed points, as in figure 3.1. All fixed points live in the $s = 0$ plane. The value of v is, of course, not constant. However, in line with the analysis in §3.3, we can treat it as such for major sections of the heteroclinic orbit that corresponds to profile solutions.

3.6 The singular problem

In the presence of the small parameter β , (3.25) is a singularly perturbed system of equations. We approach the problem using **geometric singular perturbation theory** as opposed to traditional asymptotic methods. This geometric framework is elegant and in line with the methods used throughout this dissertation. Following the structure outlined in [40], we reframe (3.25) as the *fast system*:

$$\begin{aligned} U_z &= g(U, v, \beta) \\ v_z &= \beta h(U, v, \beta) \end{aligned} \tag{3.27}$$

where $U = (u, s)$. Rescaling $\zeta = \beta z$, we obtain the corresponding *slow system*:

$$\begin{aligned} \beta U_\zeta &= g(U, v, \beta) \\ v_\zeta &= h(U, v, \beta) \end{aligned} \tag{3.28}$$

When β is nonzero, the fast and slow systems are equivalent. Taking the limit as $\beta \rightarrow 0$ in (3.27) and (3.28), we obtain the *fast and slow limit systems*:

$$\begin{array}{ll} \text{Fast limit system:} & U_z = g(U, v, 0) \\ & v_z = 0 \\ \text{Slow limit system:} & 0 = g(U, v, 0) \\ & v_\zeta = h(U, v, 0) \end{array} \tag{3.29}$$

In the fast system, there exists a single heteroclinic orbit connecting the system's fixed points. To understand this orbit in the β nonzero system, we first need to understand its component pieces in the singular system. This “singular orbit” is composed of a heteroclinic connecting the fixed point at $(u_0, 0, v_0)$ with a fixed point of the fast limit system at $(u_2, 0, v_0)$, another heteroclinic connecting the fixed point of the fast limit system at $(u_2, 0, v_f)$ with the fixed point at $(u_0, 0, v_f)$, and a “critical manifold” connecting the two heteroclinics. The flow of the slow limit system occurs on this critical manifold, which lives on the set of fixed points of the fast limit system corresponding to fixed values of v . Note that every $v = v^*$ plane is invariant. The orbital decomposition is illustrated in figure 3.2. For a rigorous treatment of this decomposition, see [40]. In Chapters 4 and 5 we will focus on the fast limit system, which we will refer to as the *reduced system*.

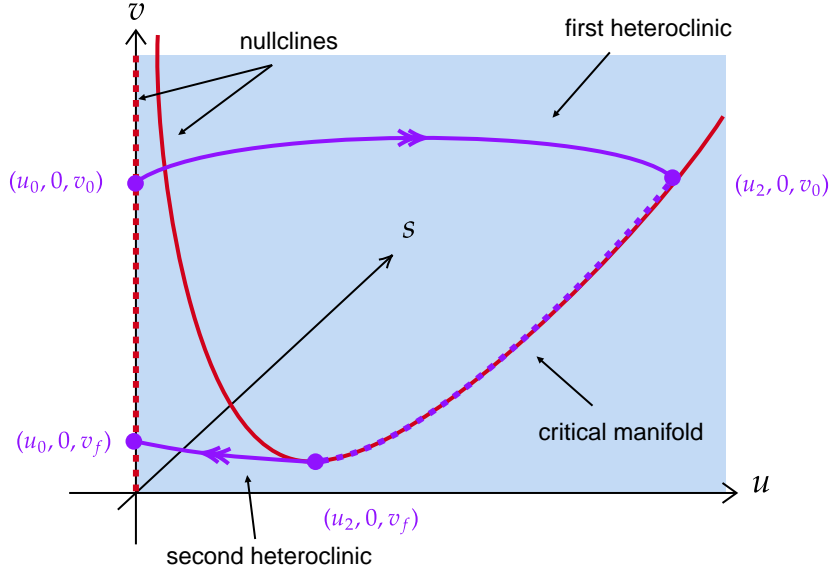


Figure 3.2: The singular orbit. In this depiction, the jump occurs at the knee of the nullcline. For other values of v_f , the jump occurs before the knee.

Fixed points of the full system consist of coordinate triples $(u, s = 0, v)$. The u coordinate of the fixed point corresponds to roots of the reaction term $f(u, v)$ for fixed v : see figure 3.3. The reaction term has three roots for values of v^* above some threshold value. We refer to these fixed points as u_0, u_1 and u_2 . Note that we will always have $u_0 = 0$ in the nondimensional system.

The v coordinate of the fixed point may be found by noting that the first and second heteroclinic orbits in the singular orbit described in §3.3 and indicated as solid lines in figure 3.2 must correspond to profile solutions moving with the same wave speed. By solving numerically for the wave speed (using the boundary value problem method outlined in §2.2) for a range of v values in $[0, 1]$, we may obtain a function $c(v)$, as illustrated in figure 3.4. We define several key points on the graph of $c(v)$:

1. \bar{v} , the value of v such that $c(v) = 0$ and the system is Hamiltonian. The graph of $f(u, v)$ is divided into two branches on either side of the vertical line $v = \bar{v}$.
2. v_{thresh} , the threshold value of v necessary for bistability: this corresponds to the minimum in u of the $v(u)$ nullcline in figure 3.1. This is also the fuel load value below which the reaction is no longer self-sustaining and the fixed points u_1 and u_2 come together. For $v < v_{\text{thresh}}$, no reaction occurs and the function is not defined.
3. c_{crit} , the c value corresponding to v_{thresh} on the left-hand branch of the graph

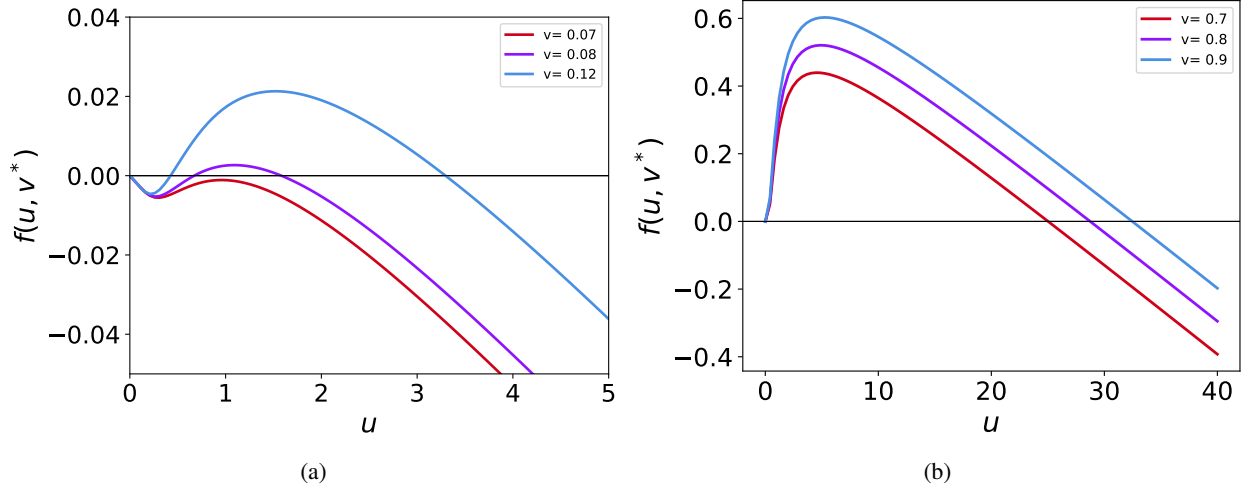


Figure 3.3: The reaction term for various values of v^* for (a) small v^* regimes and (b) large v^* regimes. The zeros of the reaction term are u_0, u_1 and u_2 . Note that, for $v^* \gg 0$, u_0 and u_1 are very close together relative to u_2 . Also note, in figure (a), that $v = 0.07$ is below the threshold for bistability.

4. v_{crit} , the v value corresponding to c_{crit} on the right-hand branch of the graph

Two qualitatively different scenarios are possible. For all $v_0 \geq v_{\text{crit}}$, the fuel will be consumed until reaching $v_f = v_{\text{thresh}}$, at which point the temperature will cool from u_2 back to u_0 . However, for $v_0 < v_{\text{crit}}$, the fuel will be consumed until reaching some $v_f > v_{\text{thresh}}$ determined by the graph of $c(v)$. Returning to figure 3.1, for most values of v_0 the “jump” back from the critical manifold to the fixed point at $(u_0, 0, v_f)$ occurs at the knee of the nullcline, as depicted. However, for a small subset of v values, this jump occurs for $v_f > v_{\text{thresh}}$.

The graph of $c(v)$ allows us to identify the v_f associated to some v_0 by pinpointing the wave speed value associated to both. Functionally, to identify the v value of the fixed point triple $(u, 0, v_f)$, one only needs to identify the initial condition v_0 , use the graph of $c(v)$ to find the c value associated to that v_0 , and draw a horizontal line across the graph to identify v_f .

3.7 Formulating the eigenvalue problem for the reduced system

In Chapters 4 and 5 we consider the dynamics of the fast limit (reduced) system. To understand our motivation, it is useful to consider what this means in the context of the pulse solutions in u to (3.25) when $\beta \neq 0$. The pulse consists of two pieces:

1. The **reaction zone**, in which the temperature quickly rises from ambient to maximum. This corresponds to the first heteroclinic in figure 3.2.

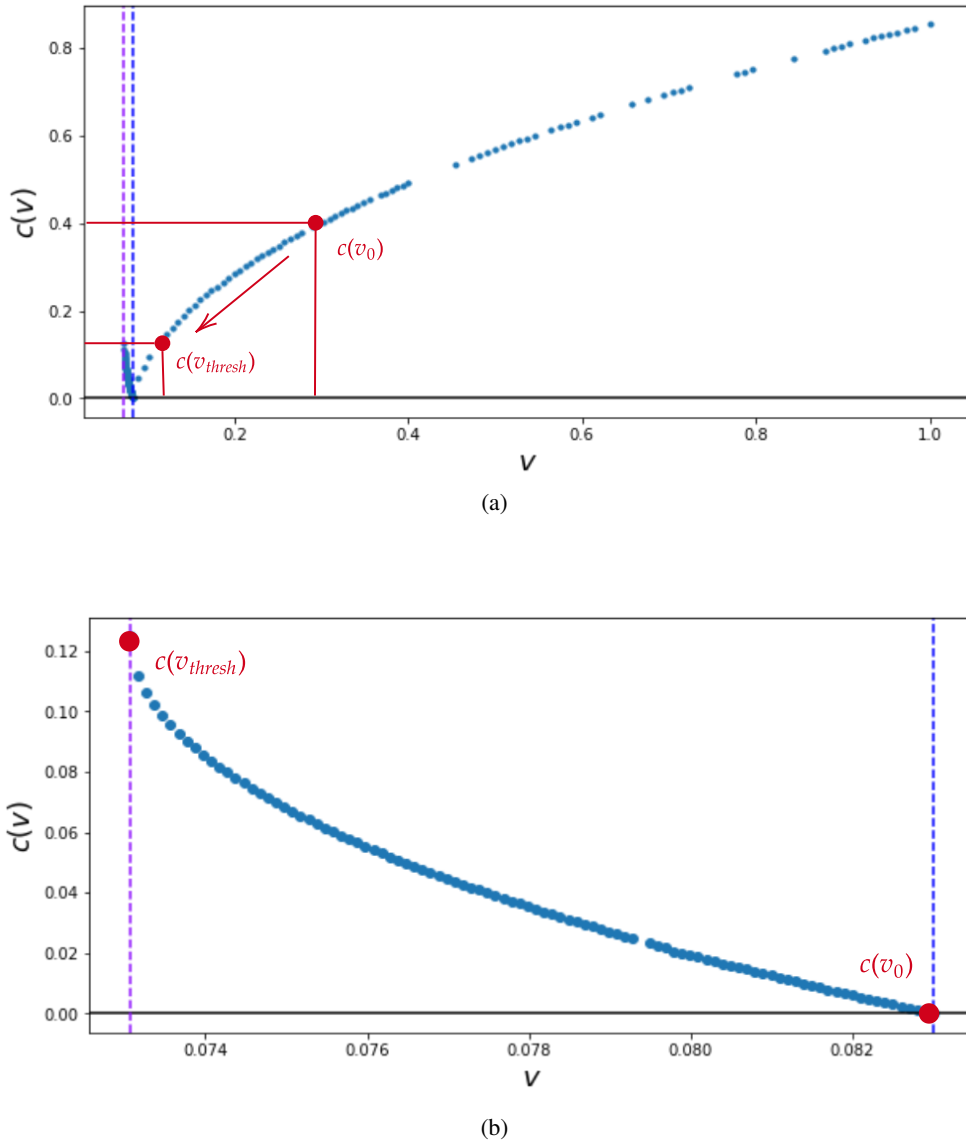


Figure 3.4: Wave speed c as a function of fuel load

2. The **cooling zone**, in which the temperature slowly cools back from maximum to ambient. This corresponds to the second heteroclinic in figure 3.2.

Considering only the fast limit system amounts to studying only the part of the pulse corresponding to the reaction zone. This segment of the pulse can be viewed as a traveling front either connecting regions of ambient to maximum temperature and moving with speed $c < 0$ or connecting regions of maximum to ambient temperature and moving with speed $c > 0$, as depicted in figure 3.5. The reduced (meaning the fast

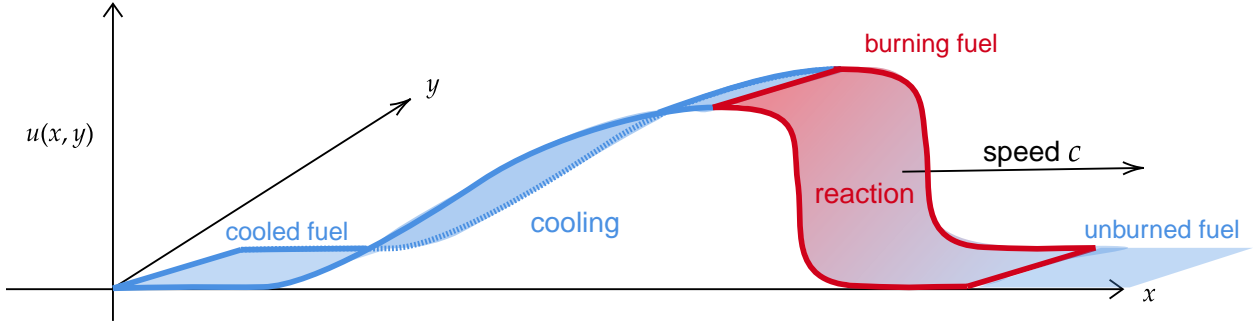


Figure 3.5: A schematic of the temperature pulse as a function of the spatial variable. Note the sharp, leading edge gradient in red followed by the gradual cooling on the tailing end, indicated in blue. In chapters 4 and 5, we focus on the traveling front consisting of the red ‘‘reaction’’ zone.

limit) system is found by taking $\beta \rightarrow 0$ in (3.27):

$$\frac{\partial u}{\partial t} = u_{zz} + u_{yy} + (c - w_z(z))u_z - w_y(y)u_y + f(u, v^*) \quad (3.30)$$

where v^* is a constant. Linearizing (3.30) about front solutions \hat{u} satisfying the reduced analogue of (3.24) we obtain, in linearized coordinates $u \rightarrow p$,

$$\frac{\partial p}{\partial t} = p_{zz} + p_{yy} + (c - w_z(z))p_z + w_y(y)p_y + f'(\hat{u})p \quad (3.31)$$

where

$$f'(u(z)) = \begin{cases} \frac{v^*}{u^2} \exp(-\frac{1}{u}) - l & u(z) > 0 \\ -l & u(z) = 0 \end{cases} \quad (3.32)$$

The corresponding eigenvalue equation is

$$\lambda p = \frac{\partial^2 p}{\partial z^2} + \frac{\partial^2 p}{\partial y^2} + (c - w_z(z))\frac{\partial p}{\partial z} + w_y(y)\frac{\partial p}{\partial y} + f'(\hat{u})p \quad (3.33)$$

We separate variables, taking $p(z, y) = q(z)\eta(y)$ and obtaining

$$\frac{d^2\eta}{dy^2} + w_y(y)\frac{d\eta}{dy} = \mu\eta \quad (3.34)$$

$$\frac{d^2q}{dz^2} + (c - w_z(z))\frac{dq}{dz} + f'(\hat{u})q = (\lambda - \mu)q = \omega q \quad (3.35)$$

where μ is the transverse eigenvalue and $\lambda - \mu = \omega$ is the streamwise eigenvalue.

We will refer to (3.33) as the “primary” eigenvalue problem that determines the stability of our two-dimensional front solution (the reaction zone depicted in figure 3.5). Equations (3.34)-(3.35) are then “secondary” eigenvalue problems related to transverse and streamwise stability, respectively. Eigenvalues of the two-dimensional problem are denoted λ with eigenfunctions $p(z, y) = q(z)\eta(y)$.

3.8 Stability of one-dimensional front solutions in the constant wind case

Consider (3.35), the eigenvalue problem in the x direction with eigenvalue ω . The ODE corresponding to (3.35), before linearization, is

$$(c - w_z) \frac{\partial u}{\partial z} + \frac{\partial^2 u}{\partial z^2} + f(u) = 0 \quad (3.36)$$

Equation (3.36) governs front solutions \hat{u} —solutions without dependence on t or y —to the original PDE (3.30). These fronts have the form of the sharp, leading edge gradient curve depicted in red in figure 3.5 and connect regions of zero temperature ($u = 0$) to regions of maximum temperature ($u = u_2$), where these values of u are found as zeros for the reaction term $f(u, v^*)$ for fixed v^* , as depicted in figure 3.1. It is a useful exercise to understand the stability of these solutions in the context of the two-dimensional PDE using the techniques described in Chapter 2 for the simple case when the wind \vec{w} is constant in space.

3.8.1 The essential spectrum

We begin by considering the eigenvalue problem (3.33) resulting from linearizing (3.30) about front solutions \hat{u} to (3.36). Theorem 2.4.1 tells us that the essential spectrum of the operator \mathcal{L} associated with (3.33) is bounded by $\mathcal{L}^{\pm\infty}$, determined by evaluating \mathcal{L} as $z \rightarrow \pm\infty$. Note that this is equivalent to linearizing about the constant solutions u_-, u_+ to which the traveling front \hat{u} is asymptotic. This results in

$$\mathcal{L}^{\pm\infty} p = \left(\frac{\partial^2}{\partial z^2} + \frac{\partial^2}{\partial y^2} + (c - w_z) \frac{\partial}{\partial z} - w_y \frac{\partial}{\partial y} + v^* r'(u_{\pm}) - l \right) p = \lambda p \quad (3.37)$$

Finding the spectrum of $\mathcal{L}^{\pm\infty}$ amounts to finding λ such that $\mathcal{L}^{\pm\infty} - \lambda I = 0$. Rather than solve this differential equation, we take the Fourier transform to convert our problem in to an algebraic one, resulting in

$$\lambda_{\pm} = -k^2 - n^2 + (c - w_z)ik - w_y in + v^* r'(u_{\pm}) - l \quad (3.38)$$

for $k, n \in \mathbb{R}$ wave numbers in the streamwise and transverse directions, respectively. The resulting curves for \mathcal{L}_- are depicted in figure 3.6 for a range of k and n . The curves are left-facing parabolas in the left half-plane

parameterized by the streamwise wave number k and plotted for several values of the transverse wave number n with parameter values $v^* = 1$, $w_y = 1$, $w_z = -0.05$, and $c = -0.085$. The curve for $n = 0$ comes close to the imaginary axis, but does not touch or cross it. The curves are very similar for \mathcal{L}_+ because, for small values of v^* , all three fixed points of the reaction term $f(u, v^*)$ are relatively close together. The depicted parabolas form the boundaries of the essential spectrum for the corresponding operator \mathcal{L} . The takeaway is that the end states of the front solution \hat{u} are not unstable with respect to transverse or streamwise perturbations in the context of the initial PDE (3.30).

3.8.2 The point spectrum

As discussed in Chapter 2, the point spectrum may be computed using Sturm-Louiville theory for the reduced system. However, in order to develop tools that may later be used in the full, $\beta \neq 0$ system, we compute the point spectrum by way of the Evans function. Recall that the Evans function is an analytic function, defined as the Wronskian of decaying solutions to the eigenvalue problem (3.37), whose zeros coincide exactly with the elements of the point spectrum. Using the package STABLAB [41] we compute the Evans function on a semi-annulus contour excluding the origin, where we expect an eigenvalue due to the translational symmetry of the problem. For a contour of any radius, we find that the winding number—defined as the number of zeros of the Evans function enclosed by the contour—is zero and the Evans function itself never passes through the origin, confirming that no instabilities arise from the point spectrum for the reduced system.

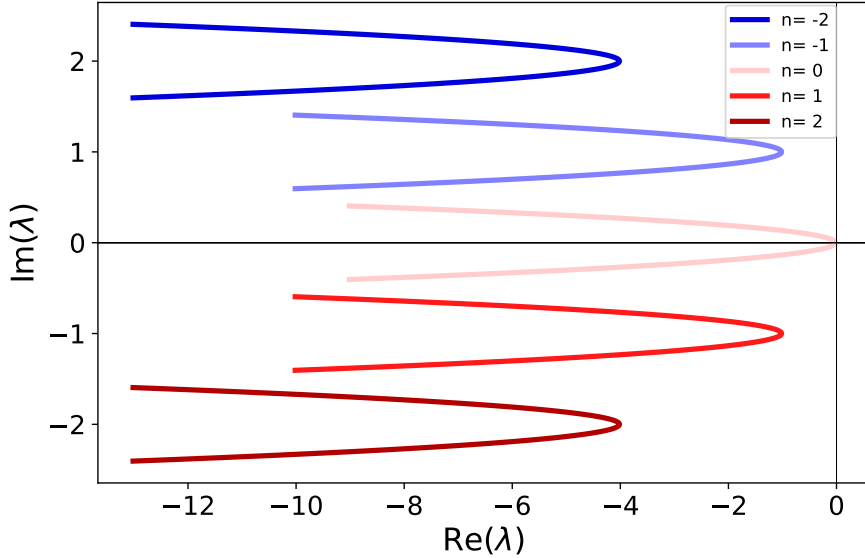


Figure 3.6: The essential spectrum of $\mathcal{L}^{-\infty}$ depicted as a plot of the real vs. the imaginary parts of λ_- as defined in (3.38).

3.9 A note on parameter values

Throughout this work, we fix $l = 0.027$. This value comes from [34], in which the authors calibrate parameters to enforce bistability and arrive at $l = BC = (5.5849 \times 10^2 K)(4.8372 \times 10^{-5} K^{-1}) = 2.7 \times 10^{-2}$. Other authors, such as [30], use $l = 0$ and dispense with the cooling effect entirely. In Chapters 4 and 5 we take $\beta = 0$, resulting in $v_t = 0$ and $v = v^*$ a parameter. For much of the numerical work done in these chapters, we fix $v^* = 0.1$. The ratio of $\frac{l}{v^*} = 0.27$ results in a reaction term with three distinct roots and allows us to investigate the problem's bistability without the risk of entering a parameter regime in which bistability is lost. For larger v^* , the locations of the first two roots of the reaction term $f(u, v^*)$ (see figure 3.3) result in a stiff system of differential equations that is challenging to solve numerically. Still, many of the results in this work for $l = 0.027$ and $v^* = 0.1$ could theoretically be extended to, e.g., the case when $v^* = 1$ and $l = 0.27$ using continuation methods.

3.10 The rest of the problem

In Chapters 4 and 5 we explore the stability of traveling wave solutions to the reduced system (3.30) in the presence of a spatially dependent wind term. Because the problem lends itself to a separation of variables approach, we do this in two parts: Chapter 4 deals with the streamwise structure of the wave and Chapter 5 discusses the transverse structure and properties of the resulting two-dimensional solution. The streamwise stability problem depends on the form of the one-dimensional front solution $\hat{u}(x)$: we begin by demonstrating

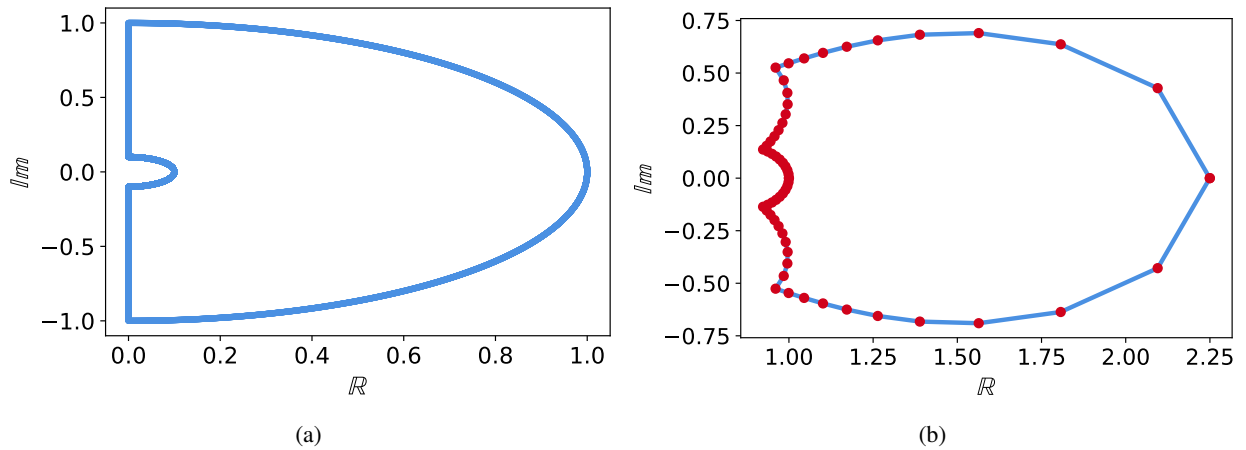


Figure 3.7: (a) The contour of radius 1 on which the Evans function is evaluated, constructed to exclude the origin and (b) the Evans function output, illustrating the location of the zeros of the Evans function when evaluated on the contour shown in (a).

the existence of these solutions for a range of wind speed values and clarifying the conditions necessary for the solution to be unique. We then find the solutions numerically and develop a framework for evaluating their stability. In the following chapter, we use some of the tools developed in Chapter 4 to evaluate the stability of transverse solutions whose spatial structure does not depend on the y coordinate. Finally, we compare our results for transverse and streamwise fronts for complementary wind regimes and develop an understanding of the stability landscape for the two-dimensional fronts.

CHAPTER 4

Streamwise wind variation in the reduced system

4.1 Introduction and motivation

Capturing the spatial structure of traveling fire fronts is key to understanding the means by which these fronts propagate. Generally, it is the structure of the front in the transverse direction—orthogonal to the motion of the fire—that is under consideration. For example, see Canfield and Linn’s 2014 paper for a discussion of the two-way feedback between the shape and curvature of the fireline and its dynamics in simulated grassfires [42]. The structure of the fire in the streamwise direction—parallel to the direction of motion—has been explored much less, although it is known that the thickness of the fireline influences the movement of the fire front. This thickness depends on both the speed of propagation and the residence time, or time to burn, of the fuel. It is the one-dimensional region of transition, consisting of a steep gradient in the temperature, that we focus on in this chapter. See fig. 4.1 for a schematic diagram illustrating this region in the context of a two-dimensional fireline.

The fact that fire generates a local wind field as the result of entrainment of cool air ahead of the fireline is well known: see [43] for an in-depth description of various wind regimes in which this occurs, [44] for a discussion of the phenomenon in coupled fire-atmosphere simulations and [37] for a mathematical treatment of the topic. The generation of this local velocity (referred to as “pyrogenic flow” by [37] and “fire-induced wind” throughout much of this paper) is due to the buoyancy of the air heated by the combustion reaction and the principle of conservation of mass. Specifically, as air heated by the combustion reaction ahead of the fireline rises, cold air is pulled in to replace it.

For a straight, infinite fireline the strongest effects from entrainment are in front of and behind the front, with the entrainment ahead of the fireline occurring in opposition to its motion. In wind-driven fires, where the ambient wind is much larger than the local, fire-induced wind, a wind term that only captures the ambient wind is a reasonable estimation of reality. As a first-order approximation, this wind field may be thought of as constant in space. However, in regimes where the environmental and fire-induced wind are on the same order of magnitude, a wind term that changes in value at a specified spatial location to reflect the entrainment field

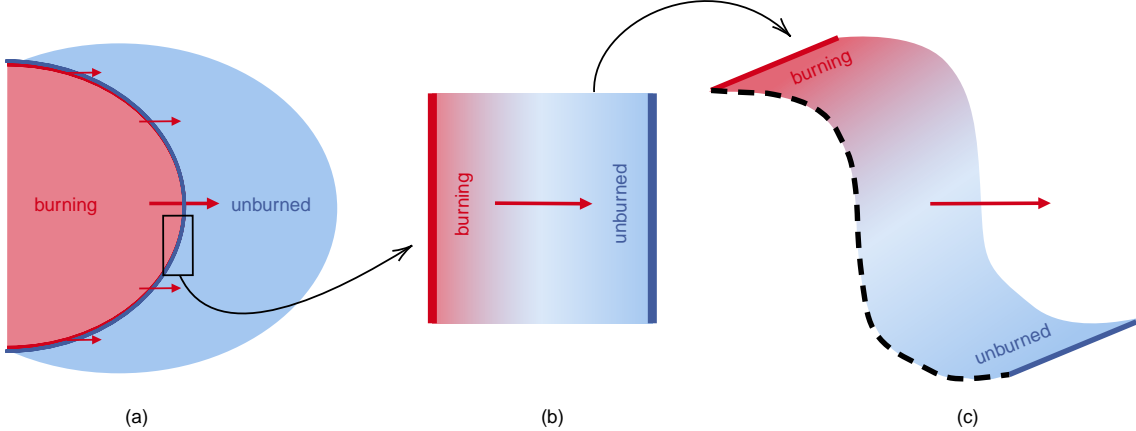


Figure 4.1: The fireline depicted as the boundary between regions of burning and unburned fuel in (a), then zoomed in to illustrate the transition zone between burning and unburned fuel in (b), then viewed again as a two-dimensional object in (c). The profile solutions we consider in this work correspond to the dotted black line in figure (c), asymptotically connecting regions of maximum and ambient temperature (corresponding to regions of burning and unburned fuel). The direction of motion of the fireline and the traveling wave is indicated by the red arrow(s) across all three figures.

and its interactions with the ambient wind is necessary to capture the local wind dynamics.

The implication of the fully-dimensional entrainment phenomenology in the one-dimensional problem is that, in the vicinity of the traveling front, the local velocity field in the streamwise direction switches in magnitude and, potentially, direction. In this chapter, we consider a generalized spatially dependent wind term that captures this switching behavior and explore how the constraints on existence and stability of solutions to a minimal model of fire propagation dictate the preferred wind configuration.

We consider a one-dimensional, nonlinear reaction-diffusion equation for the temperature of a region of burning fuel. Partial differential equations of this form have been used as a minimal model for combustion in a variety of settings (including [34], [28], [29] and [45]) in part because they admit traveling wave solutions that may be used to model propagating combustion fronts. We impose the fire-induced wind due to the entrainment field as a first-order forcing term. The existence and stability of traveling wave solutions in the constant wind case to equations of this form is well understood: see [46] for the general theory. For a spatially dependent wind term, these issues are less well understood. We use a dynamical systems framework to address both the existence and stability problem. Through a combination of geometric arguments and numerical calculations, we demonstrate the existence of traveling front solutions for a range of wave speed values dependent on the wind regime parameters. We further demonstrate that the stability properties of these

solutions depend on the qualitative nature of the wind field.

These results give us tools to better understand the properties of the solution that will persist in nature in a system with a spatially dependent wind. We identify the unique speed at which the preferred front travels as well as the relationship between the spatial location of the fire front and that of the wind switch. These findings allow us to identify, for a given wind configuration, the expected distance between and relative location of the fireline and the wind switch. We find that, for the spectrally preferred solution, the wind switch occurs ahead of the fireline. This is reflective of the physical motivation described above: propagating fires will entrain cool air ahead of the fireline. It is noteworthy that, despite not modeling the wind or coupling it to the temperature, the minimal, temperature-based model of fire propagation discussed in this chapter is able to describe a physically relevant fire-induced wind.

4.2 The reduced system in one dimension

We consider the one-dimensional analogue to (3.30)

$$\frac{\partial u}{\partial t} = \frac{\partial^2 u}{\partial z^2} + (c - w(z)) \frac{\partial u}{\partial z} + v^* r(u) - lu \quad (4.1)$$

which models the evolution of the temperature $u(x, t)$ of the fire layer, consisting of a fixed, one-dimensional region of homogeneous fuel and the layer of air immediately above it. Recall that we are interested in steady-state front solutions satisfying

$$0 = \frac{\partial^2 u}{\partial z^2} + (c - w(z)) \frac{\partial u}{\partial z} + v^* r(u) - lu \quad (4.2)$$

Recasting the system as first order we obtain

$$\begin{aligned} u' &= s \\ s' &= -(c - w(z))s - v^* r(u) + lu \end{aligned} \quad (4.3)$$

4.3 Constant wind

In the case when the wind term is homogeneous in space, traveling wave solutions to (4.1) are heteroclinic connections between the fixed points found as zeros of (3.20). In the context of the ODE system (4.3) with such a wind term, $(u_0, 0)$ and $(u_2, 0)$ are saddles. These points define boundary conditions for the traveling wave in the (u, s) system: as we take our traveling coordinate z to negative infinity, the solution trajectory

asymptotically approaches the point $(0,0)$. As we take our traveling coordinate z to positive infinity, it approaches $(u_2,0)$.

Classical theory tells us that solutions \hat{u} to the corresponding second-order system (4.1) with a constant wind term exist only for a unique wave speed $c = \hat{c}$ (see [22]). We outline two approaches for finding these solutions.

4.3.1 Solutions in phase space

The first method exploits the geometric structure described above. We reframe the first order system (4.3) as two initial value problems, one initiated near $(u_0, s_0) = (0, 0)$ and one near $(u_0, s_0) = (u_2, 0)$. The wave speed c is a free parameter, and one can numerically integrate forwards from $(0, 0)$ and backwards from $(u_2, 0)$ to obtain solution trajectories for each initial value problem and choice of c . The c value for which these solution trajectories coincide in a single, heteroclinic orbit is \hat{c} , the unique wave speed for which a profile solution exists. These solutions exist in phase space. However, reframing them in $(z, u(z))$ space—with the proper parameterization—allows us to reconstruct the profile solution.

4.3.2 Solutions to the boundary value problem

The second option bypasses the phase space point of view entirely and instead considers the second-order system (4.1) as a boundary value problem with boundary conditions given by

$$\begin{aligned} \lim_{z \rightarrow -\infty} \hat{u}(z) &= 0 \\ \lim_{z \rightarrow \infty} \hat{u}(z) &= u_2 \end{aligned} \tag{4.4}$$

The wave speed c is a free parameter that is solved for alongside u .

The boundary value approach is efficient and allows us to easily specify the desired error tolerance when solving for \hat{c} . Either method allows us to find profile solutions and wave speeds that vary as a function of the initial fuel load parameter v^* . A key point is that, for all values of $v^* \in [0, 1]$, $\hat{c} < 0$. This aligns with our physical understanding that the traveling front moves from regions of maximum temperature (representing burning fuel) to regions of ambient temperature (representing unburned fuel) as the fire progresses. The sign of \hat{c} will also be an important point in our investigation of the system with a spatially dependent wind.

4.3.3 Stability

We linearize the second order problem (4.1) about solutions to (4.2), denoted \hat{u} . The resulting eigenvalue problem in linearized coordinates p is

$$\omega p = p_{zz} + (c - w)p_z + f'(\hat{u})p \quad (4.5)$$

where

$$f'(u(z)) = \begin{cases} \frac{v^*}{u^2} \exp\left(-\frac{1}{u}\right) - l & u(z) > 0 \\ -l & u(z) = 0 \end{cases} \quad (4.6)$$

Note that (4.5) is the constant coefficient, one-dimensional analogue of the secondary eigenvalue problem (3.35) introduced in Chapter 3, where ω is the streamwise eigenvalue.

It is well known (see [21]) that the boundary of the essential spectrum of the operator \mathcal{L} associated with (4.5) is given by the spectrum of the operator $\mathcal{L}^{\pm\infty}$, where the latter is determined by evaluating \mathcal{L} at the profile solution \hat{u} and taking the limit as $z \rightarrow \pm\infty$. A straightforward algebraic argument demonstrates that the essential spectrum lies in the left half-plane. For details as to how this calculation works in a similar system, see [45]. There is also an eigenvalue at the origin reflective of the translational invariance of the traveling wave: the monotonicity of the profile and an application of Sturm-Liouville theory tells us that the translational eigenvalue is the largest eigenvalue for any given solution (for details, see [47]). This in turn implies that the wave is spectrally stable.

The conclusion is that, in the spatially homogeneous wind case, profile solutions exist to (4.1) that move with a unique wave speed. These solutions are spectrally stable for all values of the wind speed and translates of the front are also solutions. We will see that, in the spatially dependent wind case, these results do not hold: solutions exist for a continuum of wave speeds and translational invariance is broken.

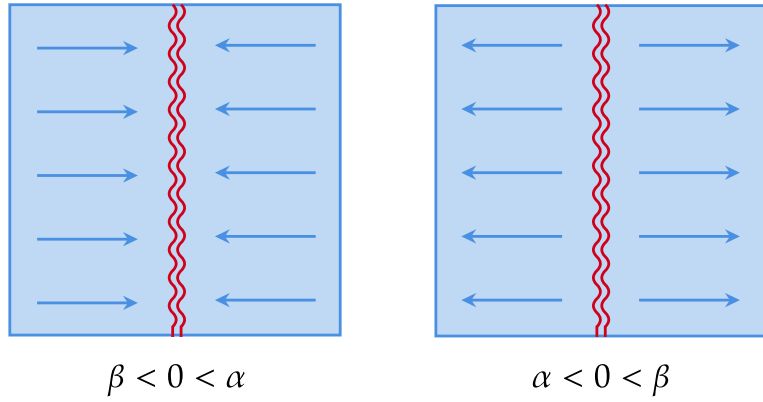


Figure 4.2: Two possibilities for the spatially dependent wind configuration. The first illustrates a convergent wind field and the second a divergent wind field. The fireline is indicated in red.

4.4 Constructing the spatially dependent wind

To introduce the switching phenomenon described in §4.1, we use a discontinuous step function whose magnitude is controlled by the parameters α and β :

$$w(z) = \begin{cases} \alpha & z < 0 \\ 0 & z = 0 \\ \beta & z > 0 \end{cases} \quad (4.7)$$

This leaves us with two potential situations: either $\alpha > \beta$ or $\alpha < \beta$. As a special case of the first option, we might consider the situation in which $\beta < 0 < \alpha$, resulting in a wind field that converges at the fireline. Alternatively, as a special case of the second option, we consider $\alpha < 0 < \beta$, resulting in a divergent wind field. The first case describes the fire-induced wind introduced in §4.1. The second case is physically unlikely, but presents a relevant mathematical foil that will help us better understand the physical implications of our results.

Recall that in the case of constant wind, traveling wave solutions exist for a unique \hat{c} . In the spatially dependent wind case, the situation is more complicated: solutions exist for a range of c values, each corresponding to a different profile shape. We will use the structure outlined in §4.3 as a guide for our analysis of the spatially dependent wind case.

4.5 Solutions in phase space with a spatially dependent wind

With the nonconstant wind term (4.7) the ODE governing the front solutions (4.3) is now non-autonomous.

As a first order autonomous system, this becomes

$$\begin{cases} u' = s \\ s' = -(c - w(z))s - v^*r(u) + lu \\ z' = 1 \end{cases} \quad (4.8)$$

The system (4.8) has traveling wave solutions $\hat{u}(z)$ that exist for some bounded continuum of wave speeds c . There exists a set of orbits connecting the point $(u, s) = (0, 0)$ as $z \rightarrow -\infty$ and the point $(u, s) = (u_2, 0)$ as $z \rightarrow +\infty$. We can think of the dynamics projected onto the plane $z' = 1$ and therefore reduced to a two-dimensional phase space in which both of these points are equilibria. The unstable manifold of the first fixed point is a two-dimensional structure that intersects with the Poincaré section at $z = 0$ in a one-dimensional curve, as is the stable manifold of the second fixed point. The point of intersection of these curves on the plane $z = 0$ can then be traced back to the fixed points at $\pm\infty$ to form the heteroclinic connection, as illustrated in figure 4.3.

This view gives us two different systems for $z < 0$ and $z > 0$.

For $z < 0$:

$$\begin{aligned} u'_- &= s_- \\ s'_- &= -c_1^*s_- - f(u_-) \end{aligned} \quad (4.9)$$

where $c_1^* = c - \alpha$. For $z > 0$:

$$\begin{aligned} u'_+ &= s_+ \\ s'_+ &= -c_2^*s_+ - f(u_+) \end{aligned} \quad (4.10)$$

where $c_2^* = c - \beta$. Values of c for which solution trajectories to the systems (4.9) and (4.10) intersect are values of c for which a solution exists to the full system (4.3) with the wind switch.

To find these values we consider solution trajectories for (4.9) originating at the fixed point $(0, 0)$ and

tangent to the unstable subspace of that fixed point as well as trajectories for (4.10) originating at the fixed point $(u_2, 0)$ tangent to the stable subspace for that system. These trajectories are invariant manifolds for their respective system parameterized by the wave speed c , which is common to both systems.

The point of intersection of the manifolds corresponds to the location of the wind switch and the point on the profile where the derivative $u' = s$ is maximized corresponds to the location of the fireline. We may pick our parameterization based on either of these points: a natural choice, since we define the wind switch as occurring at $z = 0$ in (4.7), is to fix the point of intersection of the manifolds at $z = 0$.

4.5.1 Finding the invariant manifolds and their intersections

The fixed points of (4.9) and (4.10) are the same as the fixed points of (4.3) in the constant wind case and so are given by the zeros of (3.20). Again, they are saddles. Denoting a fixed point (u, s) of either system as $(u^*, 0)$, the matrix associated with the linearization of the system about the fixed point is

$$M_{\pm} = \begin{bmatrix} 0 & 1 \\ -f'(u^*) & -c^* \end{bmatrix} \quad (4.11)$$

where $c^* = c_1^*$ or c_2^* as appropriate and f' is defined as in (4.6). For the fixed point $(u_2, 0)$ at positive infinity, the stable eigenvalue of the linearization is

$$\lambda_s = \frac{-c_2^* - \sqrt{c_2^{*2} - 4(f'(u_2))}}{2} \quad (4.12)$$

and the corresponding eigenvector is

$$\pm \vec{v}_s = \pm \begin{pmatrix} 1 \\ \lambda_s \end{pmatrix} \quad (4.13)$$

Similarly, for the fixed point $(0, 0)$ at negative infinity, the unstable eigenvalue of the linearization is

$$\lambda_u = \frac{-c_1^* - \sqrt{c_1^{*2} + 4l}}{2} \quad (4.14)$$

and the corresponding eigenvector is

$$\pm \vec{v}_{us} = \pm \begin{pmatrix} 1 \\ \lambda_{us} \end{pmatrix} \quad (4.15)$$

We perturb the fixed point at $-\infty$ in the unstable direction to determine an initial condition. We then integrate forward from this initial condition to find the unstable manifold, treating our PDE as an initial value problem. We take a similar approach for the stable manifold originating from the fixed point at $+\infty$. The range of c values for which intersections exist depends on the relative values of the wind speed parameters α and β . These results are summarized in Proposition 1.

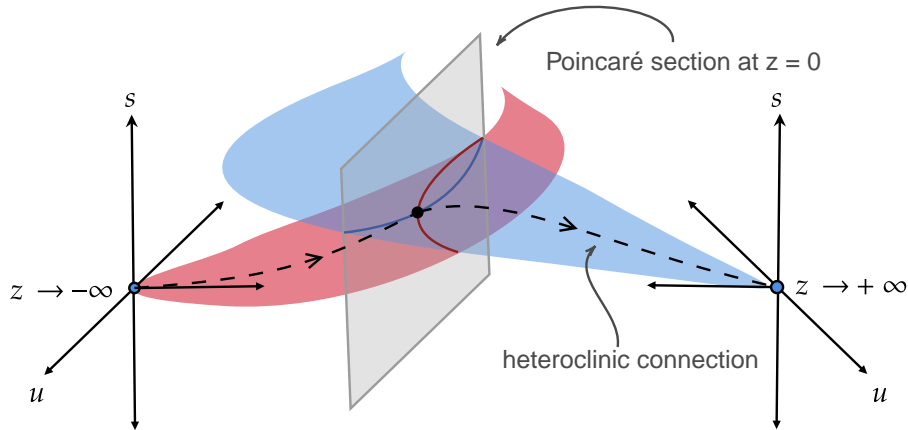


Figure 4.3: The three-dimensional phase space described in §5. The blue plane is the stable manifold of the fixed point $(u_2, 0)$ for the system at $+\infty$ and the red plane is the unstable manifold of the fixed point $(0, 0)$ for the system at $-\infty$. The solid blue and red curves indicate the intersections of these manifolds with the plane $z = 0$. The point of intersection of the solid curves can be traced back across the unstable manifold and forward across the stable manifold to find the heteroclinic connection between $(0, 0)$ and $(u_2, 0)$.

Proposition 1. If $\alpha > \beta$, the unstable manifold of the fixed point $(0, 0)$ of (4.9) intersects the stable manifold of the fixed point $(u_2, 0)$ of (4.10) when $c_1^* < \hat{c}$ and $c_2^* > \hat{c}$, where \hat{c} is the unique wave speed for which solutions exist when $\alpha = \beta = 0$ (or equivalently, the wind is constant across the spatial domain). If $\alpha < \beta$, this intersection occurs for $c_1^* > \hat{c}$ and $c_2^* < \hat{c}$. This corresponds to $\hat{c} + \alpha < c < \hat{c} + \beta$ when $\alpha > \beta$ and $\hat{c} + \beta < c < \hat{c} + \alpha$ when $\alpha < \beta$.

Proof. We consider $\mathcal{W}_0^u(c)$, the unstable manifold originating at $(0, 0)$ representing a solution trajectory of (4.9) with initial condition $(0, 0)$ and speed c . $\mathcal{W}_0^u(c)$ is parameterized in forward “time,” meaning that the independent variable z goes from $-\infty$ to $+\infty$ along the course of the trajectory.

$\mathcal{W}_{u_2}^s(c)$ is the stable manifold originating from $(u_2, 0)$ representing a solution trajectory of (4.10) with initial condition $(u_2, 0)$ and speed c . $\mathcal{W}_{u_2}^s(c)$ is parameterized in backward “time,” so the independent variable z goes from $+\infty$ to $-\infty$ along the course of the trajectory. Note that when $c = \hat{c}$ these manifolds coincide,

meaning $\mathcal{W}_{u_2}^s(\hat{c}) = \mathcal{W}_0^u(\hat{c})$.

$\mathcal{W}_{u_2}^s(c)$ and $\mathcal{W}_0^u(c)$ are parameterized by the same wave speed c , which may or may not be a value of c for which there is a solution for the entire system with the wind switch. For values of c for which $\mathcal{W}_{u_2}^s(c)$ and $\mathcal{W}_0^u(c)$ intersect, there is such a solution.

We also consider the energy of the system, defined by the Hamiltonian associated with (4.3) when $c^* = 0$:

$$H(u, s) = \frac{1}{2}s^2 + \int_0^u f(r)dr \quad (4.16)$$

The derivative of (4.16) along trajectories is

$$\frac{d}{dz}H(u(z), s(z)) = -c^*s^2 \quad (4.17)$$

If $c^* = 0$, $\frac{dH}{dz}$ is also zero along trajectories, meaning H is constant along trajectories, so level sets of (4.16) are solution trajectories of (4.3).

The derivative of the Hamiltonian, (4.17), gives us information about the rate of change of energy along trajectories when $c^* \neq 0$. In particular, recall that $\hat{c} < 0$ for $v^* \in [0, 1]$. In the case of constant wind, this means that $c^* = \hat{c} < 0 \implies \frac{dH}{dz} > 0$, meaning energy is increasing along trajectories that are parameterized in forward z and decreasing along trajectories parameterized in backward z .

Case 1. $\alpha > \beta$,

Consider $c_1^* = c - \alpha$. Assuming non-constant wind, either (a) $c_1^* > \hat{c}$ or (b) $c_1^* < \hat{c}$. If option (a) holds, $\frac{dH}{dz}(c_1^*) < \frac{dH}{dz}(\hat{c})$, meaning that energy increases less along the trajectories defined by $\mathcal{W}_0^u(c_1^*)$ than those defined by $\mathcal{W}_0^u(\hat{c})$. This, combined with the fact that the second component of the eigenvector from $(0, 0)$ in the unstable direction is given by the unstable eigenvalue (4.14) so that $c_1^* > \hat{c} \implies \lambda_{us}(c_1^*) < \lambda_{us}(\hat{c})$, means that trajectories $\mathcal{W}_0^u(c_1^*)$ will always lie below trajectories $\mathcal{W}_0^u(\hat{c})$ in phase space for case (a). If $\mathcal{W}_{u_2}^s(c_2^*)$ is to intersect $\mathcal{W}_0^u(c_1^*)$ it must also lie below $\mathcal{W}_0^u(\hat{c}) = \mathcal{W}_{u_2}^s(\hat{c})$. Because $\mathcal{W}_{u_2}^s$ is parameterized in backwards z , this requires $\frac{dH}{dz}(c_2^*) > \frac{dH}{dz}(\hat{c})$ in forward z . This implies that $c_2^* < \hat{c} \implies c - \beta < \hat{c} \implies c < \hat{c} + \beta$, and the condition on the stable manifold gives $c > \hat{c} + \alpha$. But this implies $\alpha < \beta$, contradicting our initial assumption.

So it must be that option (b) holds, meaning that $\frac{dH}{dz}(c_1^*) > \frac{dH}{dz}(\hat{c})$, meaning that energy increases more along the trajectories defined by $\mathcal{W}_0^u(c_1^*)$ than those defined by $\mathcal{W}_0^u(\hat{c})$. In this case, $\lambda_{us}(c_1^*) > \lambda_{us}(\hat{c})$, which means that trajectories $\mathcal{W}_0^u(c_1^*)$ will always lie above trajectories $\mathcal{W}_0^u(\hat{c})$ in phase space. This implies that

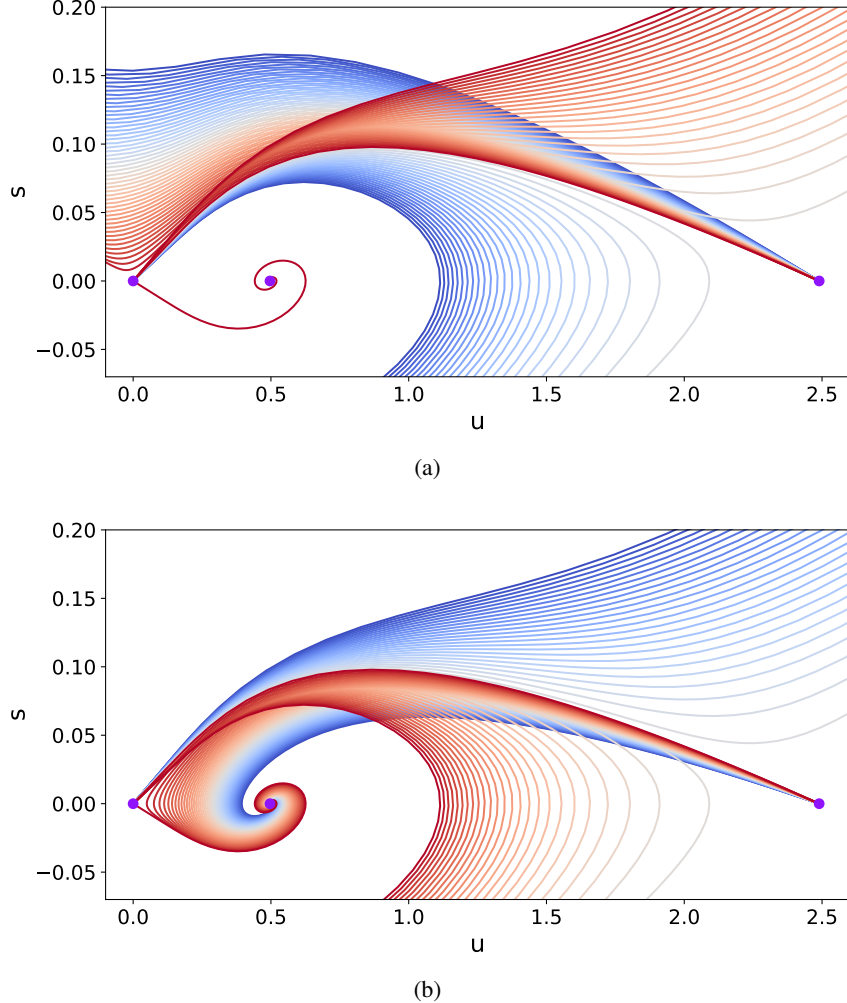


Figure 4.4: Invariant manifolds color-coded by wave speed value $c \in (-0.045, -0.125)$. (a) depicts type 1 intersections, while (b) depicts type 2 intersections for $c \in ()$. The fixed points $(0,0)$, $(u_1,0)$ and $(u_2,0)$ are indicated in purple. Note the different qualitative nature of the intersections in (a) versus those in (b).

$c_2^* > \hat{c}$ and therefore $\hat{c} + \beta < c < \hat{c} + \alpha$, which is consistent with our initial assumption that $\alpha > \beta$.

To demonstrate that $\mathcal{W}_0^u(\hat{c})$ and $\mathcal{W}_{u_2}^s(\hat{c})$ do in fact intersect for $c_1* < \hat{c} < c_2^*$, consider the lines $u = 0$ and $u = u_2$. We know that \mathcal{W}^u originates at the point $(0,0)$ on the line $u = 0$ and, because it is bounded, must intersect the line $u = u_2$. An analogous argument holds for \mathcal{W}^s and the line $u = 0$.

To see that the manifolds are bounded, we make the change of variables $s(z) = \exp(-c^*z)b(z)$. Then, the ODE for s' in (4.3) becomes $b' = -f(u)$. Integrating, we find

$$b(z) = - \int_{-\infty}^{\infty} f(u(z)) dz$$

The right hand side is bounded for $u \in [0, u_2]$ (see figure 1), so we may conclude that $s(z)$ is also bounded in that range.

Interpreting \mathcal{W}^s and \mathcal{W}^u as functions $\mathcal{W}: u \rightarrow s$, we further define $\mathbf{d}(u) = s_1(u) - s_2(u)$, where $s_2 = \mathcal{W}^s(u)$ and $s_1 = \mathcal{W}^u(u)$. The energy argument above tells us that s_1 and s_2 lie above the u axis. So, we have:

$$\begin{aligned}\mathbf{d}(u=0) &= 0 - s_2(0) < 0 \\ \mathbf{d}(u=u_2) &= s_1(u_2) - 0 > 0\end{aligned}\tag{4.18}$$

Both \mathcal{W}^u and \mathcal{W}^s are continuous functions of z because they are solution trajectories parameterized in z . Further, the fact that u is a monotone bounded function of z follows from the fact that $s > 0 \implies u' = s > 0$ and s is bounded, as demonstrated in part (1). This, together with the fact that $u(z)$ satisfies the intermediate value property for $z \in (-\infty, \infty)$, gives us that u is a continuous function of z . Therefore its inverse, $z(u)$, is also continuous. Because the composition of continuous functions is continuous, we conclude that both \mathcal{W}^u and \mathcal{W}^s are continuous functions of u . Finally, because \mathbf{d} is a continuous function of u and switches signs in the interval $[0, u_2]$, there must be a point $u^* \in [0, u_2]$ such that $\mathbf{d}(W_0^u(c_1^*), W_{u_2}^s(c_2^*), u^*) = 0$, meaning that \mathcal{W}_0^u and $\mathcal{W}_{u_2}^s$ intersect at this point.

Case 2. $\alpha < \beta$

By the same logic as case 1, we must have $c_2^* < \hat{c}$ and $c_1^* > \hat{c}$ in order for \mathcal{W}_0^u and $\mathcal{W}_{u_2}^s$ to intersect, giving us $\hat{c} + \alpha < c < \hat{c} + \beta$. In this case, the sign of $\frac{dH}{dz}$ and the magnitude of the eigenvector in the stable direction tells us that $\mathcal{W}_0^u(c_1^*)$ and $\mathcal{W}_{u_2}^s(c_2^*)$ must both lie below $\mathcal{W}_{u_2}^s(\hat{c}) = \mathcal{W}_0^u(\hat{c})$.

The fixed point $(u_1, 0)$ is either an unstable node or an unstable spiral for the systems from both $-\infty$ and $+\infty$. This implies that $(u, s) = (u_1, 0)$ is the α limit set of the system from positive infinity, meaning that $\mathcal{W}_{u_2}^s$ must approach the point $(u_1, 0)$ as $z \rightarrow -\infty$.

If $(u_1, 0)$ is a node for this system, this guarantees that the trajectory from $+\infty$ asymptotically approaches the point $(u_1, 0)$. On the other hand, because $(u_1, 0)$ is an unstable fixed point for the system from $-\infty$, which is parameterized in forward time, the ω limit set does not exist. Therefore, the trajectory from $-\infty$ diverges as $z \rightarrow +\infty$.

To see that solution trajectories for the systems at both $\pm\infty$ must cross the u axis in specific regions,

consider the vector field along that axis:

$$u' = 0$$

$$s' = -f(u)$$

where the graph of $-f(u)$ is positive for $0 < u < u_1$ and negative for $u_1 < u < u_2$.

It follows that if \mathcal{W}_0^u is to intersect the u axis, it must do so in the region $u > u_1$ due to the direction of the vector field along the axis. The opposite is true for $\mathcal{W}_{u_2}^s$, as it is parameterized in backwards z : if it intersects the u axis, it must do so in the region $u < u_1$. Because the solution trajectories to both systems are bounded and lie below the trajectory associated with \hat{c} , which intersects the u axis, they must both intersect it as well: the above bounds on where they may do so means that they must also intersect each other. \square

4.5.2 Stability properties of different intersection types

We now have a natural means of classifying intersection types: either $\beta < \alpha$, resulting in “type 1” intersections, or $\alpha < \beta$, resulting in “type 2” intersections. Numerical investigation (see figure 4) reveals that these two types of intersections are qualitatively different, and this qualitative difference translates to a difference in the stability properties of the intersections. These properties are summarized in Proposition 2.

Proposition 2. Intersections of type 1 correspond to stable fronts while intersections of type 2 correspond to unstable fronts.

Proof. Case 1. $\alpha > \beta$: type 1 intersections

Define the tangent vector associated with the \mathcal{W}_0^u at the point of intersection as v_0^u and the tangent vector associated with the $\mathcal{W}_{u_2}^s$ at the point of intersection as v_0^s . At the point of intersection, v_0^u is evolved according to the flow along $\mathcal{W}_{u_2}^s$. Call the resulting vector at the point $(u, s) = (u_2, 0)$ v_f^u and the tangent vector to the stable manifold at that point v_f^s .

Note that, because v_0^u and v_0^s are tangent to the unstable and stable manifolds, their components are determined by the vector field of the corresponding systems, namely (4.9) and (4.10). The corresponding matrix is

$$A = \begin{pmatrix} u'_- & u'_+ \\ s'_- & s'_+ \end{pmatrix} \quad (4.19)$$

and

$$\det(A) = u'_- s'_+ - s'_- u'_+ = (c_1^* - c_2^*)s^2 \quad (4.20)$$

For intersections of type 1, $c_2^* < \hat{c} < c_1^*$ means $\det(A) > 0$ and the tangent vectors therefore constitute a positively oriented basis for \mathbb{R}^2 . Uniqueness of solutions to differential equations requires that the orientation between the vectors be preserved, so the orientation of the basis associated with $[v_f^u, v_f^s]$ must also be positive.

Next, consider the angular eigenvalue system, obtained by converting the eigenvalue problem associated with (4.1) to polar coordinates in phase space (the Prüfer variables defined in Chapter 2) and noting that the equation for θ is independent from that for r , where ω is the streamwise eigenvalue:

$$\dot{\theta} = -(f'(\hat{u}) - \omega) \cos^2 \theta - (c - w(z)) \cos \theta \sin \theta - \sin^2 \theta \quad (4.21)$$

which has fixed points $\theta_{u/s}^\pm$ corresponding to the unstable/stable directions at $\pm\infty$, given by:

$$\begin{aligned} \theta_{-u/s} &= \arctan \left(\frac{-(c + \beta) \pm \sqrt{(c + \beta)^2 + 4(\omega - f'(u_2))}}{2} \right) \\ \theta_{u/s}^- &= \arctan \left(\frac{-(c + \alpha) \pm \sqrt{(c + \alpha)^2 + 4(\omega + l)}}{2} \right) \end{aligned} \quad (4.22)$$

If a given value of ω is an eigenvalue, the corresponding solution trajectory to (4.21) with initial condition θ_u^- must approach $\theta_f = \theta_s^+ + n\pi$ as $z \rightarrow \infty$ for some integer n .

Fix $\omega = 0$ and define θ_f as the angle between the positive u axis and v_f^s . A standard argument shows that 0 is not an eigenvalue, so we cannot have $\theta_f = \theta_s^+$. In fact, because of the positive orientation of $[v_f^u, v_f^s]$, it must be that $\theta_f > \theta_s^+$. Because θ_f must be aligned with an invariant subspace at $+\infty$ it must be that $\theta_f = \theta_u^+$ when $\omega = 0$.

Now, because θ_f is a piecewise monotone function of ω , $w > 0 \implies \theta_f \geq \theta_u^+$, as varying ω induces counter-clockwise rotation. But, because the vector field along the line $\theta = \frac{\pi}{2}$ is positive, meaning it points in the clockwise direction, θ is unable to rotate through this axis. We conclude that, for $\omega > 0$, $\theta_f = \theta_u^+$ and, by definition, ω is not an eigenvalue. As there are no eigenvalues in the right half plane, type 1 intersections correspond to stable solutions.

Case 2. $\alpha < \beta$: type 2 intersections

In this case, $c_1^* < \hat{c} < c_2^*$ means $\det(A) < 0$ and the basis associated with the tangent vectors $[v_0^u, v_0^s]$ at

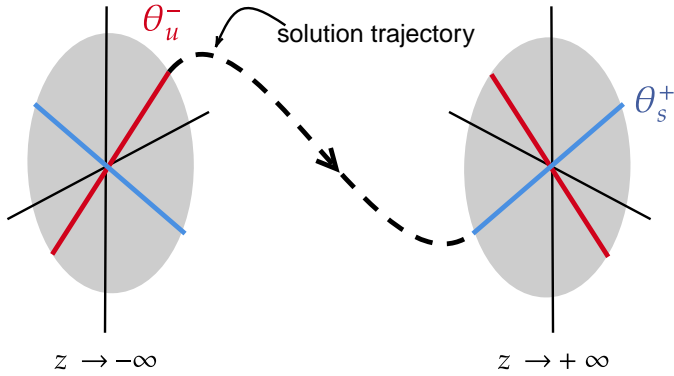


Figure 4.5: Phase portraits for the angular systems at $-\infty$ and $+\infty$ with a sample solution trajectory moving from θ_u^- to θ_s^+ . Unstable manifolds for each system are indicated in red and stable manifolds in blue.

the point of intersection is negatively oriented, as is the basis associated with $[v_f^u, v_f^s]$.

Again, fix $\omega = 0$. By the same logic as in case 1, 0 is not an eigenvalue: the orientation of $[v_f^u, v_f^s]$ means we must have $\theta_f = \theta_u^+ + \pi$. For $\omega >> 0$, θ_f approaches θ_u^+ as the growing value of ω overcomes the effect of the nonlinear reaction term. In doing so, it must pass through $\theta_s^+ + \pi$ for some value of $\omega > 0$. Therefore, for intersections of type 2, there is at least one value of ω in the right half plane. The corresponding solution is unstable. \square

The geometric approach described in this section allows us to reconstruct profile solutions and identify the intersection types corresponding to stable profiles. However, we are left with a range of stable—and therefore physically viable—fronts and no means of picking an unique front solution from the continuum of possibilities. In the next two sections, we develop tools to identify the preferred solution.

4.6 Profile solutions to the boundary value problem with a spatially dependent wind

In §4.7, we will seek to determine the preferred wave speed and corresponding solution by finding the minimizer of the largest eigenvalue associated with each wave speed/solution pair. This approach requires that we have access to very accurate numerical representations of the solutions whose existence we demonstrated in Proposition 1. As in the constant wind case, we accomplish this by framing our problem as a boundary value problem in which the wave speed c is a free parameter.

The system (4.3) is defined for $z \in (-\infty, \infty)$, so we look for profile solutions by solving the two-point boundary value problem on this domain, where the problem is given by (4.3) with wind term (4.7) and boundary conditions (4.4). We also have a condition on the derivative of the profile, which takes the form of a

pulse:

$$\lim_{z \rightarrow \pm\infty} s = 0 \quad (4.23)$$

We follow the technique outlined in [23], slightly modified to allow for a discontinuous wind. We employ projective boundary conditions

$$P_\pm(U(\pm L) - U_\pm) = 0 \quad (4.24)$$

where $U = (u, s)$, $U_+ = (u_2, 0)$, $U_- = (0, 0)$ and we take $\pm L$ to be sufficiently large so as to approximate numerical infinity.

There exists a one-parameter family of solutions indexed by the wave speed c . To pick a single solution from this family, we specify a phase condition

$$\text{phase}(\gamma) = \gamma u_2 + (1 - \gamma)u_0 \quad (4.25)$$

for $\gamma \in [0, 1]$. This phase condition serves as an additional boundary condition specifying the spatial location of the center of the profile, which corresponds exactly to the position of the fireline as determined by the point where the derivative $u' = s$ is at a maximum. Imposing a phase condition allows us to leave the wave speed c as an unknown to be solved for, whereas in §7 we specified c and found the intersections of the resulting invariant manifolds in $(u, s(u))$ space.

A number of pre-packaged solvers exist for two-point BVPs, so it is convenient to transform our three-point BVP in to a two-point BVP by doubling the size of the system and halving the domain. Lastly, to account for the unknown wave speed parameter, we augment the system with the additional relation $c' = 0$. Then, (4.3) becomes

$$\begin{aligned} u'_0 &= s_0 \\ s'_0 &= -(c - w(z))u_0 - f(u_0) \\ u'_1 &= -s_1 \\ s'_1 &= (c - w(z))u_1 + f(u_1) \\ c' &= 0 \end{aligned} \quad (4.26)$$

for $z \in [0, L]$. To close the system, we introduce a set of matching conditions at the $z = 0$ boundary, resulting

in five total boundary conditions for our five-dimensional system. The resulting solutions are smooth profiles asymptotically connecting $u = 0$ to $u = u_2$, as expected.

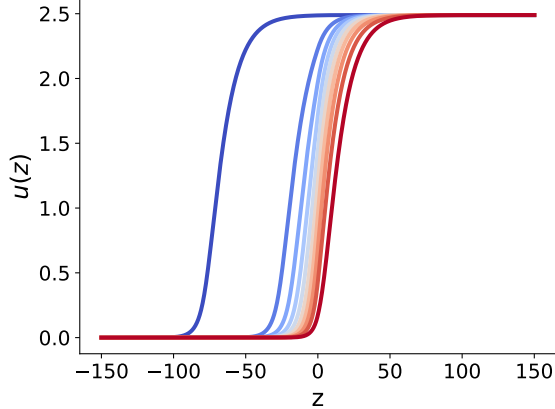


Figure 4.6: Profile solutions found using the method described in §4.6, for $v^* = 0.1$, $l = 0.027$, $\alpha = 0.05$, $\beta = -\alpha$, color-coded by wave speed c . In this case, $u_2 \approx 2.5$.

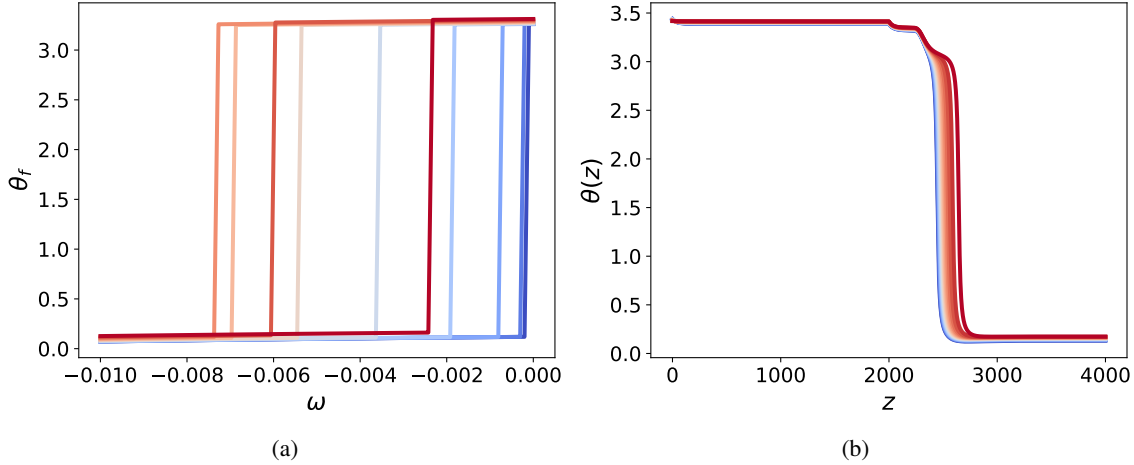


Figure 4.7: (a) shows the accumulated angle for a range of c values as a function of ω . Vertical jumps indicate the ω value that is an eigenvalue for that value of c and corresponding solution. (b) shows an alternate view of the same idea. The solution trajectories are color-coded by ω values. If the solution jumps by a factor of π as $z \rightarrow \infty$, the corresponding value of ω is an eigenvalue. It is worth noting that at the exact value of ω that is an eigenvalue, the solution in θ will not have a jump. The depicted solutions occur just after the eigenvalue.

4.7 Stability as a selection mechanism for the preferred wave

The results presented in Propositions 1 and 2 give us a means of understanding the existence and stability of traveling front solutions to (3.19) with a discontinuous wind. In particular, these results affirm our physical intuition: for a divergent wind field—corresponding to $\alpha < \beta$ and type 2 intersections—the front is unstable, whereas for a convergent wind—representative of the fire-induced wind described in §4.1 and corresponding

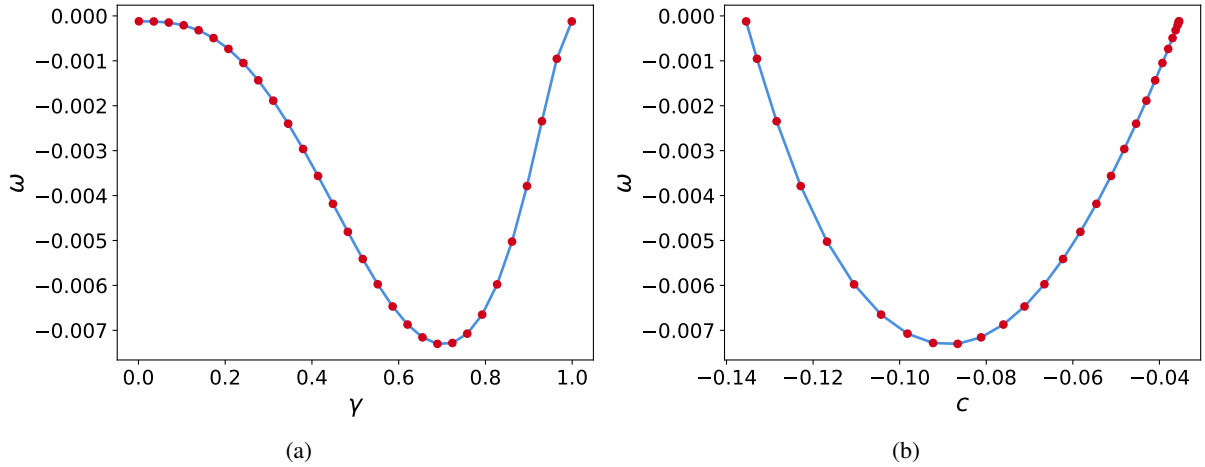


Figure 4.8: The largest eigenvalue ω as a function of the phase γ in figure (a) and the wave speed c in figure (b). Both views demonstrate a clear minimum and an inverted parabolic structure.

to $\alpha > \beta$ and type 1 intersections—the front is reinforced by the wind field and the solution is stable.

We expect for stable fronts—those whose speeds fall in the range $\hat{c} + \alpha < c < \hat{c} + \beta$ —to persist in nature, so we focus the remainder of our analysis on traveling fronts resulting from type 1 intersections. The solutions we found in §4.6 for a wind term satisfying this inequality exist for a range of phase conditions, just as intersections of the invariant manifolds discussed in §4.6 exist for a range of wave speeds. However, without a means of selecting a single wave speed from the continuum of possibilities, the solution for the system with a spatially dependent wind term is not unique.

A reasonable means of identifying the preferred solution is to identify the solution whose largest (meaning least negative) streamwise eigenvalue ω is minimized across possible phase conditions or, equivalently, wave speeds. Because perturbations to this solution will decay the fastest, it is in a sense the “most stable” of the possible solutions. Out of the continuum of possible stable solutions, this spectrally preferred solution corresponds to the traveling front that will persist in nature.

To find the largest eigenvalue for each profile solution found in §8, we again turn to the angular formulation given in (4.21). Solutions take the form of trajectories that originate on the unstable manifold of the fixed point $(0, 0)$ for the system at $-\infty$ and terminate on the stable manifold of the fixed point $(u_2, 0)$ for the system at $+\infty$, where the two systems are differentiated by the wind term, as in (4.9) and (4.10).

If some value of the eigenvalue parameter ω is in fact an eigenvalue, the corresponding trajectory in the

angular system $\theta(z)$ will satisfy the following conditions:

$$\begin{aligned}\lim_{z \rightarrow -\infty} \theta &= \theta_u^- \\ \lim_{z \rightarrow +\infty} \theta &= \theta_s^+\end{aligned}\tag{4.27}$$

for θ_u^- and θ_s^+ defined as in (4.22).

To determine if a particular value of ω satisfies this condition, we employ a shooting method, solving (4.21) by integrating forward in z with initial condition $\theta_0 = \theta_u^-$ and \hat{u} given by the solutions to the BVP discussed in §8.

For each candidate value of ω , we consider $\theta_f(\omega)$, always initializing at $\theta_0 = \theta_u^-$. The final value of $\theta(z)$ can be thought of as the angle “accumulated” over the course of the trajectory. A jump of size π in the accumulated angle indicates that the corresponding ω value is an eigenvalue, as such a jump can only be achieved if θ_f has moved from θ_u^+ to $\theta_u^+ + \pi$, passing through θ_s^+ or $\theta_s^+ + \pi$ in the process and therefore satisfying condition (4.27). The jump we find for each solution for the parameter ranges indicated in figure 6 is never larger than $\Delta\theta = \pi$. An application of Sturm-Liouville theory tells us that, for each solution, this eigenvalue is the first in a string of eigenvalues ordered $\omega_0 > \omega_1 > \dots > -\infty$ and, therefore, the largest.

Finally, we use a root finding algorithm to identify the exact values of ω at which these jumps occur. Examining the largest eigenvalue as a function of the wave speed (alternatively, the phase) for solutions associated with that wave speed (phase) gives us a curve with a clear minimum: see figure 4.8. The solution characterized by this minimum is the most stable, and therefore preferred, solution.

Note that both eigenvalue curves are essentially inverted parabolas, with ω only approaching 0 as γ and c approach the limits of their respective ranges. This occurs for the limiting cases of $c = \hat{c} + \beta$ and $c = \hat{c} + \alpha$, either end of the range of allowable speeds found in §4.5. It is only for these limiting cases that an eigenvalue exists at or very near zero: for all other allowable wave speeds, there is no zero eigenvalue and therefore no translational invariance.

For the phase space trajectories corresponding to both limiting situations and the preferred case, as well as the distance between the fireline and wind switch in each case, see figure 4.9. For wind speeds near the ends of the allowable range, the wind switch occurs very close to $z = \pm\infty$ and far away from the fireline. The preferred solution corresponds to a wave speed of $c = -0.08995$. The unique wave speed found for solutions to the constant wind speed system is $c = -0.084153$, meaning that inclusion of a wind switch induces a

speed-up of the front.

Notably, for the preferred solution, the wind switch is closer to the fireline than either of the limiting cases as well as being spatially “ahead.” Specifically, if we compute the signed distance between the u value of the wind switch and that of the fireline as $\mathbf{d} = u_{windswitch} - u_{fireline}$, we find $\mathbf{d} = 0.58459$ for the preferred wave speed (as illustrated in image (c) in figure 4.9). We parameterized the front solutions so that $z = 0$ corresponds to the fireline. Therefore $\mathbf{d} > 0$ means that, for the preferred solution, the wind switch occurs ahead of the fireline in a manner consistent with the physics of air entrainment.

4.8 Conclusion

Understanding the effects of changes in local environmental variables, such as wind, on the spatial structure of a propagating fireline is key to better understanding fire behavior more generally. Mathematically, the existence and stability of traveling wave solutions in a system with spatial discontinuities, such as those imposed by the wind switch studied here, is an intriguing extension to classical theory. In this chapter, we explored the effects of an external forcing term describing the fire-induced wind on the existence of profiles in the temperature representing fire fronts and their resilience to spatial perturbations.

Traveling wave solutions are heteroclinic connections between fixed points of the corresponding system—in this case, in \mathbb{R}^2 . As such, problems concerning their existence and stability lend themselves well to geometric dynamical systems approaches. We extended the classical existence argument involving the coincidence of invariant manifolds to a spatially discontinuous system, in which existence must be demonstrated through the intersection of invariant manifolds because of the difference between the systems at $\pm\infty$.

We found that intersections, and therefore solutions, exist only for a bounded continuum of wave speeds. Moreover, the interval of wave speeds for which solutions exist is dependent on the relative magnitude of the wind speed before and after the point of discontinuity. The relationship between the wind speed parameters also determines which of two qualitatively different categories the intersection falls in to: type 1 or type 2. This classification is tied to the stability of the fronts and allows us to filter out those wind configurations corresponding to unstable—and therefore physically nonviable—wind speeds.

As a means of identifying the spectrally preferred front and its speed, we calculated the magnitude of the largest eigenvalue across the range of wave speeds for which stable fronts exist. This led us to three physical conclusions: firstly, the largest eigenvalue is smaller than zero, as ω only approaches zero very near to the endpoint of the allowed range of wave speeds and the preferred speed is near the center of the range. The lack of a zero eigenvalue means that translational invariance is broken, so the fronts are localized in space.

Secondly, the distance between the fireline and the wind switch is relatively close for the preferred solution, with the wind switch occurring ahead of the fireline. Lastly, the spatially discontinuous wind causes the front solution to move with a faster speed than it would in the constant-wind system.

Ultimately, we are able to use the mathematical criteria for existence and stability of front solutions to determine constraints on the physical configuration of the wind field and its spatial relationship to the fireline. We modeled only the temperature of the fire layer and imposed the combined ambient and fire-induced wind as an external forcing. We find that, for the spectrally preferred solution, the wind switch occurs ahead of the fireline. Despite not explicitly modeling the wind field, this key physical takeaway is consistent with the physics of air entrainment seen in fires at all scales.

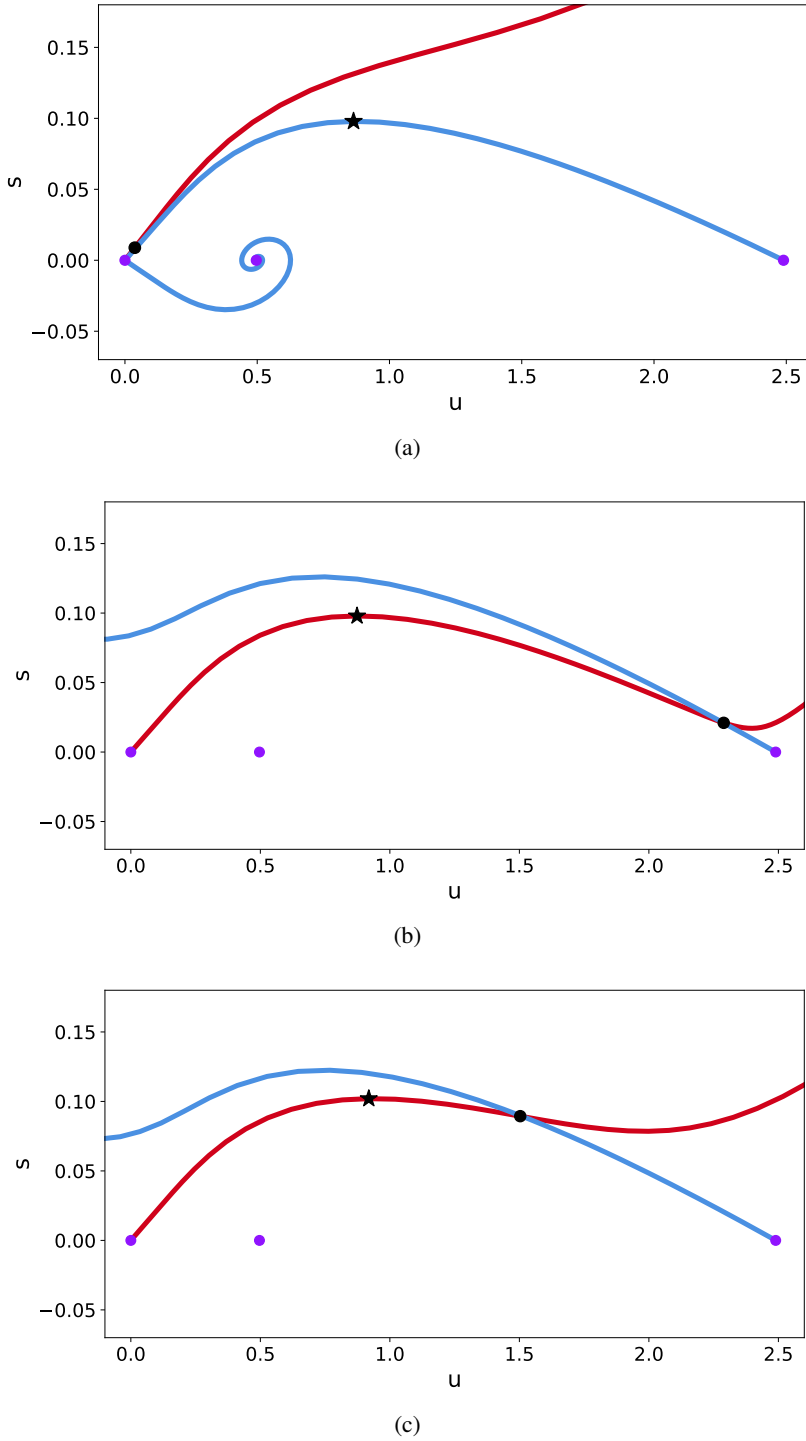


Figure 4.9: Intersecting invariant manifolds for two wave speeds on either end of the allowed range as well as the preferred wave speed. The fireline occurs at the maximum value of s along the portion of the trajectory corresponding to the solution and is indicated by the black star. The wind switch occurs at the point of intersection of the manifolds and is indicated by the black dot. All intersections are type 1. (a) shows the intersection when c is very close to $\hat{c} + \beta$. The signed distance between the fireline and the wind switch is $\mathbf{d} = -0.82683$. (b) shows the intersection when c is very close to $\hat{c} + \alpha$, with $\mathbf{d} = 1.41559$. (c) shows the intersection for the preferred wave speed, $c = -0.08995$, with $\mathbf{d} = 0.58459$.

CHAPTER 5

Transverse wind variation in the reduced system

5.1 Introduction

In this chapter, we continue to consider the reduced system described in Chapter 3 for the temperature $u(z, y, t)$ of a burning region of homogeneous fuel, described in moving coordinates:

$$\frac{\partial u}{\partial t} = \nabla^2 u + (c - w_z(z))u_z - w_y(y)u_y + f(u, v^*) \quad (5.1)$$

Recall that stationary solutions in the moving frame satisfy:

$$0 = u_{zz} + u_{yy} + (c - w_z(z))u_z - w_y(y)u_y + f(u, v^*) \quad (5.2)$$

with the front solutions considered in Chapter 4 satisfying the additional condition that $u_y = 0$.

Our goal is to determine if a transverse perturbation in the form of a nonhomogeneous wind term is sufficient to induce instability in the system. Such instability would result in spatial patterning of the front solutions in the transverse direction, normal to the direction of motion of the propagating front. We will use many of the tools first employed in Chapter 4 to consider the effects of a spatially dependent wind—this time with transverse variation—on the stability and spatial structure of solutions to (5.2). In essence, we ask whether a spatially patterned external forcing term causes spatial patterning in solutions that are, at equilibrium, constant in space. This is not the same as asking whether the system's inherent nonlinearity gives rise to instability. The use of a spatially structured wind term is, however, well motivated by the underlying physics of the problem.

Our main result for the transverse problem is the development of two methods by which one may calculate regions of transverse instability: the second method allows us to pinpoint ranges of the parameters controlling the shape of the transverse wind term that result in instability. In light of these transverse stability results we are able to obtain further information about the stability of the full, two-dimensional system. Our primary

result in the two-dimensional case allows us to identify parameter regimes for the streamwise and transverse wind resulting in overall instability and study the form of the resulting eigenfunctions.

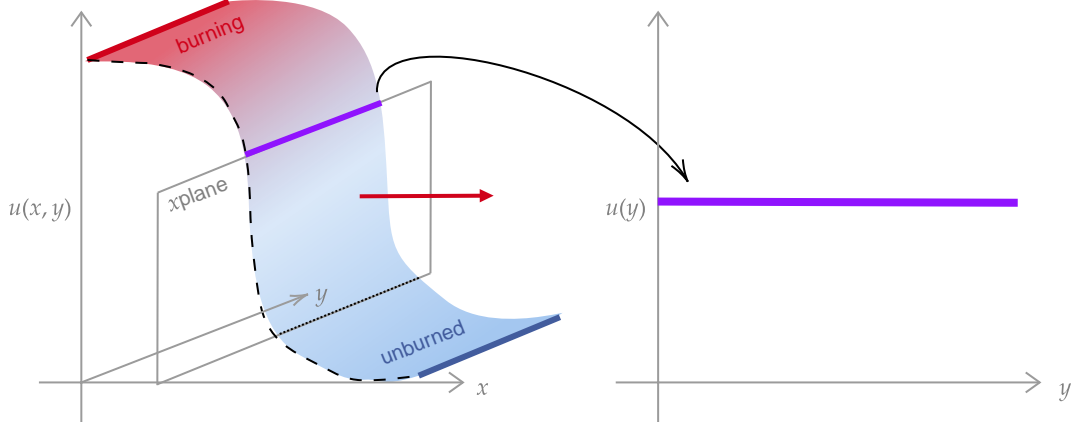


Figure 5.1: For an unperturbed system the front solutions studied in this chapter, indicated in purple, may be thought of as the result of taking the intersection of constant x planes with the two-dimensional front depicted in red and blue. As a function $u(y)$, the resulting solutions are constant. Recall that the profile solutions studied in Chapter 3 correspond to the dashed black line. For perturbations to which the system is unstable, we expect emergent transverse structure.

5.2 Motivating and constructing the spatially dependent wind

The motivation for imposing a wind term dependent on the transverse variable comes from a widely observed pattern formation phenomenon known as “towers and troughs” in the fire science community. This idea refers to the pattern of counter-rotational vortices that emerge along the length of the fireline in what we refer to as the transverse direction in this work. These counter-rotational vortices result in a pattern of updrafts and downdrafts in the z direction that alternatively push up hot air and entrain cool air. The resulting gaps in the fireline, between each “tower” and “trough,” allow for convective transfer of heat from the burning fuel to the unburned fuel ahead of the fireline. As a result, the towers and troughs phenomenon is a key mechanism contributing to fire spread. This phenomenon is observed in fires across a range of scales as well as in computational simulations. For details, see [15], [48] and [16].

To capture the vertical pattern of updrafts and downdrafts in a one-dimensional setting, we consider only the components of the velocity acting in the transverse direction. The result is a wind field that “switches” in space, similar to the wind field studied in Chapter 4. We model this behavior with a tanh function whose

slope and magnitude are controlled by the parameters α_y, β_y :

$$w_y(y) = \alpha_y \tanh(\beta_y y) \quad (5.3)$$

We are motivated to use a continuous function (as opposed to a piecewise continuous function, as in Chapter 4) for two reasons: firstly, the smooth nature of the switch between values of negative and positive α given by (5.3) reflects reality more accurately than a step function. Secondly, the fact that equilibrium solutions do not have transverse spatial structure means that we can use a more spatially complex wind term without running into the complications regarding the existence of solutions that we encountered in the streamwise case. The symmetry of the wind term does not take in to account the varying magnitude of fire-induced wind on the windward or leeward side of an advancing fireline, but its simplicity allows us to further our analysis.

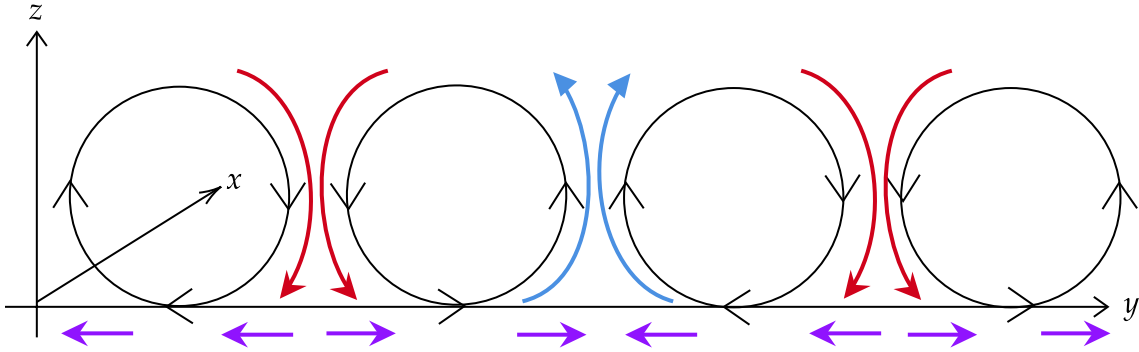


Figure 5.2: A schematic of the counter-rotational vortices along the fireline in the streamwise direction. The pattern of updrafts and downdrafts in the z direction is indicated by the blue and red arrows. The projection of the two-dimensional field on to the y axis is indicated by the purple arrows, illustrating the switching behavior in the transverse direction.

5.3 The transverse eigenvalue problem

To understand the stability of transverse front solutions we turn to the secondary eigenvalue problem (5.5) originally described in Chapter 3, resulting from separating variables in the two-dimensional eigenvalue problem. Our primary goal is to understand the effect of spatially dependent wind configurations that vary in the transverse direction on the stability of solutions to (5.1). Recall that the eigenvalue problem in linearized coordinates $p(z, y)$ resulting from the linearization of (5.1) about a two-dimensional front solution $\hat{u}(z, y)$ is

$$\lambda p = \frac{\partial^2 p}{\partial z^2} + \frac{\partial^2 p}{\partial y^2} + (c - w_z(z)) \frac{\partial p}{\partial z} + w_y(y) \frac{\partial p}{\partial y} + f'(\hat{u})p \quad (5.4)$$

Separating variables by taking $p(z,y) = q(z)\eta(y)$, we obtain

$$\frac{d^2\eta}{dy^2} + w_y(y)\frac{d\eta}{dy} = \mu\eta \quad (5.5)$$

as our transverse eigenvalue problem, where μ is the transverse spectral parameter.

We use an integrating factor argument to rewrite (5.5) without any terms involving the first derivative. We accomplish this by making the change of variables $\rho(y) = g(y)\eta(y)$ for $\eta(y)$ as in (5.5) and $g(y)$ as of yet undetermined. We expect for $\rho(y)$ to satisfy an equation of the form

$$\rho''(y) + \gamma(y)\rho(y) = \mu\rho(y) \quad (5.6)$$

where μ is the transverse eigenvalue (alternatively, the wave number in the transverse direction). Making the above change of variables, our eigenvalue problem becomes

$$g\eta'' + gw_y(y)\eta' = \mu\eta g \quad (5.7)$$

The right hand side of (5.7) already matches the right hand side of our desired form, (5.6). We would like for the left hand side to match as well, meaning we require

$$\rho'' + \gamma(y)\rho = g\eta'' + gw_y(y)\eta' \quad (5.8)$$

Expanding the left hand side, we obtain:

$$(g\eta)'' + \gamma(y)g\eta = g''\eta + 2g'\eta' + g\eta'' + \gamma(y)g\eta \quad (5.9)$$

We would like for the right hand side to be identically equal to $g\eta'' + gw_y(y)\eta$. To that end, we pick $\gamma(y)$ to cancel the $g''\eta$ and $\gamma(y)g\eta$ terms and pick g to match the $2g'\eta'$ and $gw_y(y)\eta'$ terms. This gives us two equations to solve:

$$g''\eta = -\gamma(y)g \quad (5.10)$$

and

$$2g'\eta' = gw_y(y)\eta' \quad (5.11)$$

Solving (5.11), we obtain

$$g(y) = c \exp \left[\frac{1}{2} \int_0^y w_y(s) ds \right] \quad (5.12)$$

and substituting this result in to (5.10) gives us

$$\gamma(y) = -\frac{c}{2} w'_y(y) - \frac{c^2}{4} w_y^2(y) = \frac{\alpha\beta}{2} \operatorname{sech}^2(\beta y) - \frac{\alpha^2}{4} \tanh^2(\beta y) \quad (5.13)$$

Note that the choice of c would require boundary conditions on the integrating factor $g(y)$: without loss of generality, we pick $c = 1$. Any other choice would simply shift the upcoming analysis by some constant multiple. This choice of integrating factor and potential function allows us rewrite (5.5) as a Schrödinger equation of the form (5.6).

We can convert this in to a first order system in u and v . In matrix form, this is

$$\begin{pmatrix} u \\ v \end{pmatrix}' = \begin{pmatrix} 0 & 1 \\ \mu - \gamma & 0 \end{pmatrix} \begin{pmatrix} u \\ v \end{pmatrix} = \mathcal{L}^y \begin{pmatrix} u \\ v \end{pmatrix} \quad (5.14)$$

We consider the effects of letting $y \rightarrow \pm\infty$ to obtain

$$\mathcal{L}_{\pm\infty}^y = \begin{pmatrix} 0 & 1 \\ \mu + \frac{\alpha^2}{4} & 0 \end{pmatrix} \quad (5.15)$$

with eigenvalues $\lambda_{\pm} = \pm \sqrt{\mu + \frac{\alpha^2}{4}}$. As in the constant wind case, the boundary of the essential spectrum of \mathcal{L}^y is given by the eigenvalues of $\mathcal{L}_{\pm\infty}^y$. The essential spectrum corresponds to oscillatory solutions at $\pm\infty$ as opposed to those that exponentially grow or decay. The operator associated to (5.6) is self-adjoint, so we expect our point spectrum to be entirely real, meaning we must have $\mu \geq \frac{\alpha^2}{4}$. Recalling our discussion of oscillation theory in Chapter 2, we know that the values of μ that satisfy this condition are also eigenvalues if a heteroclinic connection is made between the fixed points at $\pm\infty$. Moreover, Sturm-Liouville theory tells us that the eigenvalues of (5.6) are indexed and the n^{th} eigenvalue is associated to the eigenfunction with $n - 1$ zeros. Therefore, we are motivated to consider the case when $\mu = 0$ and use the tools of Chapter 2 to determine whether 0 is the largest eigenvalue or whether additional, positive eigenvalues exist.

5.4 The accumulated angle

As in Chapter 4, we will calculate the accumulated angle for a range of α_y and β_y values to get a sense of the indexing of the eigenvalue at 0. We convert to polar coordinates in phase space (the Prüfer variables defined in Chapter 2) to obtain

$$\begin{aligned}\dot{r} &= r \cos(\theta) \sin(\theta)(1 + \mu - \gamma) \\ \dot{\theta} &= (\mu - \gamma) \cos^2(\theta) - \sin^2(\theta)\end{aligned}\tag{5.16}$$

We begin by noting that the equation for θ is decoupled from that for r in (5.16), so it suffices to only consider solutions to the second equation

$$\dot{\theta} = (\mu - \gamma(y; \alpha_y, \beta_y)) \cos^2(\theta) - \sin^2(\theta)\tag{5.17}$$

We compactify (5.17) by making the change of variables $y \rightarrow \sigma$, where $\sigma = \tanh(\beta_y y)$, mapping us from $y \in (-\infty, \infty)$ to $\sigma \in [-1, 1]$. Denoting differentiation with respect to y by $'$, this results in the system

$$\begin{aligned}\sigma' &= \beta_y(1 - \sigma^2) \\ \theta' &= (\mu - \gamma(\sigma; \alpha_y, \beta_y)) \cos^2(\theta) - \sin^2(\theta)\end{aligned}\tag{5.18}$$

where

$$\gamma(\sigma; \alpha_y, \beta_y) = \frac{\alpha_y \beta_y}{2}(1 - \sigma^2) - \frac{\alpha_y^2}{4}\sigma^2\tag{5.19}$$

Eigenvalues are values of μ for which solution trajectories to (5.18) exist satisfying appropriate boundary conditions at $\pm\infty$. To determine these conditions, we note that σ is always in the range $[-1, 1]$ (or $[1, -1]$ if $\beta_y < 0$). By taking the limit as $y \rightarrow \pm\infty$ in the equation for θ' in (5.18), we see that $\theta_{\pm} = \theta(\rightarrow \pm\infty) = \arctan\left(\pm \sqrt{\mu + \frac{\alpha_y^2}{4}}\right)$.

A key point is that both angles θ_{\pm} are both left-hand and right-hand boundary conditions, and it is not immediately clear which angle ought to correspond to θ_0 and which to θ_f . In practice, we pick the correct θ_0 and θ_f based on the choice for which the fixed points at $\pm\infty$ are hyperbolic. As a result, we have

$\theta_0 = \arctan\left(-\sqrt{\mu + \frac{\alpha_y^2}{4}}\right)$ and $\theta_f = \arctan\left(\sqrt{\mu + \frac{\alpha_y^2}{4}}\right)$ and we find the following eigenvalue condition:

$$\Delta\theta = \theta_f - \theta_0 = 2\arctan\left(\sqrt{\mu + \frac{\alpha_y^2}{4}}\right) \text{ if } \mu \text{ is an eigenvalue} \quad (5.20)$$

$\Delta\theta = 0 \bmod \pi$ if μ is not an eigenvalue

As outlined in Chapter 2, we may use the accumulated angle $\Delta\theta = \theta_f - \theta_0$ to determine whether or not some value of μ is an eigenvalue as well as how it is indexed in comparison to other eigenvalues. In particular, if we find that $\Delta\theta(\mu = 0) = 2n\arctan\left(\sqrt{0 + \frac{\alpha_y^2}{4}}\right)$ for some range of the parameter value α_y , we may conclude that there are n eigenvalues greater than 0. In practice, the accumulated angle may only meet the condition given in (5.20) for an instantaneous coupling of parameter values. For all other values, it will be some multiple of π . This is the key to reading accumulated angle diagrams: we look for jumps of magnitude π to indicate that $\mu = 0$ was, briefly, an eigenvalue before moving in to the right half-plane. Thereafter, a positive eigenvalue exists. To calculate the accumulated angle for various values of α_y and β_y , we integrate forward in “time” from the initial condition (θ_0, σ_0) , where

$$\theta_0 = \lim_{y \rightarrow -\infty} \theta(\sigma(y)) = \arctan\left(\pm \sqrt{\mu + \frac{\alpha_y^2}{4}}\right) \quad (5.21)$$

$$\sigma_0 = \pm 1$$

Again, the choice of positive or negative branch in the definition of θ_0 and ± 1 in the definition of σ_0 depends on the sign of the parameters α_y, β_y and is picked so that the fixed point at $-\infty$ is a saddle. In practice, we may choose to only consider $\beta_y > 0$ because the parity of the wind function means that considering $\pm\alpha_y$ covers all potential forms of the wind term. This is reflected in the bilateral symmetry of the accumulated angle contour plots in figure 5.4. Results for the accumulated angle are depicted in figure 5.3 for $\beta_y = 1$ and a range of α_y values and figure 5.4 for a range of α_y and β_y values. Jumps in the accumulated angle $\Delta\theta$ of magnitude π indicate that the θ trajectory has moved from 0 through the value given in the eigenvalue condition (5.20). The implication is that, for the α_y, β_y pair where the jump occurs, $\mu = 0$ was momentarily an eigenvalue, meaning that an eigenvalue of (5.1) has moved from the left half-plane, through the origin and in to the right half-plane.

We observe a clear region of (α_y, β_y) pairs for which a positive eigenvalue should therefore exist, indicated

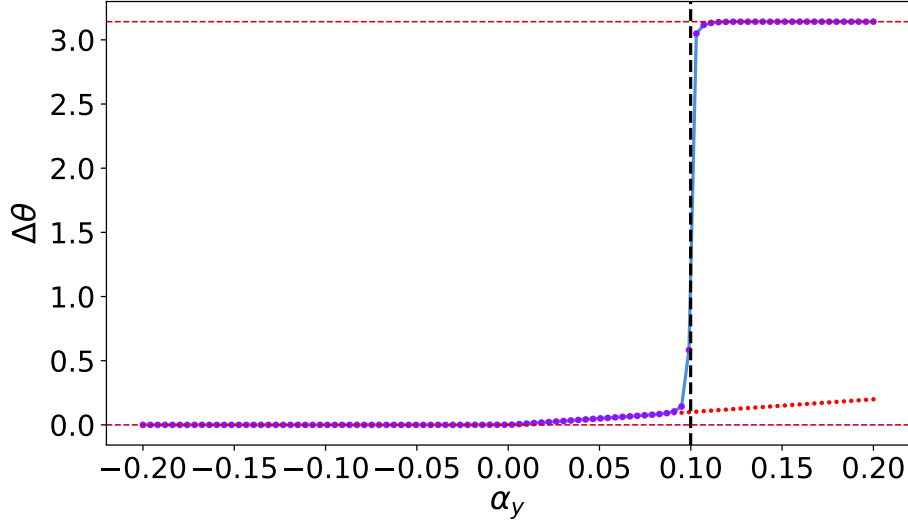


Figure 5.3: The accumulated angle for fixed $\beta_y = 1$ and a range of α_y values, zoomed in near $\alpha_y = 0$ to focus on the region of the jump. The dashed black line indicates the α_y value of the initial jump, at about 0.1. The dashed red lines are at $y = 0, \pi$ and the dotted red curve indicates the eigenvalue condition (5.20), which varies as a function of α_y . Note that the accumulated angle tracks this condition before jumping.

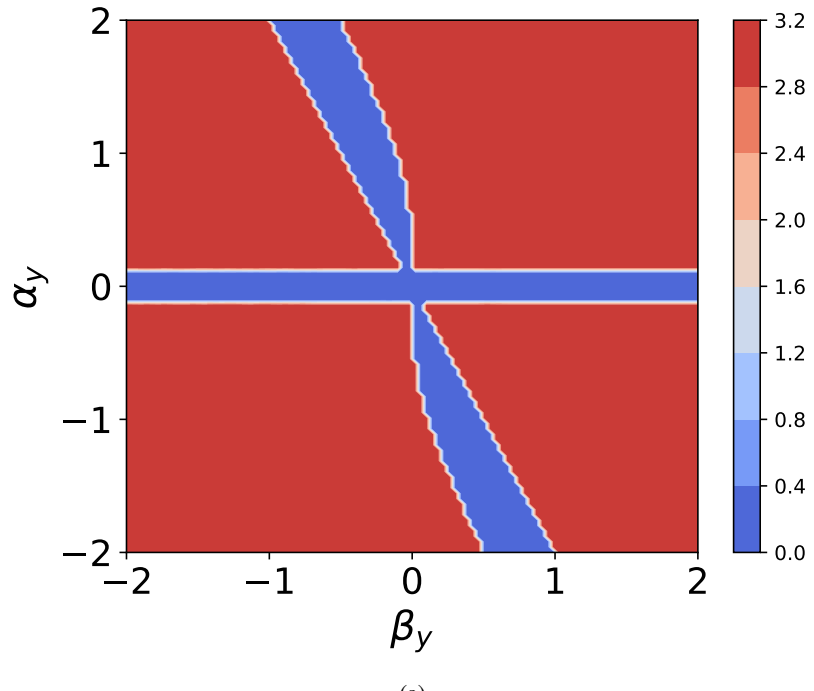
by the red region in figure 5.4.

5.5 Finding positive transverse eigenvalues and corresponding eigenfunctions

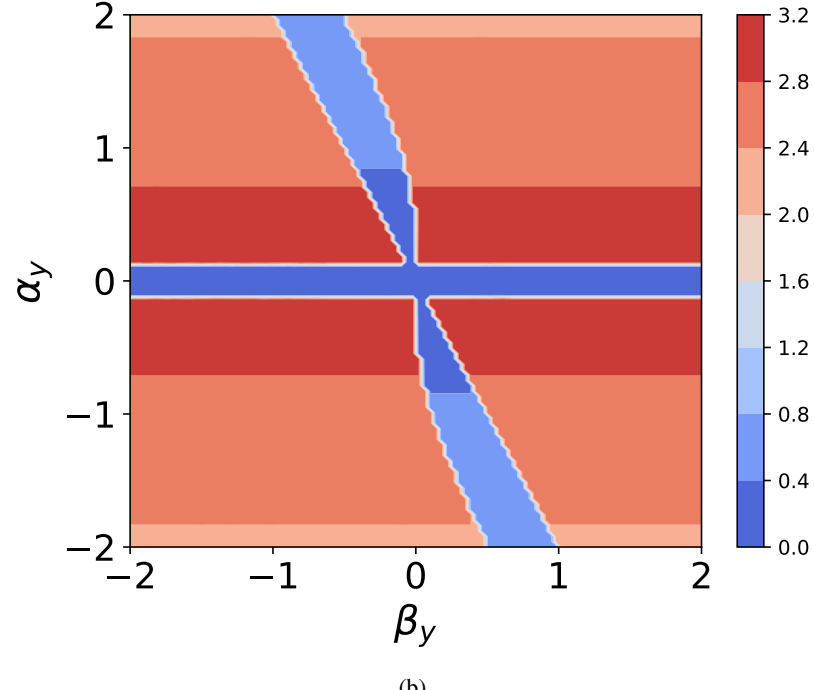
The results of the previous section give us a means to identify parameter ranges where we might expect positive eigenvalues. To actually find these eigenvalues, we frame (5.5) as a boundary value problem with the eigenvalue μ as an additional degree of freedom. Our problem becomes:

$$\begin{aligned} \eta' &= \xi \\ \xi' &= (\mu - w_y(y))\xi \end{aligned} \tag{5.22}$$

for $w_y(y)$ as in (5.3) and zero boundary conditions at $\pm\infty$. A third boundary condition is necessary because of the free parameter μ and is chosen so that the derivative is nonzero at one endpoint to prevent trivial solutions. In practice, we take boundary conditions at $\pm L$, where L is chosen to be large enough so as to approximate numerical infinity. We calculate the solution and the value of μ using SciPy's `SOLVE_BVP` for the same range of (α_y, β_y) and the same resolution as in the accumulated angle calculations from the previous section. This allows us to identify parameter regions for which positive eigenvalues exist and we may expect instability with respect to transverse perturbations. Our results are depicted in figure 5.5.



(a)



(b)

Figure 5.4: A contour plot of the accumulated angle $\Delta\theta$ as a function of α_y and β_y . Solid red indicates an accumulated angle of π and, therefore, parameter regions for which a positive eigenvalue exists. (b) is a contour plot of θ_f and demonstrates the gradient of changes in the angle as a function of the parameter values. Note the symmetry with respect to the line $\alpha_y = -\beta_y$, which is to be expected because of the parity of the tanh function used to define the wind.

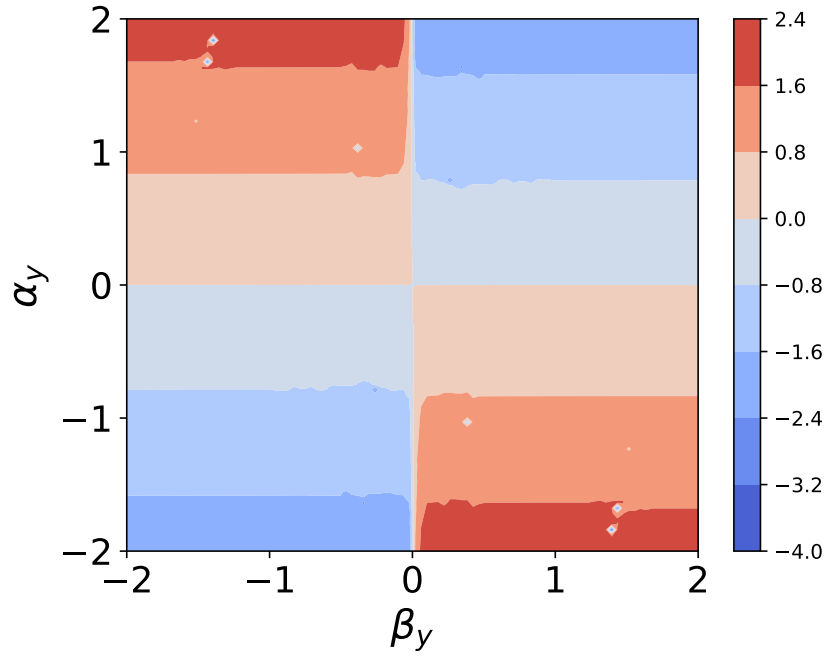


Figure 5.5: Eigenvalues found using the method described in §4.6 for $\alpha_y \in [-2, 2]$ and $\beta_y \in [-2, 2]$. The largest positive eigenvalue for this range of parameters, rounded to four decimal places, is $\mu_{max} = 1.9965$ and occurs for $\alpha_y = -2.0$, $\beta_y = 1.5556$.

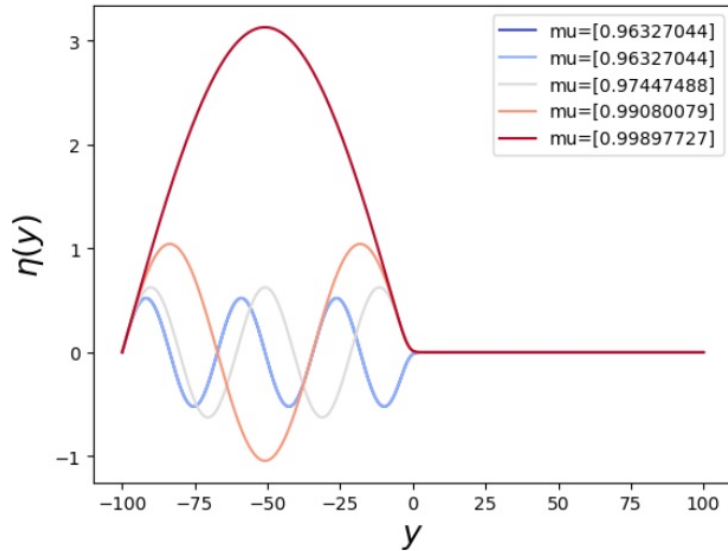


Figure 5.6: Transverse eigenfunctions $\eta(y)$ for $\alpha_y = 1$ and $\beta_y = -0.5$ with a range of guesses for the eigenvalue parameter μ . The eigenvalue corresponding to each eigenfunction is listed in the legend. The eigenfunction with no zeros corresponds to the largest eigenvalue, as expected.

5.6 Comparing streamwise and transverse eigenvalues

Of course, the interesting result is not just transverse instability but spectral instability of the full, two-dimensional solution. In the case of spatially dependent streamwise wind, we demonstrated in Chapter 4 that stable solutions all have a largest eigenvalue $\omega_{max} < 0$. Further, we have the relation

$$\lambda = \omega + \mu \quad (5.23)$$

To understand the (in)stability of solutions to the full, two-dimensional problem to perturbations imposed via a spatially varying wind term, we need to understand how to characterize wind configurations for which the transverse eigenvalue μ is large and positive enough to overcome the negative streamwise eigenvalue ω , resulting in $\lambda > 0$ and spectral instability of solutions to (5.1).

Recall that our streamwise wind was defined in Chapter 4 as

$$w(z) = \begin{cases} \alpha_x & z < 0 \\ 0 & z = 0 \\ \beta_x & z > 0 \end{cases} \quad (5.24)$$

where we have included the x subscript to distinguish between the streamwise parameters α_x, β_x and the transverse parameters α_y, β_y . Using the results from this section and the methods described in Chapter 4, we may identify parameter regimes for which positive λ exists, indicating spectral instability of the original system (5.4). Our results demonstrate that, when $\beta_y > 0$, as the magnitude of the streamwise wind grows, so does its stabilizing effect. However, for smaller values of $\alpha_x (< 0.2)$, the instability introduced by the transverse wind variation dominates for all α_y magnitudes. The opposite is true for $\beta_y < 0$. These results are summarized in figure 5.7. Note that throughout the figures in this chapter, red indicates positive eigenvalues (and therefore regions of spectral instability) whereas blue indicates negative eigenvalues (and therefore regions of spectral stability).

5.7 Two-dimensional eigenfunctions

Finally, we seek to visualize the two-dimensional eigenfunctions $p(z,y)$ that are solutions to (5.4) with eigenvalue $\lambda = \mu + \omega > 0$. These may be found as the product of the streamwise and transverse eigenfunctions, $q(z)$ and $\eta(y)$. The transverse eigenfunctions were found, along with the eigenvalues, in §5.5.

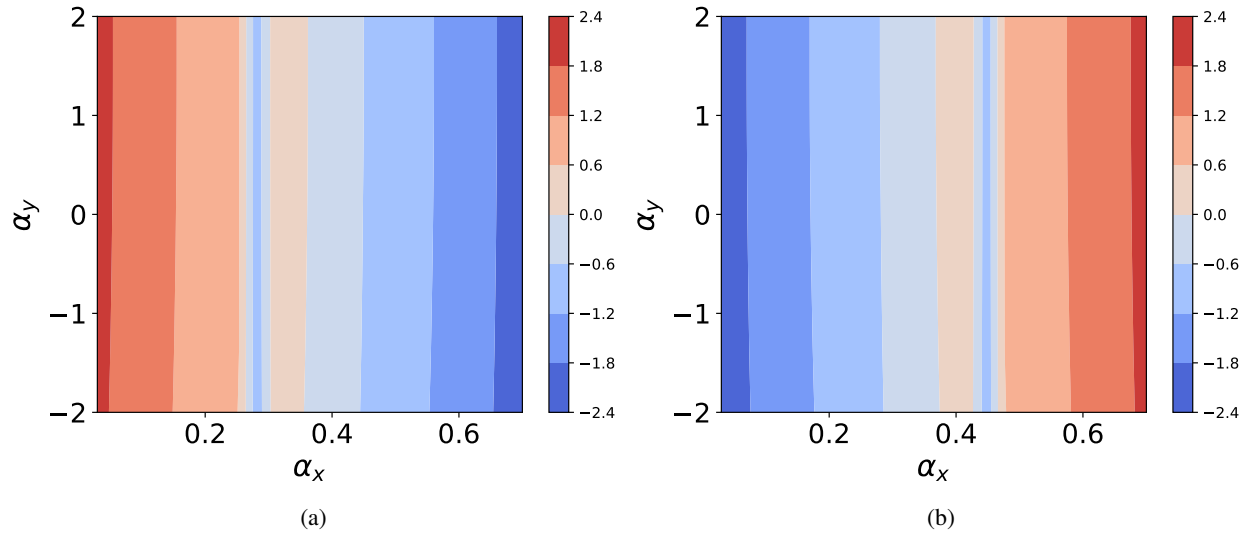


Figure 5.7: Regions of positive and negative values of the eigenvalue λ of the two dimensional problem, found as the sum of the transverse and streamwise eigenvalues $\lambda = \mu + \omega$ for $\alpha_y \in [-2, 2]$ and (a) $\beta_y = 0.5$ and $\alpha_x = \alpha_y \in [.03, .7]$ and (b) $\beta_y = -0.5$ and $\alpha_x \in [.03, .7]$.

To gain intuition about the streamwise eigenfunction, we begin by considering the case when $\mu = 0$ in the streamwise eigenvalue problem resulting from the separation of variables

$$\frac{d^2q}{dz^2} + (c - w_z(z)) \frac{dq}{dz} + f'(\hat{u}))q = (\lambda - \mu)q = \omega q \quad (5.25)$$

Note that a zero eigenvalue only exists for a wind term without a wind switch, and so this discussion is only to provide a means of checking our results for a spatially dependent wind. Taking $q(z) = \hat{u}'(z)$, we have

$$\omega \hat{u}'(z) = \lambda \hat{u}'(z) = (\hat{u}'(z))'' + (c - w_x) \hat{u}'(z) + (v^* r'(\hat{u}(z))) \hat{u}'(z) - l \hat{u}'(z) \quad (5.26)$$

The right hand side of (5.26), interpreted as an operator \mathcal{L} acting on $\hat{u}'(z)$, is identical to the right hand side of (5.1), where the operator is instead acting on $u(z)$. So, we conclude that $\lambda = \omega = 0$ is an eigenvalue of the operator

$$\mathcal{L} = \left[\frac{\partial^2}{z^2} + (c - w_x) \frac{\partial}{\partial z} + (v^* r'(\hat{u}) - l) \right] \quad (5.27)$$

with eigenfunction $\hat{u}'(z)$. It follows that, if $\mu \neq 0$, then $\omega = \lambda - \mu = 0$ is an eigenvalue of the same operator. This is in line with the results of Chapter 4, in which we concluded that $\omega = 0$ is an eigenvalue of the system with constant wind. As a consequence, if $\mu > 0$, then $\lambda = \mu > 0$ is an eigenvalue of the “primary” eigenvalue

problem (5.4) with constant streamwise wind and corresponding eigenfunction

$$p(z,y) = \hat{u}'(z)\eta(y) \quad (5.28)$$

Figure 5.8 shows the eigenfunction associated with constant streamwise and transverse wind, resulting in a zero streamwise eigenvalue and a negative transverse eigenvalue. We highlight the localization of the eigenfunction in the presence of perturbations by comparing the constant wind case to the lowest-order harmonic when the wind has spatial dependence in both the streamwise and transverse directions.

We find the streamwise eigenfunction in the constant wind case by solving for r in the angular version of the system (see Chapter 4) and constructing a θ trajectory that satisfies the eigenvalue condition laid out in that chapter before converting back to Cartesian coordinates. The resulting spatially patterned eigenfunctions are visualized in figure 5.9. The eigenfunctions depict the local behavior in the vicinity of a front of the linearized system, but this is sufficient to also predict the local (but not global) dynamics of the nonlinear system—see Chapter 2 and [20]. Note that the eigenfunctions essentially demonstrate a pattern of spatially frequency $n = k = 1$ in both directions. A wind term that switched more than once in space (in either or both directions) would result in a pattern with a higher frequency (in the corresponding direction). A higher frequency pattern can also be achieved by considering the higher-order harmonics: the number of zeros of any eigenfunction is given by the indexing of the corresponding eigenvalue, so eigenvalues smaller than μ_{max} will exhibit a larger frequency of oscillation.

5.8 Discussion and conclusions

The thrust of this chapter is that enforcing spatial structure in the spatially-dependent advection term induces spatial structure in the corresponding eigenfunctions in parameter regimes for which the systems exhibits instability. It remains to be seen if this patterning might be observed in systems in which a structured external forcing is not imposed, a point which relates back to the discussion of different mechanisms of instability in Chapter 2. There has been some work, largely due to Carter [39] and Carter and Doelman [38] demonstrating that instabilities may emerge in two-component, singularly perturbed reaction-diffusion models of ecosystems (specifically, competing vegetation) given an appropriate scaling between the ratio of the diffusion coefficients and the advection coefficient. The necessary scaling between diffusion coefficients does not adapt to the fire application for solid fuel, however, and their work does not consider spatial dependence in the advection coefficient.

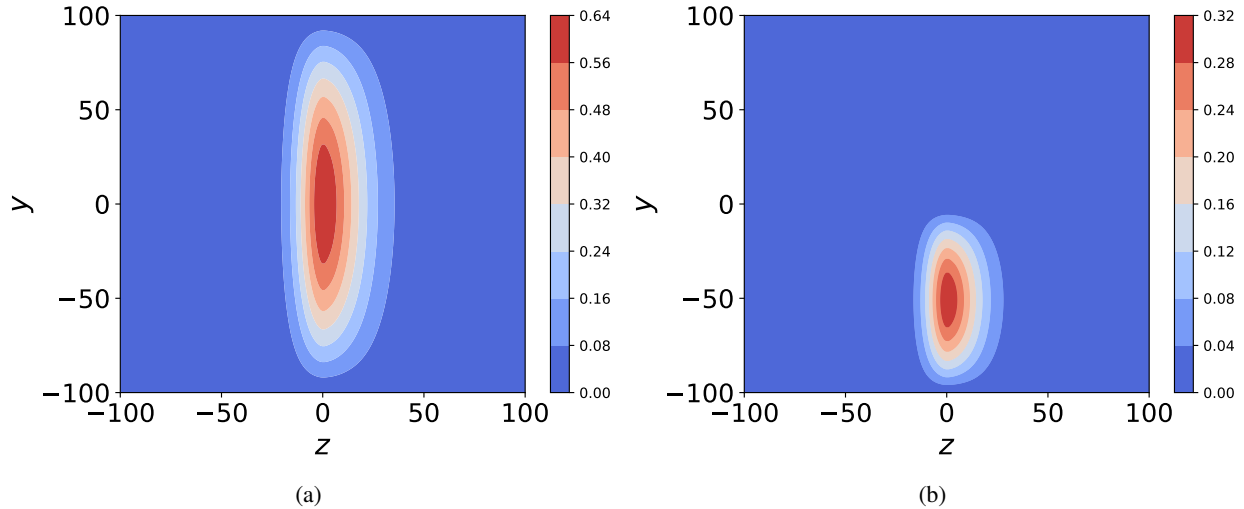


Figure 5.8: Contour plots of the two-dimensional eigenfunctions when (a) both the transverse and streamwise winds are constant in space, resulting in $\lambda = \mu + \omega = -.0002 + 0 < 0$ and (b) both the transverse and streamwise winds switch in space, resulting in $\lambda = \mu + \omega = 0.9989 - 0.0012 > 0$.

The results for the transverse eigenvalue problem presented in this chapter allow us to solidify our understanding of the stability landscape of the full, two-dimensional system with respect to the wind parameters α_x , α_y , and β_y . Physically, we have a better understand of the relative scaling of the fire-induced wind in the streamwise direction and the strength of the transverse “switch” necessary to induce instability in the system and lead to the formation of a spatially patterned state. It is necessary to note that the magnitude of the wind terms used in Chapters 4 and 5, as described by the parameters α_x and α_y , were chosen ad hoc for the analysis in each of those chapters. In future work, these terms should be coupled and the results in figure 5.7 reproduced for a system with this additional physical constraint.

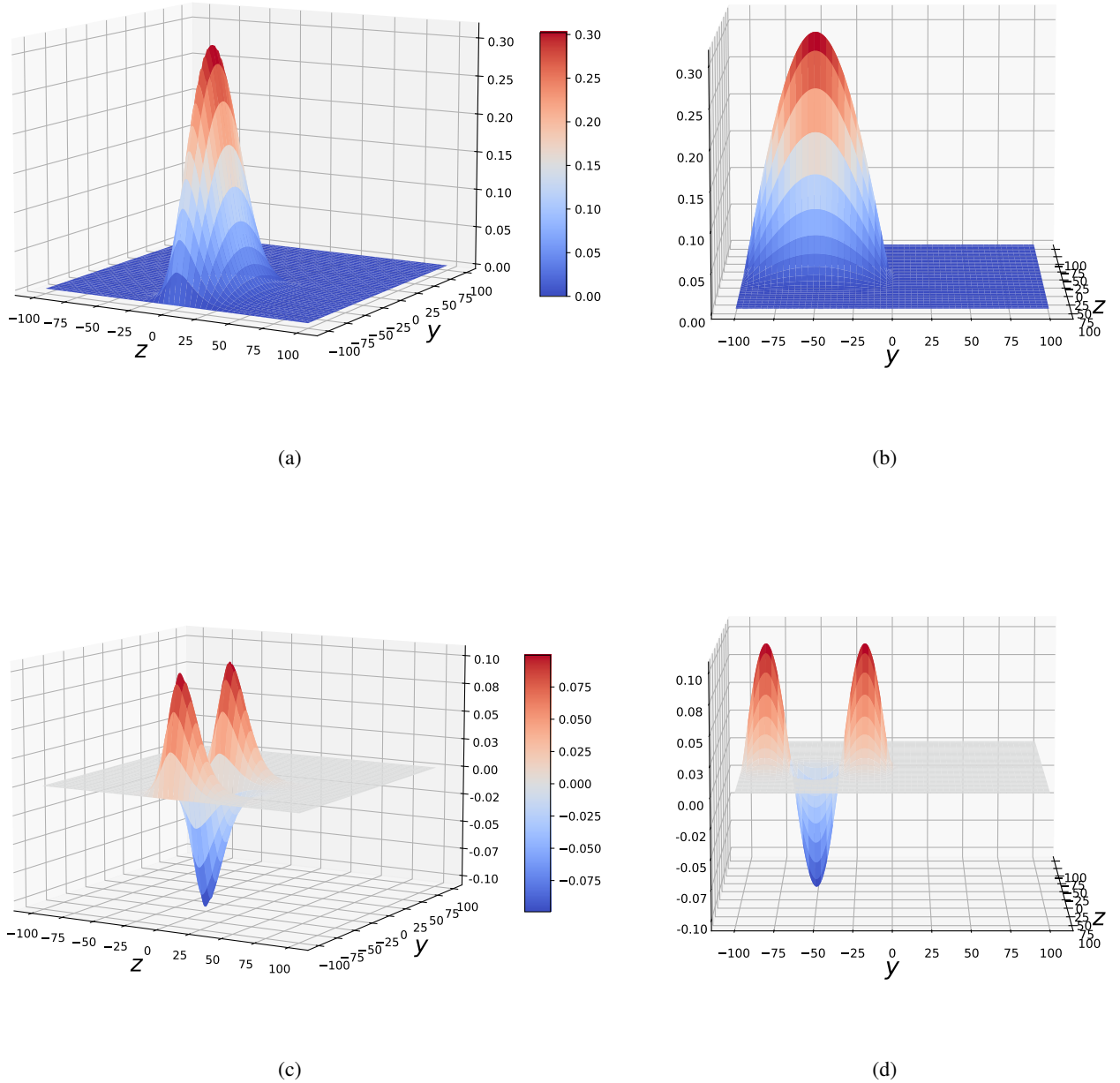


Figure 5.9: The two-dimensional spatial eigenfunction $p(z, y)$, found as the product of the streamwise and transverse eigenfunctions $q(z)$ and $\eta(z)$, for the parameters $\alpha_x = 0.05$, $\alpha_y = 1$, $\beta_y = -0.5$. (a) and (b) depict the eigenfunction for the largest transverse eigenvalue, $\mu = 0.99898$, whereas (c) and (d) depict the higher-order harmonics associated with $\mu = 0.99080$, the second largest eigenvalue.

CHAPTER 6

Emergent instabilities in wind-driven buoyant flow

6.1 Motivation

In this chapter, we take a different view of the pattern formation phenomenon known as “towers and troughs” first described in Chapter 1. Towers and troughs are coherent structures caused by counter-rotational vortices that emerge in the velocity field generated by flaming (as opposed to smoldering) fires. They are characterized by an alternating pattern of updrafts and downdrafts—essentially, localized regions of positive and negative vertical velocity. The gaps created by this pattern in the propagating fireline drive convective heat transfer by allowing heated air to move through the fire line on to unburned fuel. The phenomenon is observed in simulation and practice across a range of scales, from experimental fires to landscape-scale wildfires. For examples, see figure 1.2 and the citations in that chapter.

We test the hypothesis that towers and troughs emerge as the result of thermally driven buoyancy and, therefore, similar spatial patterning should be observable in a system without combustion or fuel consumption. Viewed this way, the emergence of towers and troughs bears a resemblance to the formation of patterns of convective cells in Rayleigh-Bénard convection, in which fluid is heated from below until buoyant effects begin to dominate over viscous effects. In this chapter, we investigate the emergence of instabilities such as those that characterize the towers and troughs pattern in a modified version of the classical system in which Rayleigh-Bénard instabilities are observed.

We consider fluid flow in a semi-infinite channel with a wind velocity in the positive x direction. We model the burning region, the fire line and the preheat region (defined as in Chapter 4) as a hot plate of constant temperature. The hot plate moves with a velocity c_f that we can think of as the rate of spread of the fire. We then consider an x slice of vanishing thickness and move to the Lagrangian viewpoint of moving with the rate of spread of the fire. In the y/z plane we expect to see the formation of counter-rotational vortices. Further, we expect that these vortices will grow in magnitude as we move across the hot plate. We aim to characterize the conditions under which the vortices may be expected to emerge from initially quiescent flow.

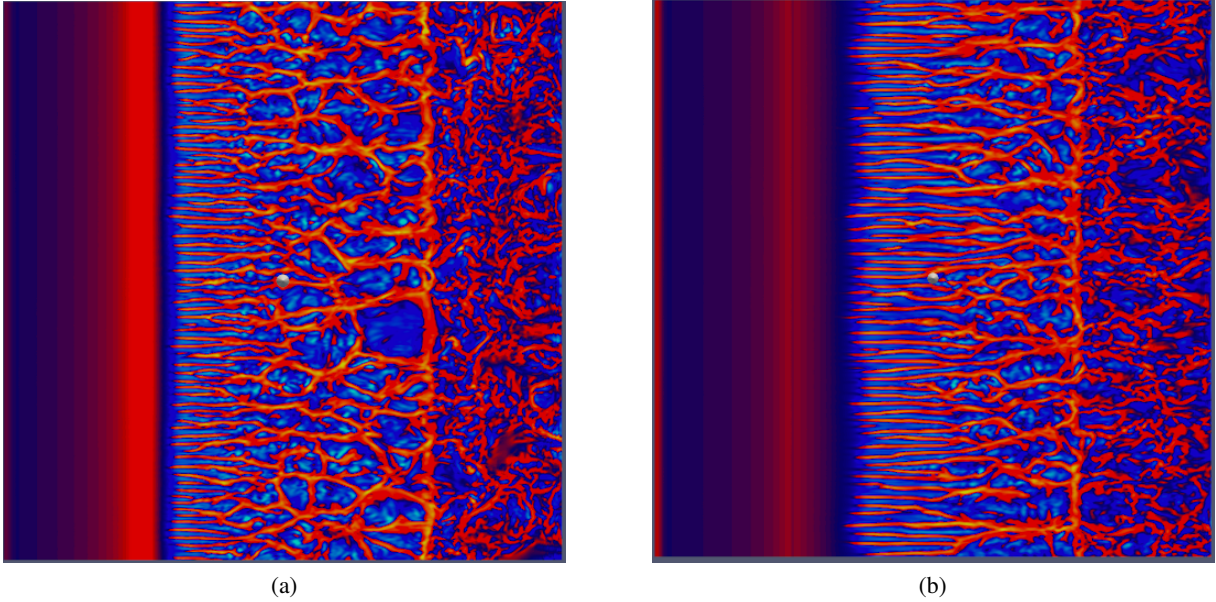


Figure 6.1: Computational fluid dynamics simulations of the vertical velocity w generated by fluid flowing over a constant heat source outputting 775 KW of heat energy in an x/y domain. The imposed wind velocity is (a) 0.3m/s and (b) 0.6m/s. The characteristic pattern of updrafts and downdrafts is visible. The vertical velocity ranges from 1.8m/s (in yellow) to -1.8 m/s (in blue). Simulations conducted by the author using FIRETEC [9].

Our approach follows the general theory of **hydrodynamic stability**, elegantly outlined¹ by S. Chandrasekhar in the first chapter of his text “Hydrodynamic and Hydromagnetic Stability” and paraphrased here [49]. We begin with a hydrodynamic system that is in a stationary state, meaning that none of the variables used to characterize the system are functions of time—this is the “base state” described in 6.3. The system is further defined by a set of parameters X_1, X_2, \dots, X_j . The goal of characterizing the stability of the system is to determine the behavior of solutions to the system when they are subject to small disturbances, or perturbations. If these perturbations decay in time and the system reverts to its initial state, then we say that the system is stable with respect to the perturbations. If, on the other hand, the perturbations grow exponentially and prevent the system from returning to the initial state, the system is unstable with respect to the perturbations.

Any such state depends on the parameters X_1, X_2, \dots, X_j : if all states may be classified as stable or unstable, then there naturally exists some set of parameters corresponding to the threshold state when the system transitions from stability to instability. We refer to this state as being **marginally stable**: when the

¹It is unclear if this aptitude for explanation runs in the family.

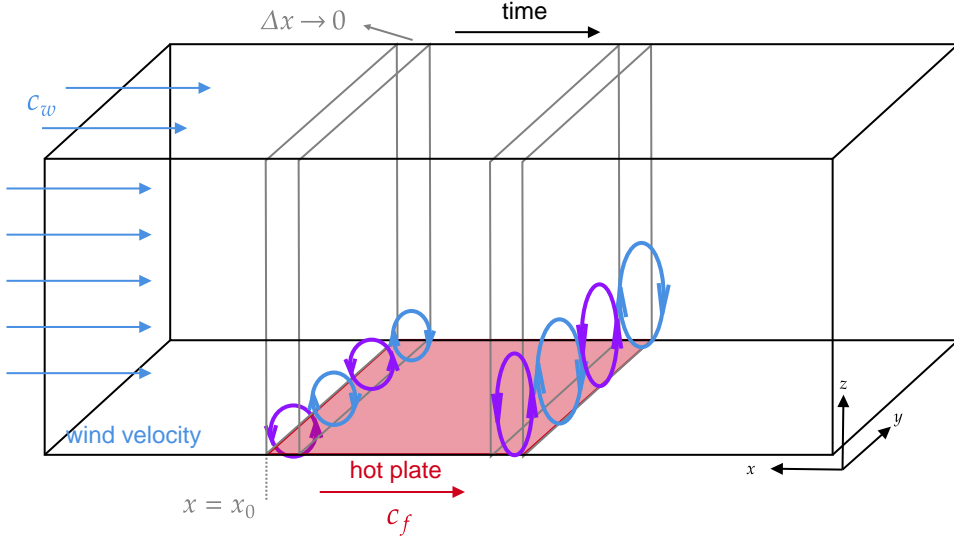


Figure 6.2: The system investigated in this chapter, in which fluid moving with velocity c_w flows over a hot plate moving with velocity c_f . We aim to characterize the conditions under which counter-rotational vortices, indicated in blue and purple, emerge in the velocity field along the length of the hot plate.

system is in this state, the parameters corresponding to the state take on what we call their **critical values**. The process of moving through the marginally stable state is referred to as a **bifurcation** of the system and occurs when the real part of the temporal eigenvalue moves from the left half-plane, through the imaginary axis, and in to the right half-plane.

6.2 Set up and formulation

We model the fire line, the burning region and the pre-heat region as a hot plate held at a constant temperature moving with velocity c_f representing the rate of spread of the fire. Additionally, we consider a wind velocity in the positive x direction denoted c_w , where $c_w \gg c_f$.

A standard analysis of Rayleigh-Bénard convection begins by considering the equations of motion for a heat-conducting viscous fluid acted upon by gravity. These consist of the continuity equation, the Navier-Stokes equations and the equation of energy. Derivations may be found in a number of textbooks, including [50]. The presentation below is due to [51], where the position and velocity vectors are given as Cartesian

tensors, $\vec{x} = x_j$ and $\vec{u} = u_j$ for $j = 1, 2, 3$.

$$\frac{\partial \rho}{\partial t} + \frac{\partial(\rho u_i)}{\partial x_j} = 0 \quad (6.1)$$

$$p \frac{D u_i}{D t} = g \rho \delta_{i3} + \frac{\partial \sigma_{ij}}{\partial x_j} \quad (6.2)$$

$$\rho \frac{D E}{D t} = \frac{\partial}{\partial x_j} \left(k \frac{\partial \theta}{\partial x_j} \right) - p \frac{\partial u_j}{\partial x_j} + \Phi \quad (6.3)$$

where ρ is the density of the fluid, p the pressure and θ the temperature. μ is the coefficient of dynamic viscosity of the fluid, λ is the coefficient of bulk viscosity and k is the thermal conductivity. The total derivative is $D/Dt = \partial/\partial t + \vec{u} \cdot \nabla$, δ_{i3} selects for the upward vertical, σ_{ij} is the stress tensor and Φ is the rate of viscous dissipation per unit volume.

In 1916, Rayleigh applied the so-called Boussinesq approximation, due to both Oberbeck and Boussinesq, to the equations of motion. The idea behind this approximation is that, for fluid flows where the temperature varies relatively little, variations in the density of the fluid may be neglected except in the direction in which the fluid is affected by gravity (meaning the vertical direction). The approximation is particularly relevant for buoyancy-driven flows. We make the ansatz

$$\rho = \rho_0 \{1 - \alpha(\theta - \theta_0)\} \quad (6.4)$$

for ρ_0 the density of the fluid when the temperature of the bottom layer is θ_0 and α a constant coefficient. This has a number of consequences for the equations (6.1), best summarized by [51] as “*in short, one approximates the thermodynamic variables as constants except for the pressure and temperature and except for the density when multiplied by g.*” The resulting equations for continuity, motion and heat transfer are referred to as Boussinesq equations describing a Boussinesq fluid.

6.3 The equations of state

For our problem, we begin with the Boussinesq equations in three dimensions, where $\vec{u} = (u, v, w)$ is the velocity of the gas, $\vec{p} = (p_x, p_y, p_z)$ is pressure, and $\vec{\theta} = (\theta_x, \theta_y, \theta_z)$ is temperature.

$$\nabla \cdot \vec{u} = 0 \quad (6.5)$$

$$\frac{\partial \vec{u}}{\partial t} + \vec{u} \cdot \nabla \vec{u} = -\frac{1}{\rho_0} (\nabla \vec{p}) + v \Delta \vec{u} + (g - \alpha g(\theta_0 - \theta)) \hat{\mathbf{z}} \quad (6.6)$$

$$\frac{\partial \theta}{\partial t} + \vec{u} \cdot \nabla \theta = \kappa \theta \quad (6.7)$$

Further, $\hat{\mathbf{z}}$ denotes the axis in the positive vertical direction, v is the kinematic viscosity, κ is the thermal diffusivity, the Laplacian is $\Delta = \partial^2 / \partial x_j^2$, ∇ denotes the gradient and $\nabla \cdot$ the divergence.

We reformulate our equations in a frame of reference moving with velocity $-c_f$ by making the change of variables $\tilde{x} = x - c_f t$, so that, e.g., $\tilde{u}(\tilde{x}, t) = u(x - c_f t)$. This gives us:

$$\nabla \cdot \vec{u} = 0 \quad (6.8)$$

$$\frac{\partial \vec{u}}{\partial t} + c_f \frac{\partial \vec{u}}{\partial \tilde{x}} + \vec{u} \cdot \nabla \vec{u} = -\frac{1}{\rho_0} \nabla \vec{p} + v \Delta \vec{u} - (g + \alpha g(\theta_0 - \vec{\theta})) \hat{\mathbf{z}} \quad (6.9)$$

$$\frac{\partial \vec{\theta}}{\partial t} + c_f \frac{\partial \vec{\theta}}{\partial \tilde{x}} + \vec{u} \cdot \nabla \vec{\theta} = \kappa \Delta \vec{\theta} \quad (6.10)$$

where $\tilde{\cdot}$ represents a variable in the traveling frame. We find the “base state” of the system by considering the case when the fluid is neither moving nor changing in time and the temperature only changes in the vertical direction. We denote this state by \cdot^* and drop the $\tilde{\cdot}$ for the sake of notational sanity, assuming going forward that all variables are in a moving frame. This gives us the base state equations:

$$u^* = (u^*, v^*, w^*) = (c_w - c_f, 0, 0) \quad (6.11)$$

$$p^* = -\rho_0 g \left(z + \frac{\alpha \beta}{2} z^2 \right) + \rho_0 \quad (6.12)$$

$$\theta^* = \theta_0 - \beta z \quad (6.13)$$

where $\beta = \frac{\theta_0 - \theta_1}{d}$ where d is the height of the channel, $\theta(z=0) = \theta_0$ and $\theta(z=d) = \theta_1$.

We linearize the moving frame equations (6.8) about perturbations to the base state (6.11), where $'$

represents such a perturbation:

$$U = U^* + u' \quad (6.14)$$

$$\theta = \theta^* + \theta' \quad (6.15)$$

$$p = p^* + p' \quad (6.16)$$

This results in the following linearized equations:

$$\nabla \cdot \vec{u}' = 0 \quad (6.17)$$

$$\frac{\partial \vec{u}'}{\partial t} + c_w \frac{\partial \vec{u}'}{\partial x} = -\frac{1}{\rho_0} \nabla \vec{p}' + v \Delta \vec{u}' + g \alpha \vec{\theta}' \hat{\mathbf{k}} \quad (6.18)$$

$$\frac{\partial \vec{\theta}'}{\partial t} + c_w \frac{\partial \vec{\theta}'}{\partial x} - \beta w' = \kappa \Delta \vec{\theta}' \quad (6.19)$$

Finally, we pick characteristic length and time scales:

$$\vec{x} = \frac{\vec{x}^*}{d} \quad t = \frac{\kappa t^*}{d^2} \quad \vec{u} = \frac{d \vec{u}^*}{\kappa} \quad \theta = \frac{\theta^*}{\beta d} \quad p = \frac{d^2 p^*}{\rho_0 \kappa} \quad (6.20)$$

where \cdot^* now denotes a dimensional variable (and we have omitted the $'$ denoting a perturbation for notational simplicity) and find the nondimensional system

$$\nabla \cdot \vec{u}' = 0 \quad (6.21)$$

$$\frac{\partial \vec{u}}{\partial t} = \sigma \frac{\partial \vec{u}'}{\partial x} - \nabla p + P \Delta \theta + R P \theta \hat{\mathbf{k}} \quad (6.22)$$

$$\frac{\partial \theta}{\partial t} = \sigma \frac{\partial \theta}{\partial x} + w + \Delta \theta \quad (6.23)$$

with nondimensional parameters

$$R = \frac{g \alpha \beta d^4}{\kappa v} \quad P = \frac{v}{\kappa} \quad \sigma = c \frac{d}{\kappa} \quad (6.24)$$

Here R is the Rayleigh number, P is the Prandtl number and σ is the nondimensional wind speed. Of note is the dependence of R on β , which in turn depends on the temperature of the hot plate, and the presence of a third nondimensional number, σ , which is not present in classical Rayleigh-Bénard convection.

6.3.1 Reduction to a system in w and θ

To further our analysis, we reduce the system (6.21)-(6.23) to a system in w (the vertical component of the velocity) and θ (the temperature) only. Taking the z component of the curl curl of (6.22) and using (6.21) yields

$$\frac{\partial \Delta w}{\partial t} = \sigma \Delta \left(\frac{\partial w}{\partial x} \right) + RP\Delta_1 \theta + P\Delta^2 w \quad (6.25)$$

where Δ_1 is the horizontal Laplacian $\Delta_1 = \frac{\partial^2}{\partial x^2} + \frac{\partial^2}{\partial y^2}$. We need six total boundary conditions to fully determine the system, as (6.25) is fourth order in w and (6.23) is second order in θ . The boundaries at $z = 0$ and $z = 1$ are maintained at a constant temperature, though internal temperature fluctuations are possible. Recall that equations (6.25) and (6.23) are for perturbations to the base state, not the base state itself. Therefore, because perturbations to the temperature at the boundary must be zero, we have $\theta(z = 0) = \theta(z = 1) = 0$.

We have some liberty with the w boundary conditions: we choose free-free boundary conditions for the sake of simplicity, though in further investigations a rigid boundary at $z = 0$ may be a more physical choice. Regardless, the upper boundary is an interface between a fluid and a fluid and therefore is a free boundary. We assume the same of the lower boundary. Such a free surface behaves as a rigid surface with tangential slip but no tangential stress [51]. The condition that the perturbations of the component of stress are zero at the surface gives us $w(z = 0) = w(z = 1) = 0$. Applying this result to the condition that the tangential stress be zero at both boundaries yields $w_{zz}(z = 0) = w_{zz}(z = 1) = 0$. For details as to the derivation, see [51]: these approximations to the free boundary conditions were used by Rayleigh in his original 1916 study. Both the width of the domain and the choice of boundary conditions affect the functional form and period of the resulting spatial modes.

Equations (6.25) and (6.23) together with boundary conditions

$$\begin{cases} \theta(z = 0) = w(z = 0) = \frac{\partial^2 w}{\partial z^2}(z = 0) = 0 \\ \theta(z = 1) = w(z = 1) = \frac{\partial^2 w}{\partial z^2}(z = 1) = 0 \end{cases} \quad (6.26)$$

fully characterize the original system.

6.4 Normal mode analysis

In the linear system we've derived, we may assume that our solutions $w(z, y, z, t)$ and $\theta(x, y, z, t)$ are superpositions of normal modes—functions of a single variable that capture the behavior of the solution in each dimension separately. To this end, we separate w and θ into the product of three spatial and one

temporal frequency and an exponential weighting term and assume our solutions have the form

$$\theta(x, y, z, t) = \exp\left(\frac{\sigma}{2}x\right) f(x, y) \phi(z) \exp(st) \quad (6.27)$$

$$w(x, y, z, t) = \exp\left(\frac{\sigma}{2}x\right) f(x, y) \eta(z) \exp(st) \quad (6.28)$$

where s is the temporal eigenvalue and $\exp\left(\frac{\sigma}{2}x\right)$ is an exponential weighting term tied to the nondimensional wind σ necessary to facilitate the separation of variables. Note that we have made the additional assumption that the x/y spatial dynamics are common to both θ and w .

Ultimately, our goal is to determine the eigenfunctions $\phi(z)$, $\eta(z)$ and $f(x, y)$. We begin by substituting (6.27) and (6.28) in to (6.23), yielding the eigenvalue problem for f :

$$\left[\frac{\partial}{\partial x^2} + \frac{\partial}{\partial y^2} \right] f = -(k^2 + n^2)f \quad (6.29)$$

where k is the wavenumber in the x direction and n the wavenumber in the y direction, and:

$$[D - \tilde{s} - \lambda] \phi = -\eta \quad (6.30)$$

where $D = \frac{\partial}{\partial z^2}$ and \tilde{s} and λ are chosen to emulate the structure of the eigenvalue problem in classical Rayleigh-Bénard convection:

$$\tilde{s} = s + \frac{\sigma^2}{2} - \sigma ik \quad (6.31)$$

$$\lambda = (k^2 + n^2) - \frac{\sigma^2}{2} + \sigma ik \quad (6.32)$$

Then, substituting (6.27) and (6.28) in to (6.25) and employing a substantial amount of algebra, we obtain our sixth order eigenvalue problem for $\eta(z)$:

$$[D^2 - \lambda] [D^2 - \lambda - \tilde{s}] \left[D^2 - \lambda - \frac{\tilde{s}}{P} \right] \eta = -R\lambda \eta \quad (6.33)$$

Lastly, we derive our transformed boundary conditions by substituting the original boundary conditions (6.26) in to the normal mode expansions (6.27) and (6.28) and applying the fourth order operator (6.30) to convert

our boundary conditions on θ and ϕ to conditions on w and η , giving us

$$\begin{aligned}\eta(z=0) &= \eta(z=1) = 0 \\ \eta''(z=0) &= \eta''(z=1) = 0 \\ \eta'''(z=0) &= \eta'''(z=1) = 0\end{aligned}\tag{6.34}$$

where \cdot' denotes differentiation with respect to z .

6.5 Spatial eigenfunctions

The sixth order eigenvalue problem (6.33) has general solution

$$\eta(z) = \sum_{i=1}^6 c_i \exp(\alpha_i + \beta_i z)\tag{6.35}$$

Let $r_i = \alpha_i + \beta_i$. Note that $r_1 = -r_4$, $r_2 = -r_5$ and $r_3 = -r_6$. Therefore, we have:

$$\eta(z) = c_1 e^{r_1 z} + c_2 e^{r_2 z} + c_3 e^{r_3 z} + c_4 e^{-r_1 z} + c_5 e^{-r_2 z} + c_6 e^{-r_3 z}\tag{6.36}$$

After imposing boundary conditions at $z = 0$, we find:

$$\eta(z) = 2i(c_1 \sin(r_1 z) + c_2 \sin(r_2 z) + c_3 \sin(r_3 z))\tag{6.37}$$

and, after imposing boundary conditions at $z = 1$:

$$\eta(z) = c_1 \sin(j_1 \pi z) + c_2 \sin(j_2 \pi z) + c_3 \sin(j_3 \pi z), \quad j_i \in \mathbb{Z}\tag{6.38}$$

Lastly, note that (6.29) has solution

$$f(x, y) = \exp(i(kx + ny))\tag{6.39}$$

We would like for these solutions to satisfy homogeneous boundary conditions in both the x and the y directions, with some periodic structure in the y direction. The solution space to the eigenvalue problem in f is spanned by functions of the form (6.39). The real part of (6.39) forms an invariant subspace in the space of eigenfunctions and, because our original problem is real, we consider only the real part of the resulting

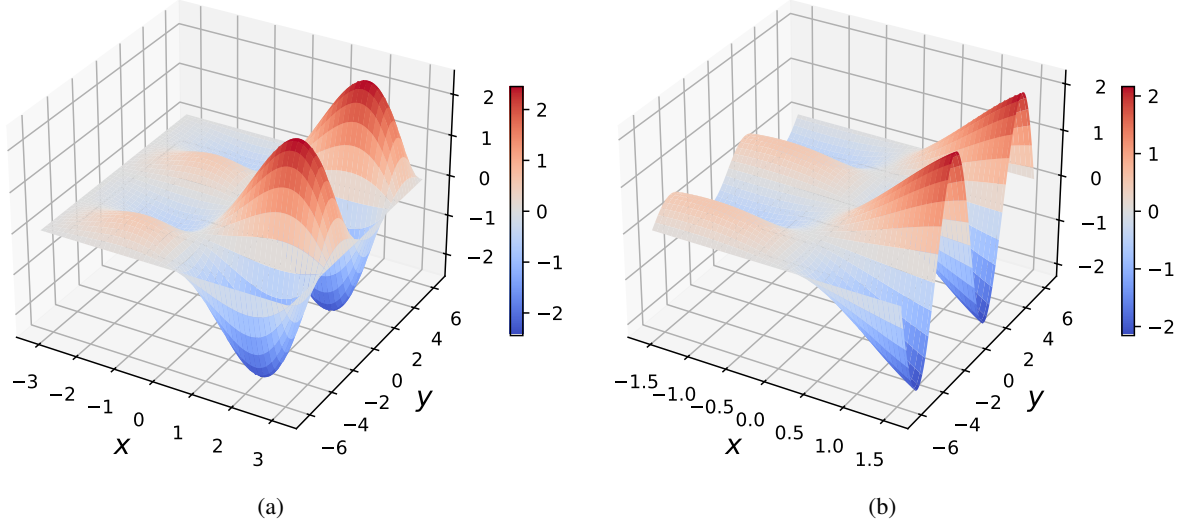


Figure 6.3: The real part of the spatial eigenfunction $w(x, y, z)$ for fixed $z = 0.5$ and $j = k = n = 1$. Note the growth of the eigenfunctions in the x direction and the periodicity in the y direction. (b) shows the same eigenfunction but for an x domain that cuts off halfway across the hot plate, illustrating the sinusoidal pattern of updrafts and downdrafts.

eigenfunction. Moreover, because we are interested in the lowest-order harmonics, for the visualization in figure 6.3, we consider a single sine function for $\eta(z)$ and set $c_2 = c_3 = 0$.

In classical Rayleigh-Bénard convection, marginal stability coincides with $s = 0$ because the **principle of exchange of stabilities** holds, meaning that whenever $\text{Re}(s) = 0$, $\text{Im}(s) = 0$. We will soon see this is not the case for this example of modified, wind-driven Rayleigh-Bénard convection: at marginal stability, $s \neq 0$ and the resulting eigenfunctions have dependence on the temporal eigenvalue s . Still, it is illuminating to consider the spatial structure of the eigenfunctions when $s = 0$.

For a fixed z value halfway to the top of the channel illustrated in figure 6.2, we see that the magnitude of the vertical velocity w grows across the domain before returning to zero at the edge of the hot plate (see figure 6.3 (a)). For a domain that does not encompass the entire hot plate (see figure 6.3 (c)), the sinusoidal pattern of updrafts and downdrafts is evident. We pick $j = 1$ because, upon analyzing the spectrum in the next section, we will see that this is the first wave number for which the spectrum moves through the imaginary axis. We also choose $k = 1$ because we do not expect oscillations in the x direction. The choice of n controls the frequency of the pattern in the transverse direction: for the purposes of our visualization, we pick $n = 1$.

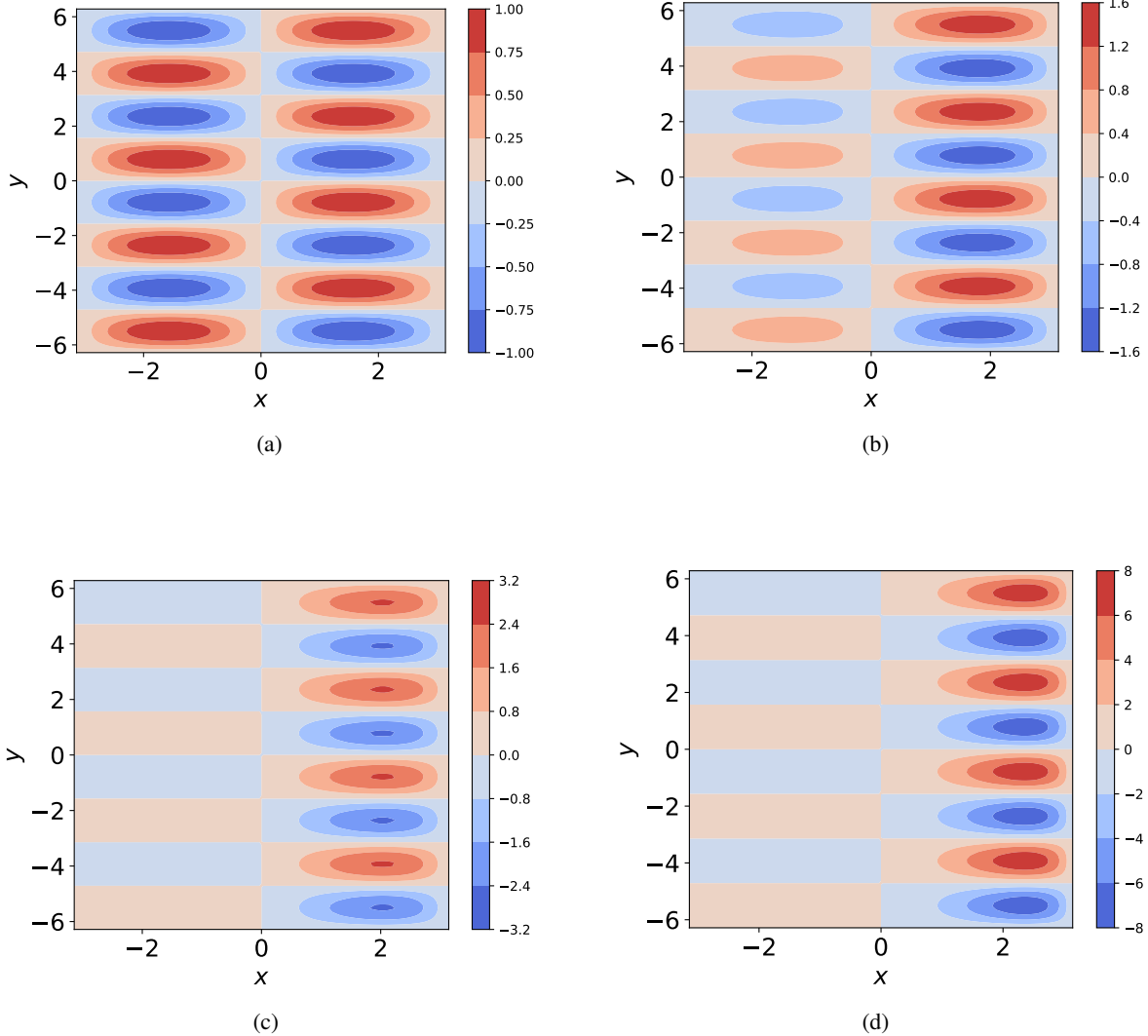


Figure 6.4: Contour plots of the eigenfunctions $w(x, y, z)$ for $j = k = 1$ and $n = 2$ and (a) $\sigma = 0$, (b) $\sigma = 0.5$, (c) $\sigma = 1$ and (d) $\sigma = 2$ for fixed $z = 0.5$, halfway up the vertical domain.

6.6 Analyzing the spectrum

Substituting the solutions (6.38) and (6.39) in to (6.23) and (6.25) results in a sixth order characteristic polynomial in j , the spatial wavenumber in the z direction, and λ and \tilde{s} as defined in (6.31).

$$[-j^2\pi^2 - \lambda] [-j^2\pi^2 - \lambda - \tilde{s}] [-j^2\pi^2 - \lambda - \tilde{s}/P] = -R\lambda \quad (6.40)$$

Of interest are parameter regimes for which $\text{Re}(s) = 0$, indicating a bifurcation, and the value of $\text{Im}(s)$ for these parameters, indicating what kind of bifurcation occurs. We consider the Rayleigh number R —which is directly tied to the temperature of the hot plate—as our bifurcating parameter and search for critical values,

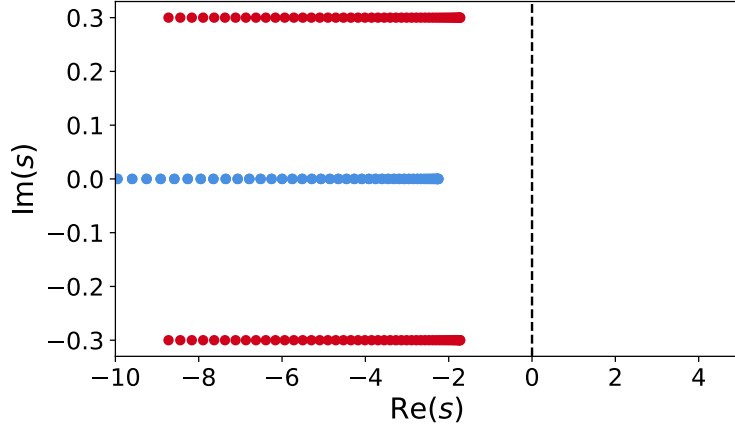


Figure 6.5: The spectrum for $\sigma = -1$ and $R = 0$: in other words, $\text{Re}(s)$ vs. $\text{Im}(s)$ parameterized as a function of j . In this case, at least one of the terms on the left hand side of (6.40) must be zero: it cannot be the first, due to a disagreement of signs. The second term yields s entirely real and gives us the spectrum along the imaginary axis in blue. The third term gives us both real and imaginary parts of s , where the imaginary parts correspond to $\pm k$ and are indicated in red.

denoted R_c , for which the system is marginally stable.

We consider a number of cases to gain intuition about the spectrum. The first is the case when $R = 0$, in which case we know at least one of the terms on the left hand side of (6.40) must be identically zero, yielding the spectrum in figure 6.5. The second is the case when the wind speed $\sigma = 0$. All three branches of the spectrum, which are distinct for σ nonzero as in figure 6.5, collapse down to one branch along the real axis. As a result, a steady state bifurcation exists with $\text{Re}(s) = \text{Im}(s) = 0$, which is in agreement with results from classical Rayleigh-Bénard convection. Moreover, for appropriate choices of the wave numbers k, n and j , we find that the bifurcation occurs for a critical Rayleigh number of $R_c = 657.5$, which is exactly in agreement with classical theory (see [49]).

Lastly, we consider the case of nonzero wind speed. In this case, the spectrum does not move through the imaginary axis only at the origin: in other words, $\text{Im}(s) \neq 0$ when $\text{Re}(s) = 0$, implying the existence of a Hopf bifurcation. Moreover, increasing the magnitude of the wind speed or the magnitude of the transverse wave number n results in a higher value of the critical Rayleigh number R_c . The implication is that, for a stronger wind, we require a hotter hot plate in order to cross the threshold in to an unstable regime. Moreover, we find that the spatial frequency of the resulting pattern in the transverse direction increases with the value of R_c .

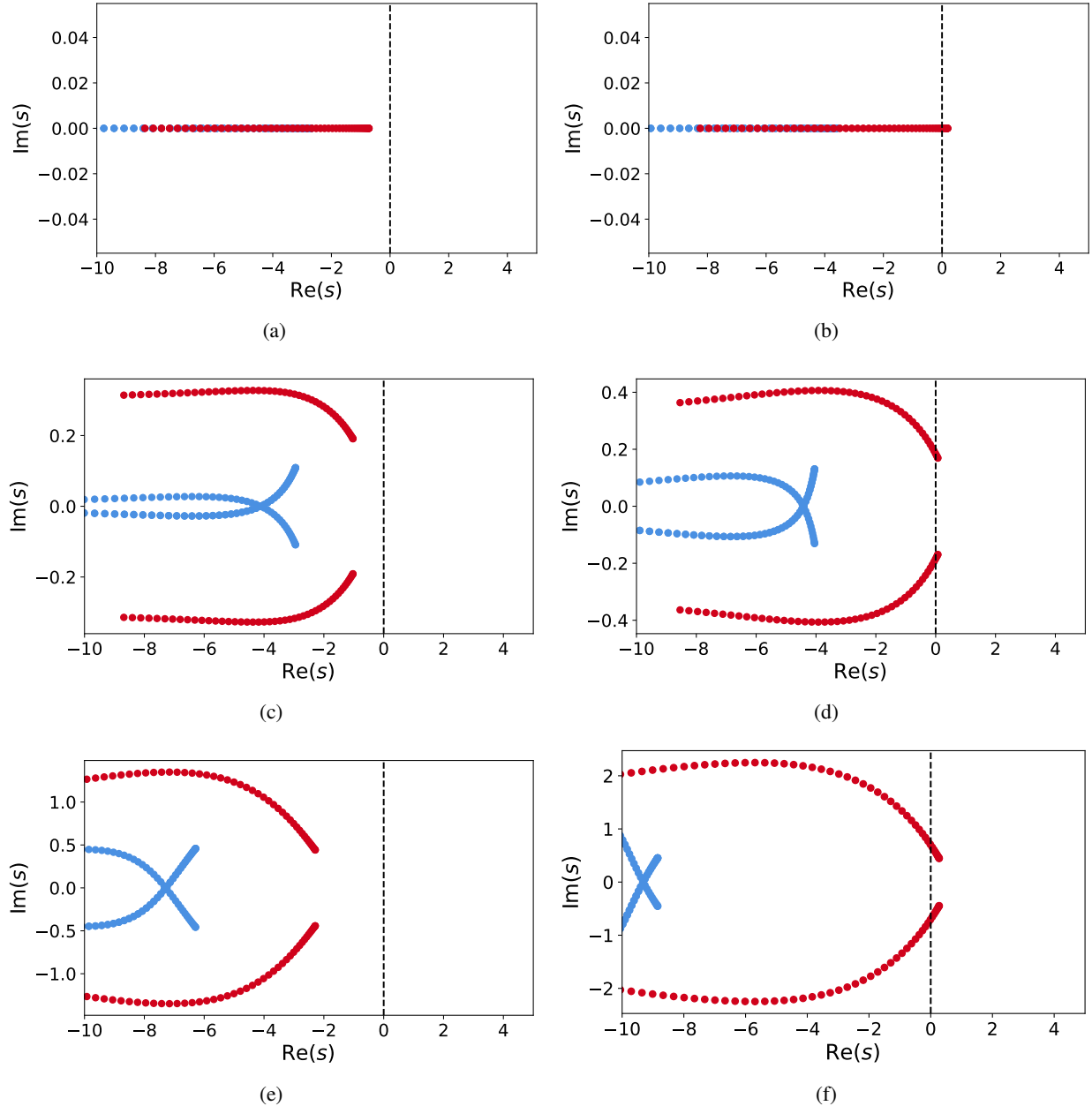


Figure 6.6: The spectrum for $\sigma = 0$ is entirely real. In (a), $R = 1.25$ and, in (b), $R = 5$. Note that the steady-state bifurcation occurs for R_c between these values: the exact value may be found using a root-finding method. The spectrum for $\sigma = -1$ with (c) $R = 1.25$ and (d) $R = 6$ exhibits a Hopf bifurcation for some R_c between these values, as does the spectrum for $\sigma = -3$ with (d) $R = 6$ and (e) $R = 30$. Note that the bifurcation occurs for a much larger R_c compared to the R_c found when $\sigma = -1$.

6.7 Conclusion

In conclusion, we have demonstrated that a system including only the effects of thermally-induced buoyancy, and not of combustion or fuel consumption, is capable of generating spatial patterning reminiscent of the towers and troughs phenomenon. In particular, the inclusion of an external forcing modeling the wind results in spatial patterns that “grow” across the domain, as is expected of the developing counter-rotational vortices that characterize towers and troughs. Moreover, the state of marginal stability corresponds to a Hopf bifurcation, implying that the resulting pattern state evolves in time.

Lastly, both the speed of the wind and the value of the transverse wave number n are proportional to the critical Rayleigh number. This has two implications: firstly, that a stronger wind necessitates a hotter hot plate (in analogy, a more intense fire) in order to generate spatial patterning. This is physically consistent: if the strength of the updraft induced by the thermal buoyancy is overwhelmed by the streamwise wind, a pattern of updrafts and downdrafts cannot develop. Secondly, a higher hot plate temperature (as indicated by a higher value of R_c) is correlated with a higher frequency of the pattern in the transverse direction (as indicated by the value of n). This result is in agreement with experimental work studying airflow over hot plates [16], suggesting that the mechanisms at play in such experiments are captured by our minimal model.

CHAPTER 7

Conclusions

In this thesis, we sought to identify the physical drivers of pattern formation in systems describing propagating fire fronts. In particular, we asked if we might observe the onset of instability in (1) a reaction-diffusion system modeling temperature acted on by a spatially dependent wind and (2) a thermally-driven fluids system with the inclusion of a crosswind term. In essence, the question boiled down to whether the onset of instability could be attributed to the interplay between diffusing heat and the combustion reaction or to thermally-driven buoyancy and the resulting fluid dynamics (or, perhaps, both or neither).

In Chapter 3, we introduce a two-dimensional reaction-diffusion model of fire propagation augmented by a wind term that “switches” in space. The resulting system has rich geometric structure and multi-scale dynamics, and we develop the framework necessary to study it in the remainder of that chapter. We are able to analyze the dynamics of the system in the vicinity of traveling wave solutions by considering the corresponding linearization. This allows us to study the streamwise (parallel to the direction of motion of the front) and transverse (normal to the direction of motion) dynamics separately in the subsequent chapters.

We begin with the streamwise system in Chapter 4, building on classical theory concerning the existence, uniqueness and stability of traveling wave solutions to reaction-diffusion systems to include a system with a spatially dependent advection coefficient. We look for wave solutions as heteroclinic connections, in the form of intersecting invariant manifolds, between the system’s equilibria. Doing so allows us to develop an understanding of the range of wave speeds for which traveling wave solutions exist and how their speeds and shapes are influenced by the magnitude and sign of the imposed wind. Using geometric methods and tools from Sturm-Liouville theory, we classify the stability of the resulting solutions and develop a means of identifying the most stable, and therefore most physically viable, solution. We use these results to draw conclusions about the spatial location of the wind switch in relation to that of the fire line, which we find to be in agreement with the physics of air entrainment. Lastly, our results give us a means of imposing constraints on the wind term to ensure stability.

Then, in Chapter 5, we turn to the transverse problem. We restructure many of the approaches developed

in Chapter 4, particularly the “accumulated angle” method of detecting positive eigenvalues, and adapt them to the specifics of this new setting. We identify clear regions of transverse instability due to the spatially dependent wind and identify the structure of the corresponding eigenfunctions. Finally, we incorporate the results of the previous chapter to understand the two-dimensional stability landscape for a range of wind magnitudes (and, in the case of the transverse wind, rates at which the switch occurs). We discuss the spatial structure of the full, the two-dimensional eigenfunction for parameter values corresponding to positive eigenvalues and, therefore, instability in the underlying system.

In Chapter 6, we dispense with the effect of combustion entirely. Instead, we consider an analogue of the classical model for Rayleigh-Bénard convection with the addition of a crosswind term to model the movement of a propagating fireline. Using techniques from the field of linear stability for hydrodynamics, we investigate the emergence of patterned states as a result of thermally driven-buoyancy of the air in the vicinity of the fireline. We identify conditions on the critical Rayleigh number, which is tied to the magnitude of the thermal forcing, for the onset of marginal stability and visualize the resulting spatially patterned eigenfunctions. Lastly, we note that the transition to instability occurs by way of a Hopf bifurcation in the presence of a wind term; without it, the spectrum is entirely real at the point of marginal stability.

We find regimes of two-dimensional instability in both systems, suggesting that neither mechanism is solely responsible for pattern formation; both play a part. In reality, spatial structures in the velocity and temperature fields are coupled, as extensive experimental work (see, e.g., [17]) documents. However, the spectral stability of the system considered in Chapters 3-5 in the presence of a constant wind highlights the need for spatial patterning of the advection term to induce spatial patterning of the front. The mechanisms described in Chapter 6 may be understood as leading to this patterning in initially quiescent flow—particularly in the transverse case, where the spatial dependence of the wind term considered is an emergent phenomenon.

CODE APPENDIX

All code created for this thesis is publicly available at <https://github.com/o-chandra/dissertation>.

REFERENCES

- [1] “National Interagency Coordination Center Wildland Fire Summary and Statistics Annual Report 2023,” en, National Interagency Coordination Center, Tech. Rep., 2023.
- [2] A. L. Sullivan, “Wildland surface fire spread modelling, 1990 to 2007. 1: Physical and quasi-physical models,” *International Journal of Wildland Fire*, vol. 18, no. 4, pp. 349–368, 2009, Publisher: CSIRO Publishing. [Online]. Available: <https://www.publish.csiro.au/wf/wf06143> (visited on 11/18/2024).
- [3] A. L. Sullivan, “Wildland surface fire spread modelling, 1990 to 2007. 2: Empirical and quasi-empirical models,” *International Journal of Wildland Fire*, vol. 18, no. 4, pp. 369–386, 2009, Publisher: CSIRO Publishing. [Online]. Available: <https://www.publish.csiro.au/wf/wf06142> (visited on 11/18/2024).
- [4] A. L. Sullivan, “Wildland surface fire spread modelling, 1990 to 2007. 3: Simulation and mathematical analogue models,” *International Journal of Wildland Fire*, vol. 18, no. 4, pp. 387–403, 2009, Publisher: CSIRO Publishing. [Online]. Available: <https://www.publish.csiro.au/WF/WF06144> (visited on 11/18/2024).
- [5] Richard C. Rothermel, “A mathematical model for predicting fire spread in wildland fuels,” en, *Res. Pap. INT-115. Ogden, UT: U.S. Department of Agriculture, Intermountain Forest and Range Experiment Station. 40 p.*, vol. 115, 1972. [Online]. Available: <https://research.fs.usda.gov/treesearch/32533> (visited on 11/18/2024).
- [6] M. A. Finney, “FARSITE: Fire Area Simulator-model development and evaluation,” en, *Res. Pap. RMRS-RP-4, Revised 2004. Ogden, UT: U.S. Department of Agriculture, Forest Service, Rocky Mountain Research Station. 47 p.*, vol. 4, 1998. DOI: 10.2737/RMRS-RP-4. [Online]. Available: <https://research.fs.usda.gov/treesearch/4617> (visited on 11/18/2024).
- [7] M. A. Finney, “An Overview of FlamMap Fire Modeling Capabilities,” en, In: Andrews, Patricia L.; Butler, Bret W., comps. 2006. *Fuels Management-How to Measure Success: Conference Proceedings. 28-30 March 2006; Portland, OR. Proceedings RMRS-P-41. Fort Collins, CO: U.S. Department of Agriculture, Forest Service, Rocky Mountain Research Station. p. 213-220*, vol. 041, 2006. [Online]. Available: <https://research.fs.usda.gov/treesearch/25948> (visited on 11/18/2024).
- [8] P. L. Andrews, “BehavePlus fire modeling system: Past, present, and future,” en, In: *Proceedings of 7th Symposium on Fire and Forest Meteorology; 23-25 October 2007, Bar Harbor, Maine. Boston, MA: American Meteorological Society. 13 p.*, 2007. [Online]. Available: <https://research.fs.usda.gov/treesearch/31549> (visited on 11/18/2024).
- [9] R. Linn, J. Reisner, J. J. Colman, and J. Winterkamp, “Studying wildfire behavior using FIRETEC,” *International journal of wildland fire*, vol. 11, no. 4, pp. 233–246, 2002, Publisher: CSIRO Publishing. [Online]. Available: <https://www.publish.csiro.au/wf/wf02007> (visited on 11/18/2024).
- [10] D. H. Anderson, E. A. Catchpole, N. J. De Mestre, and T. Parkes, “Modelling the spread of grass fires,” en, *The Journal of the Australian Mathematical Society. Series B. Applied Mathematics*, vol. 23, no. 4, pp. 451–466, Apr. 1982, ISSN: 0334-2700, 1839-4078. DOI: 10.1017/S0334270000000394. [Online]. Available: https://www.cambridge.org/core/product/identifier/S0334270000000394/type/journal_article (visited on 11/18/2024).

- [11] V. Mallet, D. E. Keyes, and F. E. Fendell, “Modeling wildland fire propagation with level set methods,” *Computers & Mathematics with Applications*, vol. 57, no. 7, pp. 1089–1101, Apr. 2009, ISSN: 0898-1221. DOI: [10.1016/j.camwa.2008.10.089](https://doi.org/10.1016/j.camwa.2008.10.089). [Online]. Available: <https://www.sciencedirect.com/science/article/pii/S0898122108006329> (visited on 08/29/2024).
- [12] I. Karafyllidis and A. Thanailakis, “A model for predicting forest fire spreading using cellular automata,” *Ecological Modelling*, vol. 99, no. 1, pp. 87–97, Jun. 1997, ISSN: 0304-3800. DOI: [10.1016/S0304-3800\(96\)01942-4](https://doi.org/10.1016/S0304-3800(96)01942-4). [Online]. Available: <https://www.sciencedirect.com/science/article/pii/S0304380096019424> (visited on 11/18/2024).
- [13] A. Turing, “The chemical basis of morphogenesis,” en, *Philosophical Transactions of the Royal Society of London. Series B, Biological Sciences*, vol. 237, no. 641, pp. 37–72, Aug. 1952, ISSN: 2054-0280. DOI: [10.1098/rstb.1952.0012](https://doi.org/10.1098/rstb.1952.0012). [Online]. Available: <https://royalsocietypublishing.org/doi/10.1098/rstb.1952.0012> (visited on 11/18/2024).
- [14] D. L. Benson, P. K. Maini, and J. A. Sherratt, “Unravelling the Turing bifurcation using spatially varying diffusion coefficients,” en, *Journal of Mathematical Biology*, vol. 37, no. 5, pp. 381–417, Nov. 1998, ISSN: 0303-6812, 1432-1416. DOI: [10.1007/s002850050135](https://doi.org/10.1007/s002850050135). [Online]. Available: <http://link.springer.com/10.1007/s002850050135> (visited on 11/18/2024).
- [15] T. Banerjee, T. Holland, K. Solander, M. Holmes, and R. Linn, “Identifying Characteristics of Wildfire Towers and Troughs,” en, *Atmosphere*, vol. 11, no. 8, p. 796, Aug. 2020, Number: 8 Publisher: Multidisciplinary Digital Publishing Institute, ISSN: 2073-4433. DOI: [10.3390/atmos11080796](https://doi.org/10.3390/atmos11080796). [Online]. Available: <https://www.mdpi.com/2073-4433/11/8/796> (visited on 10/16/2024).
- [16] C. Miller, M. A. Finney, S. McAllister, E. Sluder, and M. J. Gollner, “Investigating coherent streaks in wildfires via heated plates in crosswind,” *Fire Safety Journal*, Fire Safety Science: Proceedings of the 12th International Symposium, vol. 91, pp. 735–741, Jul. 2017, ISSN: 0379-7112. DOI: [10.1016/j.firesaf.2017.03.035](https://doi.org/10.1016/j.firesaf.2017.03.035). [Online]. Available: <https://www.sciencedirect.com/science/article/pii/S0379711217300590> (visited on 10/01/2024).
- [17] A. Desai, S. Goodrick, and T. Banerjee, “Investigating the turbulent dynamics of small-scale surface fires,” *Scientific Reports*, vol. 12, p. 10503, Jun. 2022, ISSN: 2045-2322. DOI: [10.1038/s41598-022-13226-w](https://doi.org/10.1038/s41598-022-13226-w). [Online]. Available: <https://www.ncbi.nlm.nih.gov/pmc/articles/PMC9217930/> (visited on 08/27/2024).
- [18] P. Carter and A. Doelman, “Traveling Stripes in the Klausmeier Model of Vegetation Pattern Formation,” en, *SIAM Journal on Applied Mathematics*, vol. 78, no. 6, pp. 3213–3237, Jan. 2018, ISSN: 0036-1399, 1095-712X. DOI: [10.1137/18M1196996](https://doi.org/10.1137/18M1196996). [Online]. Available: <https://pubs.siam.org/doi/10.1137/18M1196996> (visited on 11/18/2024).
- [19] R. Murray, *Nonlinear Systems: Local Theory*, Jan. 2011.
- [20] P. W. Bates and C. K. R. T. Jones, “Invariant Manifolds for Semilinear Partial Differential Equations,” in *Dynamics Reported: A Series in Dynamical Systems and Their Applications*, U. Kirchgraber and H. O. Walther, Eds., Wiesbaden: Vieweg+Teubner Verlag, 1989, pp. 1–38, ISBN: 978-3-322-96657-5. DOI: [10.1007/978-3-322-96657-5_1](https://doi.org/10.1007/978-3-322-96657-5_1). [Online]. Available: https://doi.org/10.1007/978-3-322-96657-5_1.
- [21] D. Henry, *Geometric Theory of Semilinear Parabolic Equations* (Lecture Notes in Mathematics). Berlin, Heidelberg: Springer, 1981, vol. 840, ISBN: 978-3-540-10557-2 978-3-540-38528-8. DOI: [10.1007/BFb0067027](https://doi.org/10.1007/BFb0067027).

- 1007/BFb0089647. [Online]. Available: <http://link.springer.com/10.1007/BFb0089647> (visited on 09/16/2024).
- [22] L. C. Evans, *Partial differential equations*. Providence, R.I.: American Mathematical Society, 2010, ISBN: 978-0-8218-4974-3 0-8218-4974-3.
- [23] B. Barker, J. Humpherys, G. Lyng, and J. Lytle, “Evans function computation for the stability of travelling waves,” en, *Philosophical Transactions of the Royal Society A: Mathematical, Physical and Engineering Sciences*, vol. 376, no. 2117, p. 20170184, Apr. 2018, ISSN: 1364-503X, 1471-2962. DOI: 10.1098/rsta.2017.0184. [Online]. Available: <https://royalsocietypublishing.org/doi/10.1098/rsta.2017.0184> (visited on 11/18/2024).
- [24] M. Beck, “Topics in stability theory for partial differential equations,” English, Diss. Boston University, Boston, MA, 2006.
- [25] G. Teschl, *Ordinary differential equations and dynamical systems* (Graduate studies in mathematics v. 140). Providence, R.I: American Mathematical Society, 2012, ISBN: 978-0-8218-8328-0.
- [26] T. Kapitula, *The Evans Function: A Primer*, en, 2004.
- [27] C. Jones, R. Gardner, and J. Alexander, “A topological invariant arising in the stability analysis of travelling waves.,” de, vol. 1990, no. 410, pp. 167–212, Jan. 1990, Publisher: De Gruyter Section: Journal fur die reine und angewandte Mathematik, ISSN: 1435-5345. DOI: 10.1515/crll.1990.410.167. [Online]. Available: <https://www.degruyter.com/document/doi/10.1515/crll.1990.410.167/html> (visited on 09/16/2024).
- [28] J. Norbury and A. M. Stuart, “Travelling Combustion Waves in a Porous Medium. part 1: Existence,” *SIAM Journal on Applied Mathematics*, vol. 48, no. 1, pp. 155–169, Feb. 1988, Publisher: Society for Industrial and Applied Mathematics, ISSN: 0036-1399. DOI: 10.1137/0148007. [Online]. Available: <https://pubs.siam.org/doi/abs/10.1137/0148007> (visited on 08/27/2024).
- [29] J. Norbury and A. M. Stuart, “Travelling Combustion Waves in a Porous Medium. part 2: Stability,” *SIAM Journal on Applied Mathematics*, vol. 48, no. 2, pp. 374–392, Apr. 1988, Publisher: Society for Industrial and Applied Mathematics, ISSN: 0036-1399. DOI: 10.1137/0148019. [Online]. Available: <https://pubs.siam.org/doi/abs/10.1137/0148019> (visited on 08/27/2024).
- [30] R. O. Weber, G. N. Mercer, H. S. Sidhu, and B. F. Gray, “Combustion waves for gases ($Le = 1$) and solids ($Le \gg 1$),” *Proceedings of the Royal Society of London. Series A: Mathematical, Physical and Engineering Sciences*, vol. 453, no. 1960, pp. 1105–1118, May 1997, Publisher: Royal Society. DOI: 10.1098/rspa.1997.0062. [Online]. Available: <https://royalsocietypublishing.org/doi/10.1098/rspa.1997.0062> (visited on 08/27/2024).
- [31] F. A. Albini, “A Model for Fire Spread in Wildland Fuels by-Radiation,” en, *Combustion Science and Technology*, vol. 42, no. 5-6, pp. 229–258, Mar. 1985, ISSN: 0010-2202, 1563-521X. DOI: 10.1080/00102208508960381. [Online]. Available: <http://www.tandfonline.com/doi/abs/10.1080/00102208508960381> (visited on 11/18/2024).
- [32] A. Bayliss and B. J. Matkowsky, “From Traveling Waves to Chaos in Combustion,” en, *SIAM Journal on Applied Mathematics*, vol. 54, no. 1, pp. 147–174, Feb. 1994, ISSN: 0036-1399, 1095-712X. DOI: 10.1137/S0036139992232921. [Online]. Available: <http://pubs.siam.org/doi/10.1137/S0036139992232921> (visited on 11/18/2024).

- [33] M. I. Asensio and L. Ferragut, “On a wildland fire model with radiation,” en, *International Journal for Numerical Methods in Engineering*, vol. 54, no. 1, pp. 137–157, May 2002, ISSN: 0029-5981, 1097-0207. DOI: [10.1002/nme.420](https://doi.org/10.1002/nme.420). [Online]. Available: <https://onlinelibrary.wiley.com/doi/10.1002/nme.420> (visited on 11/18/2024).
- [34] J. Mandel, L. S. Bennethum, J. D. Beezley, *et al.*, “A wildland fire model with data assimilation,” *Mathematics and Computers in Simulation*, vol. 79, no. 3, pp. 584–606, Dec. 2008, ISSN: 0378-4754. DOI: [10.1016/j.matcom.2008.03.015](https://doi.org/10.1016/j.matcom.2008.03.015). [Online]. Available: <https://www.sciencedirect.com/science/article/pii/S0378475408001572> (visited on 08/27/2024).
- [35] A. Ghazaryan and C. K. R. T. Jones, “On the stability of high Lewis number combustion fronts,” en, *Discrete and Continuous Dynamical Systems*, vol. 24, no. 3, pp. 809–826, Apr. 2009, Publisher: Discrete and Continuous Dynamical Systems, ISSN: 1078-0947. DOI: [10.3934/dcds.2009.24.809](https://doi.org/10.3934/dcds.2009.24.809). [Online]. Available: <https://www.aims sciences.org/en/article/doi/10.3934/dcds.2009.24.809> (visited on 11/18/2024).
- [36] S. Harris and N. McDonald, “Fingering instability in wildfire fronts,” *Journal of Fluid Mechanics*, vol. 943, A34, 2022. DOI: [10.1017/jfm.2022.452](https://doi.org/10.1017/jfm.2022.452).
- [37] S. Dipierro, E. Valdinoci, G. Wheeler, and V.-M. Wheeler, “A Simple but Effective Bushfire Model: Analysis and Real-Time Simulations,” *SIAM Journal on Applied Mathematics*, pp. 1504–1514, Aug. 2024, Publisher: Society for Industrial and Applied Mathematics, ISSN: 0036-1399. DOI: [10.1137/24M1644596](https://doi.org/10.1137/24M1644596). [Online]. Available: <https://pubs.siam.org/doi/10.1137/24M1644596> (visited on 08/27/2024).
- [38] P. Carter, A. Doelman, K. Lilly, E. Obermayer, and S. Rao, “Criteria for the (in) stability of planar interfaces in singularly perturbed 2-component reactionâdiffusion equations,” *Physica D: Nonlinear Phenomena*, vol. 444, p. 133 596, 2023, Publisher: Elsevier. [Online]. Available: <https://www.sciencedirect.com/science/article/pii/S0167278922003001> (visited on 11/18/2024).
- [39] P. Carter, “A Stabilizing Effect of Advection on Planar Interfaces in Singularly Perturbed Reaction-Diffusion Equations,” en, *SIAM Journal on Applied Mathematics*, vol. 84, no. 3, pp. 1227–1253, Jun. 2024, ISSN: 0036-1399, 1095-712X. DOI: [10.1137/23M1610872](https://doi.org/10.1137/23M1610872). [Online]. Available: <https://pubs.siam.org/doi/10.1137/23M1610872> (visited on 11/18/2024).
- [40] C. K. R. T. Jones, “Geometric singular perturbation theory,” en, in *Dynamical Systems: Lectures Given at the 2nd Session of the Centro Internazionale Matematico Estivo*, L. Arnold, C. K. R. T. Jones, K. Mischaikow, G. Raugel, and R. Johnson, Eds., Berlin, Heidelberg: Springer, 1995, pp. 44–118, ISBN: 978-3-540-49415-7. DOI: [10.1007/BFb0095239](https://doi.org/10.1007/BFb0095239). [Online]. Available: <https://doi.org/10.1007/BFb0095239> (visited on 09/24/2024).
- [41] B. Barker, J. Humpherys, J. Lytle, and K. Zumbrun, *Stablab: A matlab-based numerical library for evans function computation*, 2015. [Online]. Available: <https://github.com/nonlinear-waves>.
- [42] J. M. Canfield, R. R. Linn, J. A. Sauer, M. Finney, and J. Forthofer, “A numerical investigation of the interplay between fireline length, geometry, and rate of spread,” *Agricultural and Forest Meteorology*, vol. 189-190, pp. 48–59, Jun. 2014, ISSN: 0168-1923. DOI: [10.1016/j.agrformet.2014.01.007](https://doi.org/10.1016/j.agrformet.2014.01.007). [Online]. Available: <https://www.sciencedirect.com/science/article/pii/S0168192314000082> (visited on 08/29/2024).

- [43] R. M. Nelson, B. W. Butler, and D. R. Weise, “Entrainment regimes and flame characteristics of wildland fires,” en, *International Journal of Wildland Fire*. 21: 127-140. (*Includes Accessory Publication.*), vol. 21, pp. 127–140, 2012. DOI: 10.1071/WF10034. [Online]. Available: <https://research.fs.usda.gov/treesearch/40492> (visited on 08/27/2024).
- [44] R. R. Linn, J. M. Canfield, P. Cunningham, C. Edminster, J. .-. Dupuy, and F. Pimont, “Using periodic line fires to gain a new perspective on multi-dimensional aspects of forward fire spread,” *Agricultural and Forest Meteorology*, vol. 157, pp. 60–76, May 2012, ISSN: 0168-1923. DOI: 10.1016/j.agrformet.2012.01.014. [Online]. Available: <https://www.sciencedirect.com/science/article/pii/S0168192312000445> (visited on 10/01/2024).
- [45] A. Ghazaryan, S. Lafourte, and P. McLarnan, “Stability Analysis for Combustion Fronts Traveling in Hydraulically Resistant Porous Media,” *SIAM Journal on Applied Mathematics*, vol. 75, no. 3, pp. 1225–1244, Jan. 2015, Publisher: Society for Industrial and Applied Mathematics, ISSN: 0036-1399. DOI: 10.1137/140981204. [Online]. Available: <https://pubs.siam.org/doi/10.1137/140981204> (visited on 08/27/2024).
- [46] B. Sandstede, “Stability of Travelling Waves,” en, in *Handbook of Dynamical Systems*, vol. 2, Elsevier, 2002, pp. 983–1055, ISBN: 978-0-444-50168-4. DOI: 10.1016/S1874-575X(02)80039-X. [Online]. Available: <https://linkinghub.elsevier.com/retrieve/pii/S1874575X0280039X> (visited on 08/27/2024).
- [47] P. C. Fife and J. B. McLeod, “The approach of solutions of nonlinear diffusion equations to travelling front solutions,” en, *Archive for Rational Mechanics and Analysis*, vol. 65, no. 4, pp. 335–361, Dec. 1977, ISSN: 0003-9527, 1432-0673. DOI: 10.1007/BF00250432. [Online]. Available: <http://link.springer.com/10.1007/BF00250432> (visited on 10/01/2024).
- [48] M. A. Finney, J. D. Cohen, J. M. Forhofer, et al., “Role of buoyant flame dynamics in wildfire spread,” *Proceedings of the National Academy of Sciences*, vol. 112, no. 32, pp. 9833–9838, Aug. 2015, Publisher: Proceedings of the National Academy of Sciences. DOI: 10.1073/pnas.1504498112. [Online]. Available: <https://www.pnas.org/doi/full/10.1073/pnas.1504498112> (visited on 10/16/2024).
- [49] S. Chandrasekhar, *Hydrodynamic and hydromagnetic stability*, Dover ed. New York: Dover Publications, 1981, ISBN: 978-0-486-64071-6.
- [50] G. K. Batchelor, *An Introduction to Fluid Dynamics*, 1st ed. Cambridge University Press, Feb. 2000, ISBN: 978-0-521-66396-0 978-0-511-80095-5. DOI: 10.1017/CBO9780511800955. [Online]. Available: <https://www.cambridge.org/core/product/identifier/9780511800955/type/book> (visited on 11/18/2024).
- [51] P. G. Drazin and W. H. Reid, *Hydrodynamic Stability* (Cambridge Mathematical Library), 2nd ed. Cambridge: Cambridge University Press, 2004, ISBN: 978-0-521-52541-1. DOI: 10.1017/CBO9780511616938. [Online]. Available: <https://www.cambridge.org/core/books/hydrodynamic-stability/A0E78BC88D5572AED79CCCE8B977707C> (visited on 11/18/2024).
- [52] E. E. Zukoski, T. Kubota, and B. Cetegen, “Entrainment in fire plumes,” *Fire Safety Journal*, vol. 3, no. 2, pp. 107–121, Jan. 1981, ISSN: 0379-7112. DOI: 10.1016/0379-7112(81)90037-0. [Online]. Available: <https://www.sciencedirect.com/science/article/pii/0379711281900370> (visited on 08/27/2024).

- [53] J. Hilton, A. Sullivan, W. Swedosh, J. Sharples, and C. Thomas, “Incorporating convective feedback in wildfire simulations using pyrogenic potential,” en, *Environmental Modelling & Software*, vol. 107, pp. 12–24, Sep. 2018, ISSN: 13648152. DOI: [10.1016/j.envsoft.2018.05.009](https://doi.org/10.1016/j.envsoft.2018.05.009). [Online]. Available: <https://linkinghub.elsevier.com/retrieve/pii/S1364815217309593> (visited on 08/27/2024).
- [54] C. Lautenberger, “Wildland fire modeling with an Eulerian level set method and automated calibration,” *Fire Safety Journal*, vol. 62, pp. 289–298, Nov. 2013, ISSN: 0379-7112. DOI: [10.1016/j.firesaf.2013.08.014](https://doi.org/10.1016/j.firesaf.2013.08.014). [Online]. Available: <https://www.sciencedirect.com/science/article/pii/S0379711213001343> (visited on 08/29/2024).
- [55] A. L. Atchley, R. Linn, A. Jonko, et al., “Effects of fuel spatial distribution on wildland fire behaviour,” en, *International Journal of Wildland Fire*, 30: 179-189., vol. 30, pp. 179–189, 2021. DOI: [10.1071/WF20096](https://doi.org/10.1071/WF20096). [Online]. Available: <https://research.fs.usda.gov/treesearch/62194> (visited on 08/29/2024).
- [56] J. H. Barrett, “Oscillation theory of ordinary linear differential equations,” *Advances in Mathematics*, vol. 3, no. 4, pp. 415–509, Oct. 1969, ISSN: 0001-8708. DOI: [10.1016/0001-8708\(69\)90008-5](https://doi.org/10.1016/0001-8708(69)90008-5). [Online]. Available: <https://www.sciencedirect.com/science/article/pii/0001870869900085> (visited on 09/16/2024).
- [57] T. Kapitula and B. Sandstede, “Eigenvalues and resonances using the Evans function,” en, *Discrete and Continuous Dynamical Systems*, vol. 10, no. 4, pp. 857–869, Mar. 2004, Publisher: Discrete and Continuous Dynamical Systems, ISSN: 1078-0947. DOI: [10.3934/dcds.2004.10.857](https://doi.org/10.3934/dcds.2004.10.857). [Online]. Available: <https://www.aims.science/en/article/doi/10.3934/dcds.2004.10.857> (visited on 09/16/2024).
- [58] R. A. Gardner and K. Zumbrun, “The gap lemma and geometric criteria for instability of viscous shock profiles,” en, *Communications on Pure and Applied Mathematics*, vol. 51, no. 7, pp. 797–855, Jul. 1998, ISSN: 0010-3640, 1097-0312. DOI: [10.1002/\(SICI\)1097-0312\(199807\)51:7<797::AID-CPA3>3.0.CO;2-1](https://doi.org/10.1002/(SICI)1097-0312(199807)51:7<797::AID-CPA3>3.0.CO;2-1). [Online]. Available: [https://onlinelibrary.wiley.com/doi/10.1002/\(SICI\)1097-0312\(199807\)51:7%3C797::AID-CPA3%3E3.0.CO;2-1](https://onlinelibrary.wiley.com/doi/10.1002/(SICI)1097-0312(199807)51:7%3C797::AID-CPA3%3E3.0.CO;2-1) (visited on 09/16/2024).
- [59] D. H. Sattinger, “On the stability of waves of nonlinear parabolic systems,” *Advances in Mathematics*, vol. 22, no. 3, pp. 312–355, Dec. 1976, ISSN: 0001-8708. DOI: [10.1016/0001-8708\(76\)90098-0](https://doi.org/10.1016/0001-8708(76)90098-0). [Online]. Available: <https://www.sciencedirect.com/science/article/pii/0001870876900980> (visited on 09/16/2024).
- [60] R. Levicky, “Integral (macroscopic) balance equations,”
- [61] B. Gabbert, *Findings about the fluid dynamics of wildfires*, en-US, Dec. 2019. [Online]. Available: <https://wildfiretoday.com/2019/12/30/findings-about-the-fluid-dynamics-of-wildfires/> (visited on 10/16/2024).
- [62] R. Linn, “Fluid dynamics of wildfires,” *Physics Today*, vol. 72, no. 11, p. 70, Nov. 2019, ISSN: 0031-9228. DOI: [10.1063/PT.3.4350](https://doi.org/10.1063/PT.3.4350). [Online]. Available: <https://doi.org/10.1063/PT.3.4350> (visited on 10/16/2024).
- [63] P. L. Andrews, “The Rothermel surface fire spread model and associated developments: A comprehensive explanation,” en, *Gen. Tech. Rep. RMRS-GTR-371. Fort Collins, CO: U.S. Department of Agriculture, Forest Service, Rocky Mountain Research Station.* 121 p., vol. 371, 2018. DOI: [10.2737/RMRS-2018-001](https://doi.org/10.2737/RMRS-2018-001)

GTR-371. [Online]. Available: <https://research.fs.usda.gov/treesearch/55928> (visited on 11/18/2024).

- [64] T. Ghisu, B. Arca, G. Pellizzaro, and P. Duce, “An Improved Cellular Automata for Wildfire Spread,” en, *Procedia Computer Science*, vol. 51, pp. 2287–2296, 2015, ISSN: 18770509. DOI: [10.1016/j.procs.2015.05.388](https://doi.org/10.1016/j.procs.2015.05.388). [Online]. Available: <https://linkinghub.elsevier.com/retrieve/pii/S1877050915011965> (visited on 11/18/2024).
- [65] J. D. Meiss, *Differential Dynamical Systems, Revised Edition* (Mathematical Modeling and Computation). Society for Industrial and Applied Mathematics, Jan. 2017, ISBN: 978-1-61197-463-8. DOI: [10.1137/1.9781611974645](https://doi.org/10.1137/1.9781611974645). [Online]. Available: <https://pubs.siam.org/doi/book/10.1137/1.9781611974645> (visited on 11/18/2024).
- [66] F. A. Albini, “Estimating wildfire behavior and effects,” en, *Gen. Tech. Rep. INT-GTR-30. Ogden, UT: U.S. Department of Agriculture, Forest Service, Intermountain Forest and Range Experiment Station.* 92 p., vol. 30, 1976. [Online]. Available: <https://research.fs.usda.gov/treesearch/29574> (visited on 11/18/2024).
- [67] R. R. Linn and P. Cunningham, “Numerical simulations of grass fires using a coupled atmosphereâfire model: Basic fire behavior and dependence on wind speed,” en, *Journal of Geophysical Research: Atmospheres*, vol. 110, no. D13, 2004JD005597, Jul. 2005, ISSN: 0148-0227. DOI: [10.1029/2004JD005597](https://doi.org/10.1029/2004JD005597). [Online]. Available: <https://agupubs.onlinelibrary.wiley.com/doi/10.1029/2004JD005597> (visited on 11/18/2024).